

Copyright
by
Jae Hyun Kim
2015

**The Dissertation Committee for Jae Hyun Kim Certifies that this is the approved
version of the following dissertation:**

**Four-Probe Thermal and Thermoelectric Transport Measurements of
Bismuth Antimony Telluride, Silicon, and Boron Arsenide
Nanostructures**

Committee:

Li Shi, Supervisor

Jayathi Murthy

Yaguo Wang

Zhen Yao

Emanuel Tutuc

**Four-Probe Thermal and Thermoelectric Transport Measurements of
Bismuth Antimony Telluride, Silicon, and Boron Arsenide
Nanostructures**

by

Jae Hyun Kim, B. S.; M. S.

Dissertation

Presented to the Faculty of the Graduate School of
The University of Texas at Austin
in Partial Fulfillment
of the Requirements
for the Degree of

Doctor of Philosophy

The University of Texas at Austin

August 2015

Dedication

Jeewon and Yonu

Acknowledgements

I am sincerely grateful to my advisor professor Li Shi for his continuous support, insightful advice, and encouragement. I would not have been able to make this progress without his guidance. I would like to thank my dissertation committee members, professors Jayathi Murthy, Yaguo Wang, Zhen Yao, and Emanuel Tutuc. I also would like to thank previous and current lab members; Yong , Arden, Jae Hun, Michael, Insun, Dan, Pat, Mir, Annie, Eric, Gabbi, Brandon, and others, who helped me a lot in many aspects.

**Four-Probe Thermal and Thermoelectric Transport Measurements of
Bismuth Antimony Telluride, Silicon, and Boron Arsenide
Nanostructures**

Jae Hyun Kim, Ph. D.

The University of Texas at Austin, 2015

Supervisor: Li Shi

Thermal management in electronic devices has become a significant challenge because of the high power density in nanoelectronic devices. This challenge calls for a better understanding of thermal transport processes in nanostructures and devices, as well as new thermal management approaches such as high thermal conductivity materials and efficient on-chip thermoelectric coolers. While several experimental methods have been developed to investigate size-dependent thermal and thermoelectric properties, there are a number of limitations in the current experimental capability in probing nanoscale thermal and thermoelectric transport properties. Among these limitations is the difficulty in determining and eliminating the contact thermal resistance error so as to obtain the intrinsic thermal and thermoelectric properties of nanostructures. This dissertation presents an effort to develop new experimental methods for uncovering the intrinsic thermal and thermoelectric properties of nanostructures, and the applications of these methods for investigating the thermal and thermoelectric transport phenomena in three materials systems.

The intrinsic thermoelectric properties of bismuth antimony telluride nanostructures, which are synthesized by two different methods, are characterized with a four-probe thermoelectric measurement method based on a suspended device. The obtained thermoelectric property reveals a transition from n-type to p-type electronic transport as the antimony to bismuth ratio is increased to about 0.25. The peak zT was found when this ratio is close to 0.5. A new four-probe thermal transport measurement method is established in this work to probe both the contact thermal resistance and intrinsic thermal resistance of a nanostructure, which can be either an electrical conductor or insulator. The effectiveness of this method is demonstrated with its use to reveal size-dependent thermal conductivity of patterned silicon nanowires. The new four-probe measurement method is employed to obtain both the intrinsic thermal and thermoelectric properties of nanostructures of boron arsenide (BAs) with potentially record high thermal conductivity. The measurement results suggest that the thermal conductivity of one of such sample with an equivalent diameter of about $1.1 \mu\text{m}$ is higher than that of bulk silicon, despite pronounced phonon scattering by surface roughness and point defects associated with arsenic vacancies. In addition, high thermoelectric power factor was measured on the BAs sample.

Table of Contents

List of Figures	x
Chapter 1 Introduction	1
1.1 Background	1
1.2 Scope of work	3
Chapter 2 Thermoelectric Transport in Bismuth Antimony Telluride Nanostructures	7
2.1 Introduction	7
2.2 Sample preparation	8
2.2.1 Bi _{0.1} Sb _{1.9} Te ₃ film sample grown by MOCVD	8
2.2.2 Nanoplates grown by vapor solid method	13
2.3 Measurement results	16
2.3.1 Bi _{0.1} Sb _{1.9} Te ₃ film sample grown by MOCVD	16
2.3.2 Nanoplates grown by vapor solid method	25
2.4 Summary	28
Chapter 3 A novel four-probe thermal transport measurement method for nanostructures	31
3.1 Introduction	31
3.2 Measurement method	34
3.3 Experimental results	40
3.3.1 Device fabrication and sample preparation	40
3.3.2 Measurement setup	44
3.3.3 Measurement results	44
3.4 Summary	56
Chapter 4 Thermal and Thermoelectric Transport in Boron Arsenide Nanostructures	60
4.1 Introduction	60
4.2 Crystal growth and characterization	62
4.3 Experimental results	66

4.3.1 Sample preparation	66
4.3.2 Measurement results	71
4.4 Summary	81
Chapter 5 Conclusion.....	85
Bibliography	88
Vita.....	94

List of Figures

- Figure 2.1: A 170 nm thick $\text{Bi}_{0.1}\text{Sb}_{1.9}\text{Te}_3$ film sample grown on GaAs substrate is patterned by photo lithography and reactive ion etching, and suspended after wet etching of the GaAs substrate.11
- Figure 2.2: Structure of the 6-beam suspended measurement device (a), and an optical micrograph of a fabricated device before a sample is assembled on the device (b).....11
- Figure 2.3: Patterned $\text{Bi}_{0.1}\text{Sb}_{1.9}\text{Te}_3$ film sample is picked up with a sharp tungsten probe, and transferred on a piece of a Si substrate coated with a PVA layer (a). After the PMMA layer is spin coated on the sample, the PMMA layer together with the film sample is transferred and aligned on a pre-fabricated suspended device (b).....12
- Figure 2.4: Optical micrograph of a 170nm thick $\text{Bi}_{0.1}\text{Sb}_{1.9}\text{Te}_3$ film sample assembled on a pre-fabricated suspended device for thermoelectric measurement.13
- Figure 2.5: The vapor solid growth setup for $(\text{Bi}_{1-x}\text{Sb}_x)_2\text{Te}_3$ (a). The nanoplate samples can be picked up and transferred on a device by a sharp tungsten probe (b).15
- Figure 2.6: Optical micrographs for $(\text{Bi}_{1-x}\text{Sb}_x)_2\text{Te}_3$ nanoplates of $x=0.7$ (a), and $x=0.95$ (b). AFM images (c and d) of the areas indicated as a red square in (a) and (b).....16

Figure 2.7: Schematic diagram of a measurement device. Each serpentine Pt line is used as a resistive heater and thermometer. Heating is made by direct current (DC), and temperature is measured by alternating current (AC)	20
Figure 2.8: Measured temperature of each membrane (a), and thermovoltage drops of inner and outer electrodes as a function of temperature difference (b)	21
Figure 2.9: Measured thermal conductivity (a) and Seebeck coefficient (b) as a function of temperature.	22
Figure 2.10: Measured electrical conductivity (a) and thermoelectric figure of merit zT (b) as a function of temperature.	23
Figure 2.11: Calculated reduced Fermi level (a), hole carrier concentration (b), and Lorenz number (c) based on the measured Seebeck coefficient.	24
Figure 2.12: Measured Seebeck coefficient (a) and thermoelectric figure of merit zT (b) as a function of Sb content x . Some of data points are measured by Michael T. Pettes in same research group.	26
Figure 2.13: Measured Seebeck coefficient (a) and thermoelectric figure of merit zT (b) as a function of temperature. Some of data points are measured by Michael T. Pettes in same research group.	27
Figure 3.1: Optical micrograph of a device for four-probe thermal measurement with a Si nanowire sample assembled across all four suspended Pt/SiN _x RTs. The temperature profile of the i^{th} heater line shows a parabolic shape because of uniform Joule heating, and the other three j^{th} lines show linear temperature profile.	35

Figure 3.2: Thermal resistance circuit of the measurement device when RT1 is used as a heater at a rate of $(IV)_1$. R_1 , R_2 , and R_3 are the thermal resistances of the left, middle, and right suspended segments of the suspended Si nanowire sample. $R_{c,j}$ is the contact thermal resistance between the j^{th} Pt/SiN_x line and the sample. $R_{b,j}$ is the thermal resistance of the j^{th} Pt/SiN_x resistance thermometer line. $\theta_{c,j,i}$ is the j^{th} Pt/SiN_x line temperature at the contact to the sample when the i^{th} line is used as the heater line. The temperature rise θ_0 at the two ends of each of the suspended Pt/SiN_x lines is assumed to be negligible because the spreading thermal resistance of the Si substrate is orders of magnitude lower than $R_{b,j}$36

Figure 3.3: Completed devices assembled with silicon nanowire samples of two different cross section areas: 740 nm x 220 nm and 240 nm x 220 nm.42

Figure 3.4: Process of transferring silicon nanowire sample on a pre-fabricated device with four suspended thermometer lines. The nanowire is first transferred on a piece of wafer with PVA (polyvinyl alcohol) coating, and polymethyl methacrylate (PMMA) is spin coated on the piece. The PVA layer is dissolved in water, and the PMMA layer with the nanowire sample is floating on water. The PMMA layer is transferred and aligned on a suspended device, and the PMMA layer is removed finally.....43

- Figure 3.5: (a) Measured electrical resistance rises of RT1, RT2, RT3, and RT4 as a function of the heating current in RT1 at sample stage temperature $T_0 = 350\text{K}$. (b) Measured $R_e(I = 0)$ at different sample stage temperature (T_0). The temperature coefficient of resistance (TCR) can be obtained from the linear fit of each set of the measurement data.....46
- Figure 3.6: (a) Measured average temperature rise of each RT as a function of Joule heating rate in the first line when $T_0 = 350\text{K}$. (b) Net heat flow rate across the contact point from each thermometer line into the nanowire sample as a function of the heating current (I) in the first line.47
- Figure 3.7: Measured thermal resistances of four suspended thermometers as a function of stage temperature T_0 for 740 nm width sample (a) and 240 nm sample (b). The designs of both devices are the same, so that the values are almost same between the two samples.48
- Figure 3.8: (a) Measured contact point temperature rise of each RT as a function of the Joule heating rate in the first line when $T_0 = 350\text{K}$. (b) Net heat flow rate across the contact point from each thermometer line into the nanowire sample as a function of Joule heating rate in the first line.49
- Figure 3.9: The five measured thermal resistances, including the intrinsic thermal resistance of the middle suspended segment of the sample (R_2), and contact thermal resistances of the two middle contacts ($R_{c,2}$ and $R_{c,3}$), for the two Si nanowire samples with the cross section being 740 nm x 220 nm (a) and 240 nm x 220 nm (b).51

Figure 3.10: Measured thermal conductivity of the 740 nm wide (circles) and the 240 nm wide (squares) Si nanowire samples, both with 220 nm thickness. For comparison, the measured thermal conductivity data of bulk Si crystals (diamonds) reported by Glassbrenner and Slack, and two different theoretical calculation results for bulk Si and Si nanowires with the same equivalent diameter as the two samples measured here. The theoretical calculations are based on the models reported by Morelli, Heremans, and Slack (dashed lines) and Wang and Mingo (solid lines). Thin green, red, and thick blue lines and symbols are used for the results for bulk, $740 \times 220 \text{ nm}^2$, and $240 \times 220 \text{ nm}^2$ cross section. The uncertainty of some data points is smaller than the symbol size.55

Figure 4.1: Boron arsenide synthesizing process: Boron and arsenic pellets are mixed together in a quartz tube, and evacuated for one hour. The tube is sealed with oxy-acetylene torch, and the ampoules are placed in a box furnace at 800 °C for 72 hours. The furnace is cooled down slowly at a rate of 0.1 °C/min, and the growth process is completed64

Figure 4.2: Scanning electron micrographs (SEM) taken after the growth. Boron pellets are covered by various shapes of BAs crystals, including polycrystalline coating (a), small rods (b), dendrites (c), and platelets (d).....65

Figure 4.3: (a) XRD results of the boron pellets before and after the growth. (b) Raman spectroscopy of BAs crystals grown in this work in comparison to the results reported in Ref. 17 and 18.66

Figure 4.4: A BAs nanostructure crystal grown on the surface of boron pellet can be picked up with sharp tungsten probe (a), and transferred on a separate substrate coated with PVA for assembling on a suspended device (b)68

Figure 4.5: The BAs nanostructure sample shown in figure 4.4 (b) is characterized with Raman spectroscopy. It shows only one peak at 699 cm^{-1} , which matches with the reported values.68

Figure 4.6: The BAs nanostructure sample is transferred and aligned on a prefabricated suspended device together with the PMMA carrier layer as shown in (a), and (b) is the optical micrograph of the assembled PMMA, BAs, and suspended device.....69

Figure 4.7: The PMMA carrier layer is removed by heating at 350°C . Optical micrographs show the completed device for thermoelectric measurement (a). The gap between two inner suspended thermometer lines is $12.2\text{ }\mu\text{m}$. SEM micrographs are taken for measuring the width and thickness of the sample (b).....70

Figure 4.8: Thermal resistances of suspended thermometer lines (a), and intrinsic thermal resistance of BAs (R_2) and contact thermal resistances between the sample and two middle thermometer lines ($R_{c,2}$, $R_{c,3}$) (b).76

Figure 4.9: Measured point temperature rise at the contacts between the BAs sample and two inner thermometer lines at 300K , which is plotted by heating current (a) and heating rate (b). They are very close, but still detectable the different slope in (b).....77

Figure 4.10: Measured thermal conductivity of BAs nanostructure sample (black circles). Red and green star indicates the calculation value of 1140 nm diameter ¹¹BAs and natural BAs rods with an infinite length, respectively78

Figure 4.11: Measured Seebeck coefficient (a), and electrical resistivity (b) of the BAs nanostructure sample79

Figure 4.12: Calculated reduced Fermi level (a), hole carrier concentration (b), and Lorenz number (c) from the measured Seebeck coefficient according to the single parabolic band model.80

Chapter 1: Introduction

1.1 BACKGROUND

As nanofabrication technique for ultra large scale integrated (ULSI) electronic devices continues to progress, thermal management of the device becomes an important challenge because more power is generated per unit volume. In addition, non-uniform heat dissipation in the devices results in local hot spots, which are detrimental to device performance and reliability. According to the International Technology Roadmap for Semiconductors,¹ the critical feature size of nanoelectronic devices is already in a length scale less than 10 nm. The thermal conductivity of the semiconducting, dielectric, and metallic materials used in fabricating the devices can be reduced considerably at such a small dimension because of increased boundary scattering of electrons and phonons, the heat carriers in solids, as well as intriguing quantum confinement effects on these quasi particles. These size effects on the thermal transport property need to be understood better for rational design of next-generation electronic devices.

In addition, alternative materials with high thermal conductivity are desirable for use as heat spreading substrate or layers in future electronic devices. Diamond, graphite, graphene, and carbon nanotubes hold the highest thermal conductivity among known materials. Their thermal conductivity is dominated by the contribution from lattice vibration or phonons, which is high because the strong covalent bonding and small atomic mass result in large phonon group velocity, and the high crystal quality minimizes phonon defect scattering. Because of the significant challenges remained in the synthesis of high-quality diamond and graphitic materials and in their integration into electronic devices, there are active efforts in the search of other materials with potentially high

thermal conductivity. One recent theoretical calculation has predicted that the thermal conductivity of boron arsenide (BAs) can be comparable to the diamond value of $2270 \text{ Wm}^{-1} \text{ K}^{-1}$ at room temperature, and becomes higher than the diamond value at above room temperature. The origin of the high thermal conductivity in BAs is attributed to the large atomic mass ratio between B and As,² which results in a large energy gap between acoustic phonon branches with neighboring atoms vibrating in phase and optical branches with neighboring atoms vibrating out of phase. The large energy gap can suppress the scattering of acoustic phonons by the optical phonons, and result in long phonon-phonon scattering mean free path. This mechanism for the potentially ultrahigh thermal conductivity in BAs is different from that discussed above for diamond. Despite the encouraging theoretical prediction, there have been few experimental data on the thermal transport properties of BAs. In particular, the thermal conductivity of BAs can depend sensitively on the sample size, as phonon-boundary scattering can reduce the effective phonon mean free path especially when the phonon-phonon scattering mean free path is long.³ There is a lack of experimental data of such size effects on the thermal conductivity of BAs.

Besides high thermal conductivity materials, another approach to addressing the hot spot issue in electronic devices is to employ integrated Peltier coolers near the hot spots.⁴ In a Peltier cooler under an electrical bias, electrons in n-type semiconductors and holes in p-type semiconductors carry heat from the cold junction to the hot junction. In addition, Peltier devices can also be operated a reverse mode as a thermoelectric power generator to convert heat input into an electrical power. These solid state thermoelectric devices have several desirable features, such as the presence of few mechanical moving parts and heat transfer fluids. However, the energy conversion efficiency of these thermoelectric devices is limited by the thermoelectric figure of merit of the materials,

which is defined as $zT = S^2\sigma T/k$, where S , σ , k , and T are the Seebeck coefficient, electrical conductivity, thermal conductivity, and absolute temperature, respectively.

Bismuth telluride (Bi_2Te_3) alloys remain the most-widely used thermoelectric materials for commercial Peltier coolers, with a room temperature zT close to unity. A number of theoretical calculations have suggested that higher zT values can potentially be obtained in Bi_2Te_3 nanostructures because quantum confinement of electrons or the presence of topological protected surface electronic states can increase the power factor ($S^2\sigma$), while phonon-boundary scattering can suppress the phonon or lattice contribution to the thermal conductivity (k_l). Although increased zT to about 1.4 has been reported in nanocomposites of $\text{Bi}_{2-x}\text{Sb}_x\text{Te}_3$ and attributed to reduced k_l , enhanced power factor has not been observed in Bi_2Te_3 nanostructures.⁵⁻⁷

The development of several nanoscale thermal transport measurement methods have helped to obtain a better understanding of size-dependent thermal and thermoelectric properties in nanostructures. However, these transport measurement methods have limitation in their inability to eliminate the contact thermal resistance error from the measurement and obtain the intrinsic thermal transport properties. Such and other limitations in the current experimental capabilities have resulted in the lack of understanding of size-dependent thermal and thermoelectric properties of different materials including Bi_2Te_3 and BAs.

1.2 SCOPE OF WORK

This dissertation consists of three experimental works. Chapter 2 reports thermoelectric measurements of bismuth antimony telluride $(\text{Bi}_{1-x}\text{Sb}_x)_2\text{Te}_3$ nanostructure samples synthesized by two different methods, which are metal organic chemical vapor

deposition (MOCVD) and vapor solid growth in a tube furnace. The MOCVD grown sample is a thin film sample grown on a GaAs substrate with a thickness of 170nm and nominal $x=0.95$. The vapor transport grown samples are single crystalline thin $(\text{Bi}_{1-x}\text{Sb}_x)_2\text{Te}_3$ nanoplates. With the use of four-probe thermoelectric transport measurement method based on a suspended microdevice, the intrinsic Seebeck coefficient, thermal conductivity, and electrical conductivity of one MOCVD thin film sample and several nanoplate samples with different Sb content x are measured. The results are analyzed to understand the effects of chemical composition and size confinement on the thermoelectric properties.

Chapter 3 reports the development of new four probe thermal measurement method for measuring both the intrinsic thermal resistance and contact thermal resistance of a nanostructure sample. Compared to the four-probe thermoelectric measurement method presented in Chapter 2, this new four-probe thermal transport measurement method does not require electrical contact made to the sample, and can thus be applied to both conducting and insulating nanostructure samples. The method is demonstrated by measuring two patterned Si nanowire samples with different cross section areas. The results are compared to theoretical calculations. This new nanoscale thermal transport method can enable the discovery of the intrinsic size dependent thermal transport phenomena in nanostructures, especially those with potentially high thermal conductivity.

Chapter 4 reports the application of the new four probe thermal measurement method for measuring the intrinsic thermal transport properties of boron arsenide (BAs) nanorods. In addition, the four-probe method is further developed to measure the intrinsic thermoelectric properties of the BAs nanostructure sample. The obtained thermal and thermoelectric properties are analyzed and compared to theoretical calculation in order to better understand phonon transport in BAs.

Chapter 5 summarizes the major findings from the three experimental investigations presented in this dissertation.

REFERENCES

1. <http://www.itrs.net>.
2. L. Lindsay, D. A. Broido and T. L. Reinecke, *Physical Review Letters* 111 (2), 025901 (2013).
3. L. Lindsay, D. A. Broido and N. Mingo, *Physical Review B* 82 (16), 161402 (2010).
4. I. Chowdhury, R. Prasher, K. Lofgreen, G. Chrysler, S. Narasimhan, R. Mahajan, D. Koester, R. Alley and R. Venkatasubramanian, *Nat Nano* 4 (4), 235-238 (2009).
5. L. D. Hicks, T. C. Harman, X. Sun and M. S. Dresselhaus, *Physical Review B* 53 (16), R10493-R10496 (1996).
6. B. Poudel, Q. Hao, Y. Ma, Y. Lan, A. Minnich, B. Yu, X. Yan, D. Wang, A. Muto, D. Vashaee, X. Chen, J. Liu, M. S. Dresselhaus, G. Chen and Z. Ren, *Science* 320 (5876), 634-638 (2008).
7. R. Chen, A. I. Hochbaum, P. Murphy, J. Moore, P. Yang and A. Majumdar, *Physical Review Letters* 101 (10), 105501 (2008).

Chapter 2: Thermoelectric Transport in Bismuth Antimony Telluride Nanostructures

2.1 INTRODUCTION

Temperature gradients can be directly converted to electricity by solid state thermoelectric devices, which can be employed to recover waste heat from transportation vehicles and industrial processes. The efficiency of a thermoelectric device is limited by the thermoelectric figure of merit $zT = S^2 \sigma T / (k_e + k_l)$,¹ where S is the Seebeck coefficient, σ is the electrical conductivity, T is the absolute temperature, and k_e and k_l are the electronic and lattice contributions to the thermal conductivity, respectively. There have been many efforts to increase the zT by reducing the lattice thermal conductivity k_l , such as thin film superlattices and low dimensional materials.²⁻⁴ Another approach to increasing zT is to enhance the power factor ($S^2 \sigma$) by tuning the carrier concentration and Fermi level and modifying the electronic band structure.^{5, 6} Although bismuth Telluride (Bi_2Te_3) has been a well-known thermoelectric material for a long time, this material system is still under active investigations.^{7, 8} Alloying of Tellurides (Bi_2Te_3 , Sb_2Te_3 , PbTe , GeTe) has been employed to enhance the thermoelectric properties.⁹⁻¹¹ Bi_2Te_3 has also received attention recently because it is a layered material with quintuple structure (Te-Bi-Te-Bi-Te), and can be exfoliated or grown in two-dimensional shape. This and other two-dimensional layered materials are under active investigation for thermoelectric applications because thermoelectric properties can potentially be enhanced by electron confinement, surface electronic states, and phonon scattering.¹²⁻¹⁵

In this chapter, the effect of alloying of Bi_2Te_3 and Sb_2Te_3 is investigated. The thermoelectric properties of two types of $(\text{Bi}_{1-x}\text{Sb}_x)_2\text{Te}_3$ samples, synthesized by two

different methods, are characterized with a microfabricated device according to a four-probe thermoelectric measurement method. One sample is 170 nm thick film sample grown by metal organic chemical vapor deposition (MOCVD). The other one is single crystalline nanoplates grown by a catalyst free vapor solid process in tube furnace.¹⁶ The objective of the experiments is to employ alloying to vary the Sb content x to tune the electronic states so as to enhance the power factor ($S^2\sigma$).

2.2 SAMPLE PREPARATION

2.2.1 $\text{Bi}_{0.1}\text{Sb}_{1.9}\text{Te}_3$ film sample grown by MOCVD

The $\text{Bi}_{0.1}\text{Sb}_{1.9}\text{Te}_3$ film sample is grown by a metal organic chemical vapor deposition (MOCVD) method by researchers at Center for Solid State Energetics, RTI international.¹⁷ The film sample is grown on a piece of gallium arsenide (GaAs) wafer. The film thickness can be controlled during the growth. In this research, 170 nm thick $\text{Bi}_{0.1}\text{Sb}_{1.9}\text{Te}_3$ film sample is used for thermoelectric measurements. Prior measurements of similar $\text{Bi}_{0.1}\text{Sb}_{1.9}\text{Te}_3$ films still supported on a GaAs substrate suggest that high power factor ($S^2\sigma$) can be obtained. However, the thermal conductivity has not been measured on the same sample where the power factor is measured.

To measure the thermal conductivity, Seebeck coefficient, and electrical conductivity of the $\text{Bi}_{0.1}\text{Sb}_{1.9}\text{Te}_3$ film sample, the film sample is patterned and suspended before the sample is transferred onto a suspended device for four-probe thermoelectric measurements.¹⁸ The $\text{Bi}_{0.1}\text{Sb}_{1.9}\text{Te}_3$ film sample is patterned first with photo-lithography and reactive ion etch (RIE) process, and suspended with wet etch process of GaAs substrate. The RIE process is carried out in the Oxford ICP etcher with the gas mixture ratio of $\text{CH}_4:\text{H}_2:\text{Ar}=3:1:3$, and the photo-resist is stripped off with N-Methyl-2-

pyrrolidone (NMP) based solvent such as remover PG. The wet etch process of the GaAs substrate is done with the etchant mixture ratio of $\text{NH}_4\text{OH}:\text{H}_2\text{O}_2:\text{H}_2\text{O}=1:3:18$ for about 10-20 min. The ratio of the etchant is optimized to etch the GaAs substrate effectively and to minimize the damage to the $\text{Bi}_{0.1}\text{Sb}_{1.9}\text{Te}_3$ film sample. Figure 2.1 shows the patterned and suspended $\text{Bi}_{0.1}\text{Sb}_{1.9}\text{Te}_3$ film sample.

The suspended device used for thermoelectric measurements is a new design based on those reported previously.¹⁹ Figure 2.2 shows the device design and fabrication process. The device consists of two serpentine Pt supported on two suspended SiN_x membranes. Each Pt serpentine is connected to four Pt leads supported on long suspended SiN_x beams for four-probe electrical measurement of the electrical resistance of the serpentine, which depends on the temperature so that the serpentine can be used as a heater and a thermometer. Each serpentine is covered by a thin HfO_2 insulating layer, on top of which two additional Pd contact pads are deposited, and connected to two Pt leads supported by long SiN_x beams. The four Pt contact pads on the two membranes allow for four-probe electrical measurement of a nanostructure suspended between the two membranes. Moreover, they can be used to measure the thermovoltage drops along different segments of the nanostructure when one Pt serpentine is electrically heated to generate a temperature gradient along the sample. The measured thermovoltage drops can be used to determine the temperature drops along the suspended and supported segments of the nanostructure, so that both the contact thermal resistance and intrinsic thermal resistance and Seebeck coefficient of the suspended segment of the nanostructure can be obtained, as discussed in details in a prior work.¹⁸

The patterned $\text{Bi}_{0.1}\text{Sb}_{1.9}\text{Te}_3$ film sample can be assembled on the pre-fabricated suspended device with the use of a polymethyl methacrylate (PMMA) carrier layer. Figure 2.3 shows the process of transferring and aligning a patterned $\text{Bi}_{0.1}\text{Sb}_{1.9}\text{Te}_3$ film

sample on a prefabricated suspended device. The patterned and suspended film sample is picked up with a sharp Tungsten probe controlled by a XYZ micro manipulator, and transferred on a piece of substrate coated with water soluble polyvinyl alcohol (PVA). Thick PMMA is spin coated on this piece of substrate with the $\text{Bi}_{0.1}\text{Sb}_{1.9}\text{Te}_3$ film sample. The film sample adheres to the PMMA very well. The PVA layer is dissolved in deionized water, so that the PMMA layer with the film sample floats on the water. This relatively large PMMA layer is transferred with the sharp probe on a pre-fabricated suspended device, and aligned by the XYZ micro manipulator. After the alignment of the sample, the whole assembly is thermally annealed at 180°C in tube furnace, which is maintained at the pressure of 1 Torr with Ar atmosphere, to enhance the adhesion between the sample and the suspended device and to release the stress which causes warping of the sample. The PMMA layer can be removed by dipping the device in acetone after the annealing process. After two narrow SiN_x connecting bars are broke using the sharp probe or a focused laser beam, the sample preparation is completed to obtain a measurement device with the film sample suspended between the two membranes, as shown in figure 2.4.

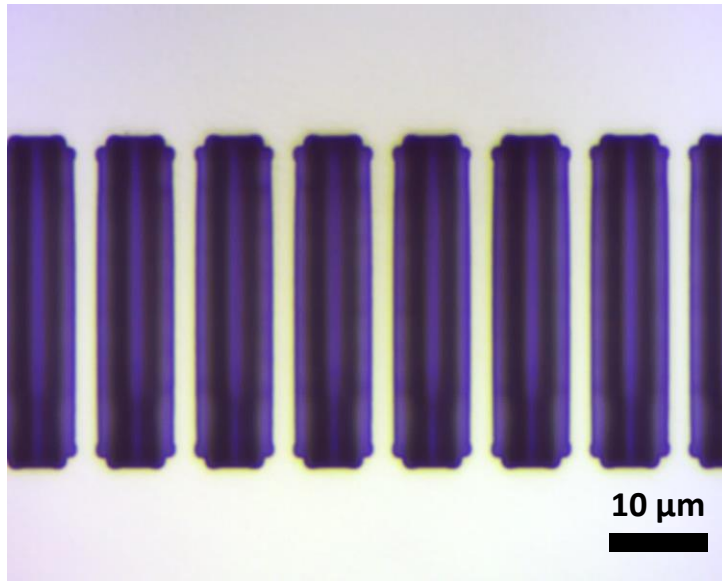


Figure 2.1: A 170 nm thick $\text{Bi}_{0.1}\text{Sb}_{1.9}\text{Te}_3$ film sample grown on GaAs substrate is patterned by photo lithography and reactive ion etching, and suspended after wet etching of the GaAs substrate.

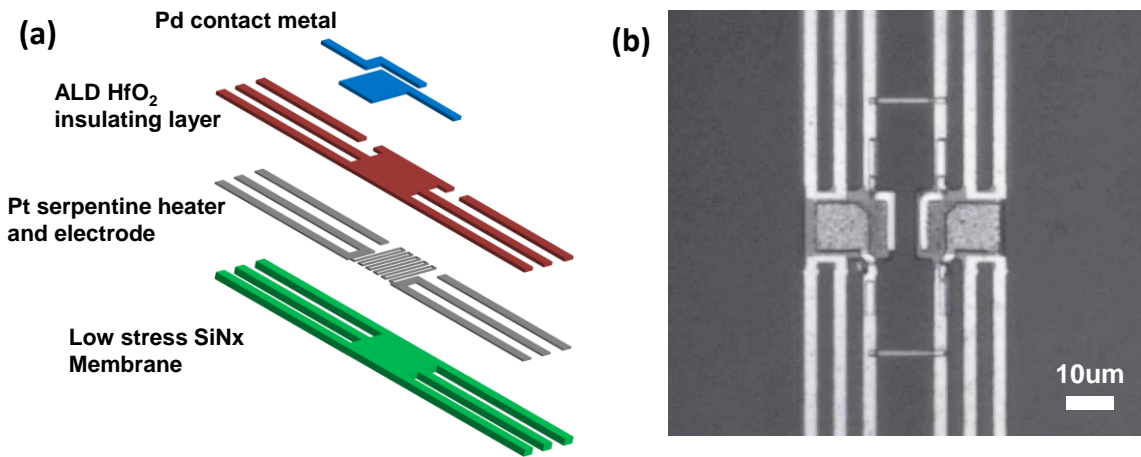


Figure 2.2: Structure of the 6-beam suspended measurement device (a), and an optical micrograph of a fabricated device before a sample is assembled on the device (b).

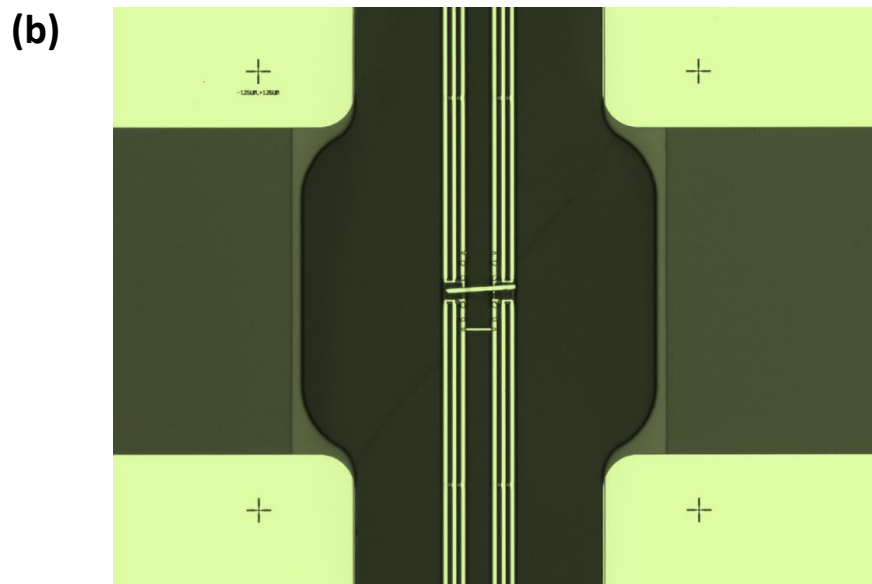
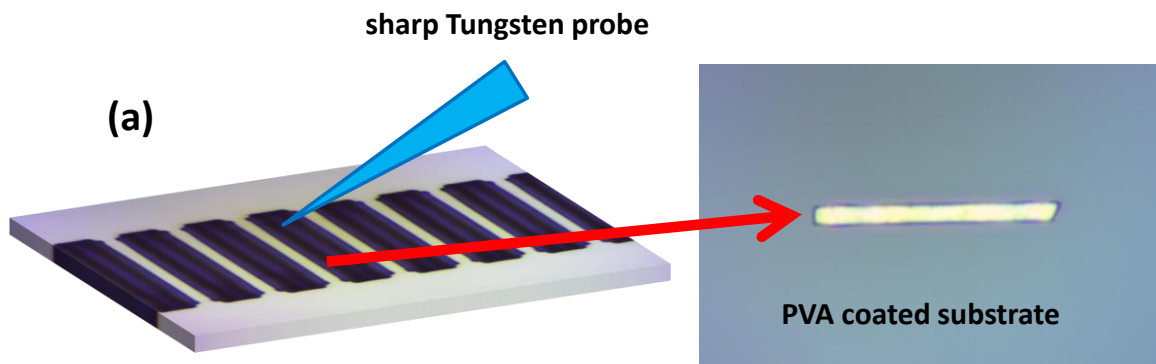


Figure 2.3: Patterned $\text{Bi}_{0.1}\text{Sb}_{1.9}\text{Te}_3$ film sample is picked up with a sharp tungsten probe, and transferred on a piece of a Si substrate coated with a PVA layer (a). After the PMMA layer is spin coated on the sample, the PMMA layer together with the film sample is transferred and aligned on a pre-fabricated suspended device (b).

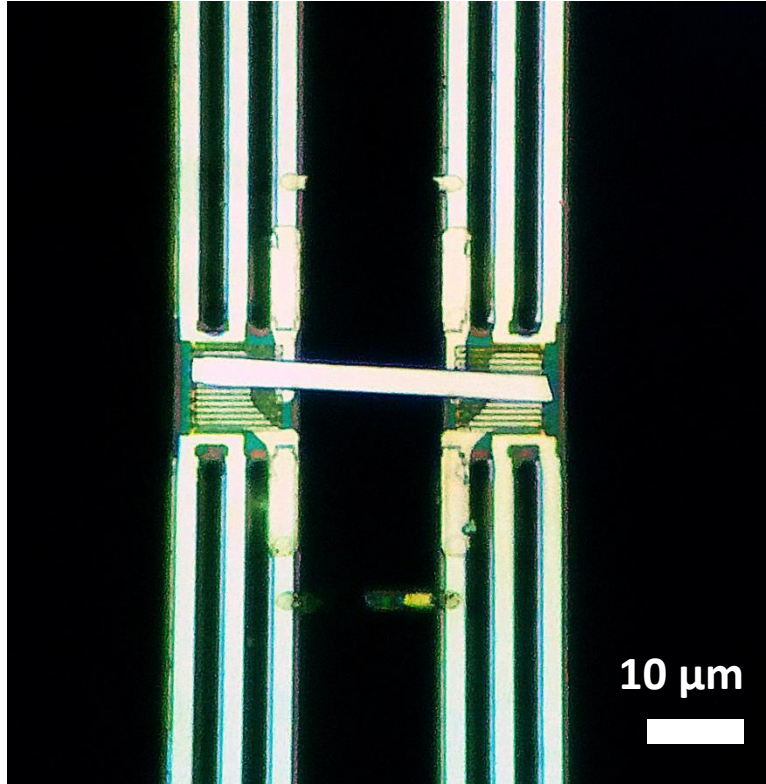


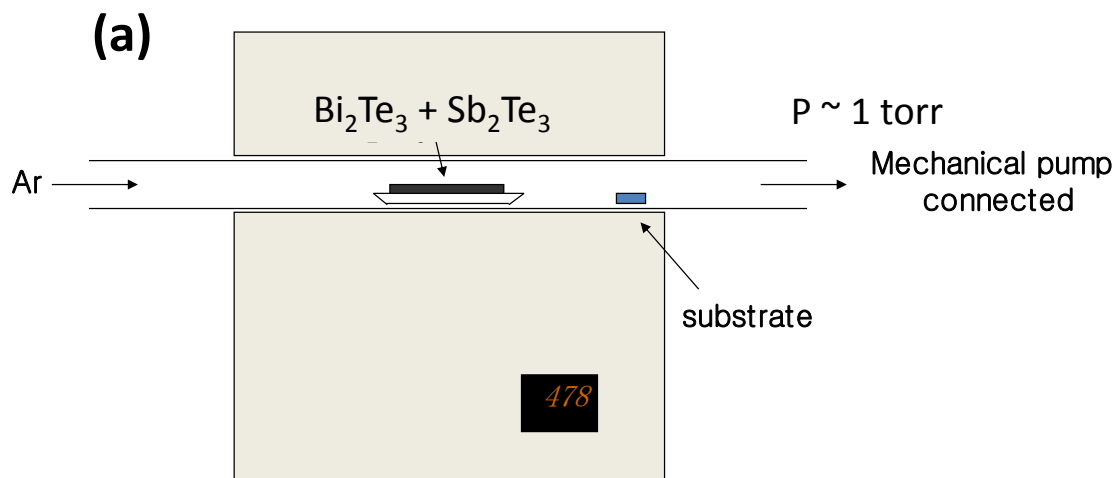
Figure 2.4: Optical micrograph of a 170nm thick $\text{Bi}_{0.1}\text{Sb}_{1.9}\text{Te}_3$ film sample assembled on a pre-fabricated suspended device for thermoelectric measurement.

2.2.2 Nanoplates grown by vapor solid method

Two-dimensional $(\text{Bi}_x\text{Sb}_{1-x})_2\text{Te}_3$ thin crystal plates with various Sb content x are grown by catalyst free vapor solid method in a tube furnace.¹⁶ Figure 2.5 (a) shows the schematic diagram of the growth system. Source materials of Bi_2Te_3 and Sb_2Te_3 are located at the center of the quartz tube, and a piece of Si wafer with 300 nm thick surface SiO_2 is located at the end part of the furnace, which is at a lower temperature than the temperature of source materials. The temperature of the furnace is maintained at 478 °C

for 3 hours, and is slowly cooled down for 12 hours to room temperature. After the growth, many $(\text{Bi}_x\text{Sb}_{1-x})_2\text{Te}_3$ crystal plates can be found on the Si substrate, as shown in figure 2.5 (b). Some of them stick out of the surface of substrate, so that they can be picked up with a sharp tungsten probe. The picked up sample is transferred directly onto the pre-fabricated device by a XYZ micro manipulator under the microscope.

Figure 2.6 (a), (b) show completed devices ready to be measured with $(\text{Bi}_{1-x}\text{Sb}_x)_2\text{Te}_3$ sample of $x=0.7$ and $x=0.95$, respectively, where x is determined based on the ratio in the source material instead of in the synthesized nanoplates. Upon the completion of the thermoelectric measurements, atomic force microscopy (AFM) is used to measure the thickness of the $(\text{Bi}_{1-x}\text{Sb}_x)_2\text{Te}_3$ plate assembled on the device. Figure 2.6 (c), (d) show the AFM images of the sample with $x = 0.7$ and 0.95 , respectively. Five samples of different Sb content $x = 0.07, 0.25, 0.5, 0.7,$ and 0.95 have been transferred and measured in this work. Among them, three samples of $x=0.07, 0.25,$ and 0.5 are measure by Michael T. Pettes in same research group.



- (b)**
- Tungsten probe
 - XYZ micro manipulator

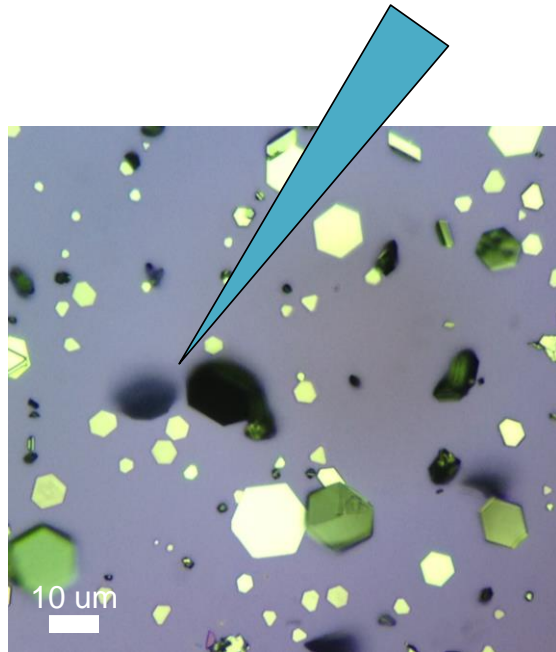


Figure 2.5: The vapor solid growth setup for $(\text{Bi}_{1-x}\text{Sb}_x)_2\text{Te}_3$ (a). The nanoplate samples can be picked up and transferred on a device by a sharp tungsten probe (b).

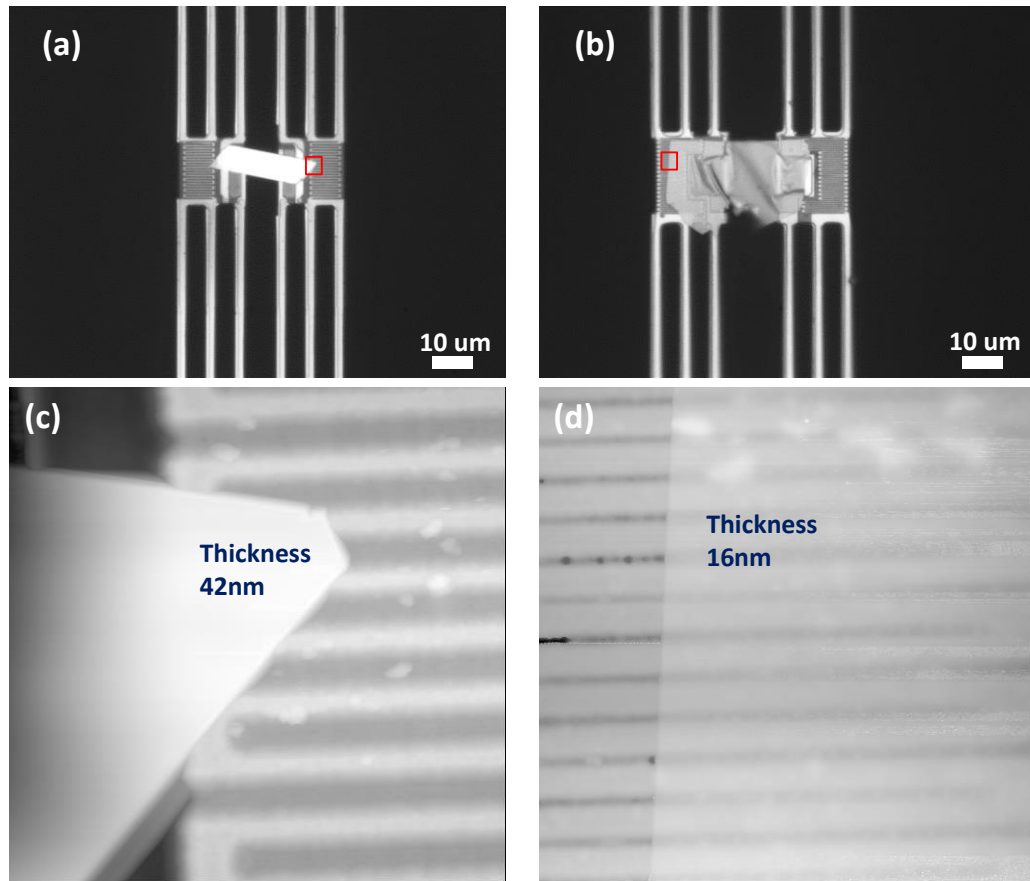


Figure 2.6: Optical micrographs for $(\text{Bi}_{1-x}\text{Sb}_x)_2\text{Te}_3$ nanoplates of $x=0.7$ (a), and $x=0.95$ (b). AFM images (c and d) of the areas indicated as a red square in (a) and (b).

2.3 MEASUREMENT RESULTS

2.3.1 Bi_{0.1}Sb_{1.9}Te₃ film sample grown by MOCVD

Thermoelectric measurement is carried out in the temperature range from 100 to 350K. Figure 2.7 shows a schematic diagram of the measurement setup. One membrane is heated by a direct current (I_{DC}), which is ramped from 0 to -20 μ A, -20 μ A to +20 μ A, and +20 μ A to 0 with 203 steps per ramping cycle. The Joule heating results in an increase of the electrical resistance (R_e) of each Pt serpentine, which is measured with a small sinusoidal current (i_{ac}) and a lock-in amplifier. For the heating membrane where I_{DC} flows, the frequency of the i_{ac} coupled to the I_{DC} needs to be sufficiently high, typically about 2kHz, so that the first harmonic heating term ($2I_{DC}i_{ac}R_e$) is fast compared to the thermal time constant of the device and the resulted first harmonic temperature rise in the heating membrane is negligible.¹⁹ In this case, the electrical resistance of the heating Pt serpentine can be obtained directly as v_{ac}/i_{ac} , where v_{ac} is the first harmonic component of the measured voltage drop over the Pt serpentine. In comparison, such frequency requirement is not necessary for the other sensing Pt serpentine without the heating current. The measured increase in R_e of each Pt serpentine can be used to obtain the temperature rise in each Pt serpentine based on the measured temperature coefficient of resistance of each Pt serpentine. In addition, the thermovoltage drops between the two Pd inner electrodes and that between the two outer electrodes are measured simultaneously during the ramping cycle. Figure 2.8 shows the measured temperature rise of each Pt serpentine as a function of the heating current, and the thermovoltage drops as a function of the temperature differences between the two serpentes. The ratio of two themovoltage drops, $\gamma=S_{14}/S_{23}=(T_1-T_4)/(T_2-T_3)$, can be used to determine and eliminate the contact thermal resistance by assuming a fin temperature profile with constant heat conductance at the thermal contact, and uniform temperature on each membrane.¹⁸

Because γ gives the information of actual temperature on different points of the sample, the temperature profile can be obtained from the fin temperature profile. From the temperature profile, the intrinsic Seebeck and thermal resistance of the sample can be determined.

Figure 2.9 shows the measured thermal conductivity and Seebeck coefficient of the $\text{Bi}_{0.1}\text{Sb}_{1.9}\text{Te}_3$ film sample. The thermal conductivity is about $2 \text{ Wm}^{-1}\text{K}^{-1}$ and approximately independent of temperature between 100 and 350 K. The electronic contribution to the total thermal conductivity is calculated from the measured electrical conductivity by the Wiedemann-Franz law.

The measured Seebeck coefficient is positive, revealing that the sample is a p-type semiconductor. The measured Seebeck coefficient increases nearly linearly with the temperature, with a value of $89 \mu\text{V/K}$ at 300K. Together with the decreasing electrical conductivity with increasing temperature, the linear temperature dependence of the Seebeck coefficient reveals that the sample is degenerately p-doped. Figure 2.10 shows the thermoelectric figure of merit (zT) calculated from the three measured thermal and thermoelectric properties. It is worth noting that the thermoelectric properties of $(\text{Bi}_{1-x}\text{Sb}_x)_2\text{Te}_3$ can depend sensitively on the processing conditions. In particular, the 180°C annealing process used in the sample preparation process could have potentially altered the chemical composition in the materials with relatively low melting temperature and high vapor pressure for constituent elements. As such, the measured thermoelectric properties can differ from those measured on the original thin film supported on the GaAs substrate.

The measurement results can be used to better understand the lattice and electronic contributions to the thermal conductivity. According to a single parabolic

band model, the measured Seebeck coefficient can be used to extract the, Fermi level, hole carrier concentration, and Lorenz number ($L = k_e / \sigma T$) according to

$$S = \frac{k_B}{e} \left\{ \frac{(r_p + \frac{5}{2})F_{r_p+3/2}(\eta)}{(r_p + \frac{3}{2})F_{r_p+1/2}(\eta)} - \eta \right\} \quad (1), \quad F_r(\eta) = \int_0^\infty \frac{\zeta^r}{\exp(\zeta - \eta) + 1} d\zeta \quad (2)$$

$$p = \frac{(2m_p^* k_B T)^{\frac{3}{2}}}{2\pi^2 \hbar^3} F_{\frac{1}{2}}(\eta) \quad (3), \quad L = \left(\frac{k_B}{e}\right)^2 \left\{ \frac{3F_2(\eta)}{F_0(\eta)} - \frac{4F_1(\eta)^2}{F_0(\eta)^2} \right\} \quad (4)$$

where the reduced Fermi level $\eta = E_F / k_B T$, and $r_p = -1/2$ for acoustic phonon and boundary scattering dominant condition. The calculation values are shown in Figure 2.11. The Fermi level is referenced at valence band edge, and positive Fermi energy refers to the case that the Fermi level is located below the valence band edge. The hole concentration is close to order of 10^{20} cm^{-3} , confirming that the sample is highly degenerate.

The obtained Lorenz number at 100K is close to the value of metallic limit, and decreasing with the increasing temperature. The obtained Lorenz number is used together with the measured electrical conductivity to calculate the electronic contribution (k_e) to the thermal conductivity according to the Wiedemann–Franz law. The obtained k_e is then subtracted from the measured total thermal conductivity to obtain the lattice thermal conductivity (k_l). As shown in Fig. 2.9, the obtained k_e and k_l are comparable to each other, and are insensitive to temperatures in the range between 100 and 350 K.

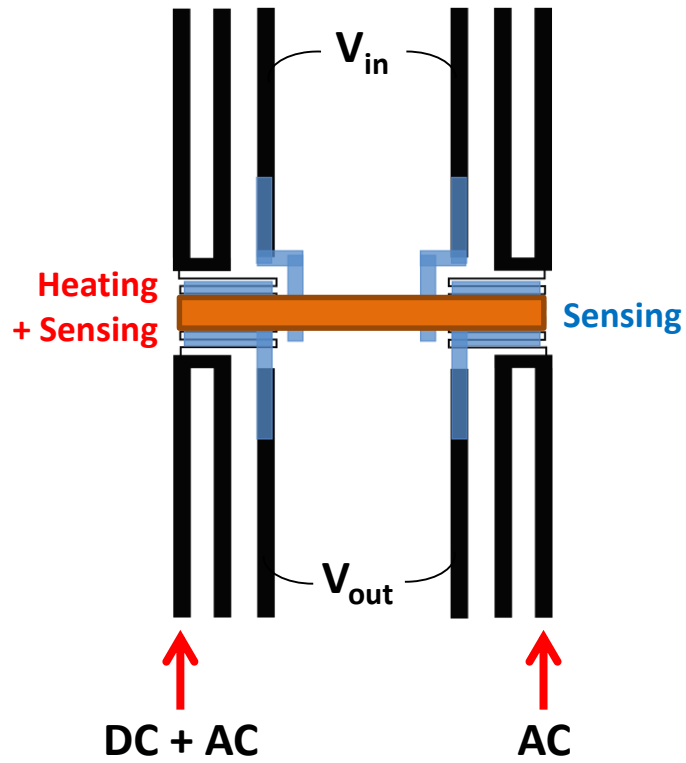


Figure 2.7: Schematic diagram of a measurement device. Each serpentine Pt line is used as a resistive heater and thermometer. Heating is made by direct current (DC), and temperature is measured by alternating current (AC).

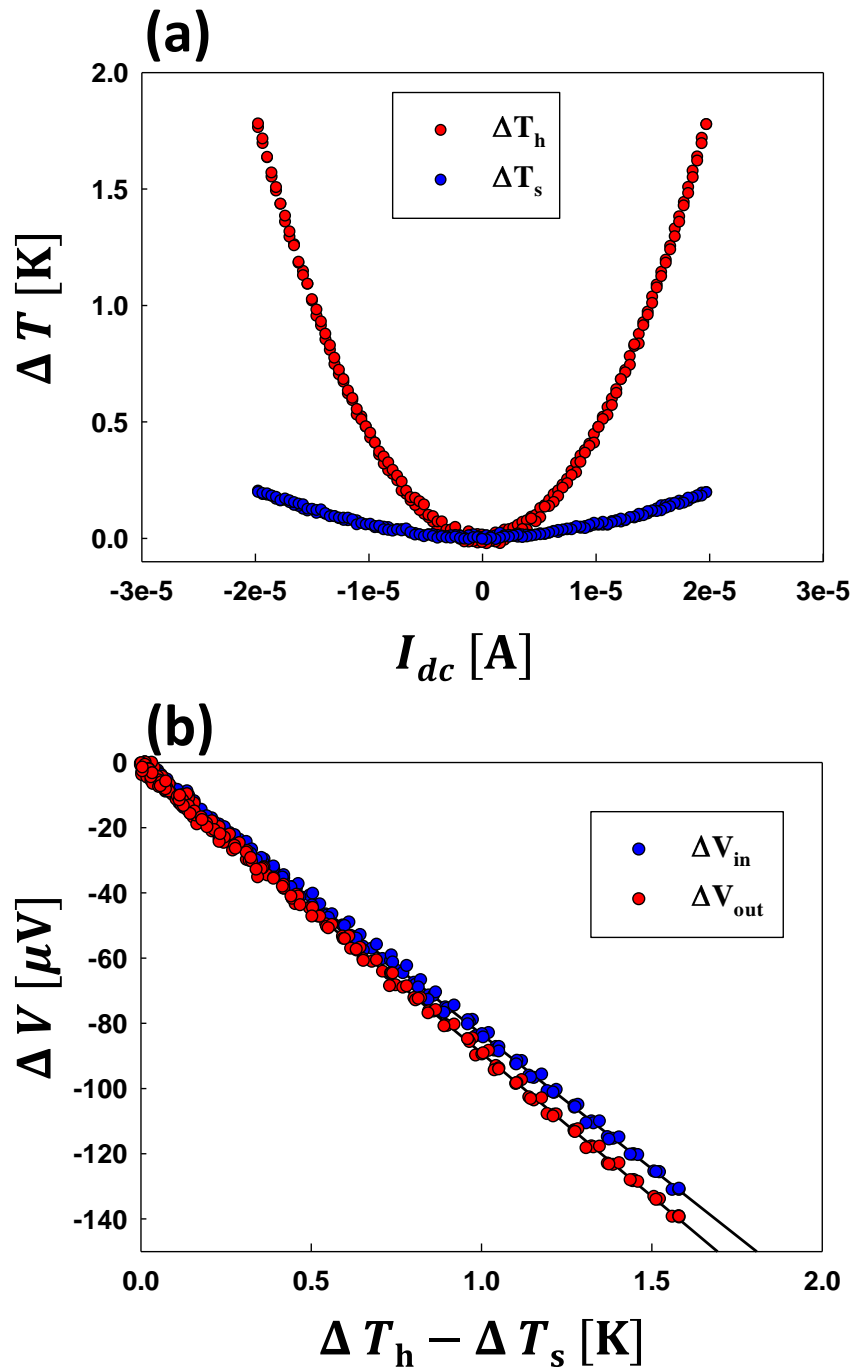


Figure 2.8: Measured temperature of each membrane (a), and thermovoltage drops of inner and outer electrodes as a function of temperature difference (b).

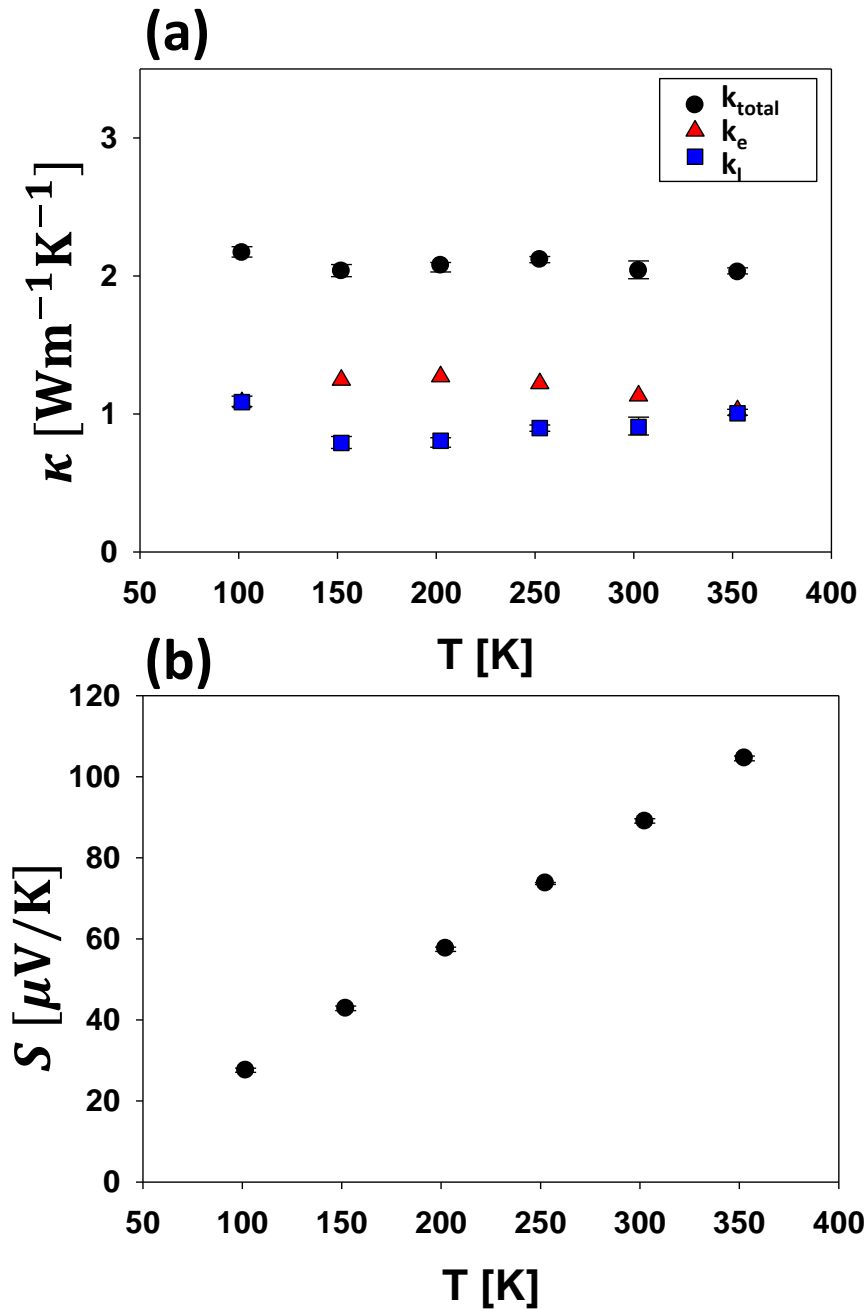


Figure 2.9: Measured thermal conductivity (a) and Seebeck coefficient (b) as a function of temperature.

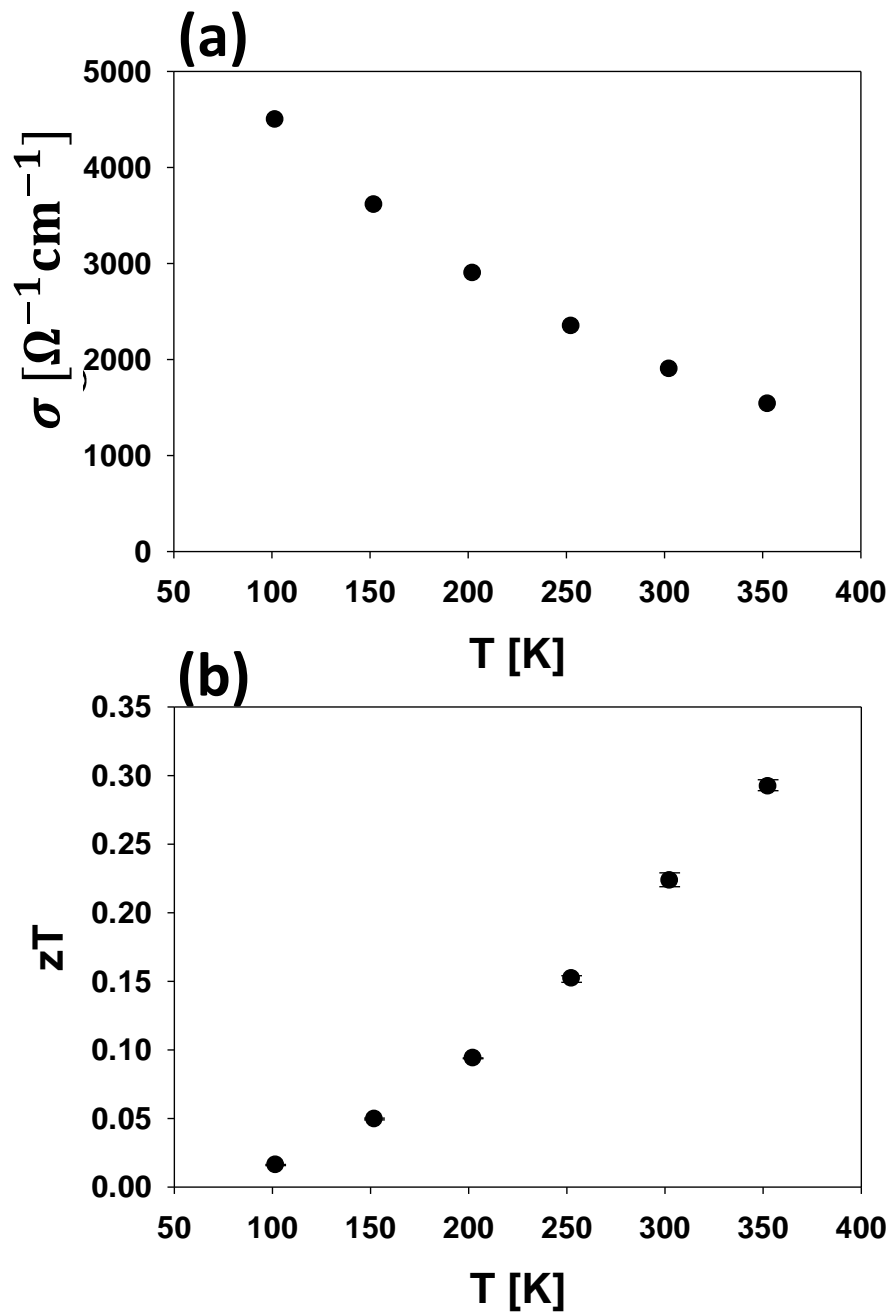


Figure 2.10: Measured electrical conductivity (a) and thermoelectric figure of merit zT (b) as a function of temperature.

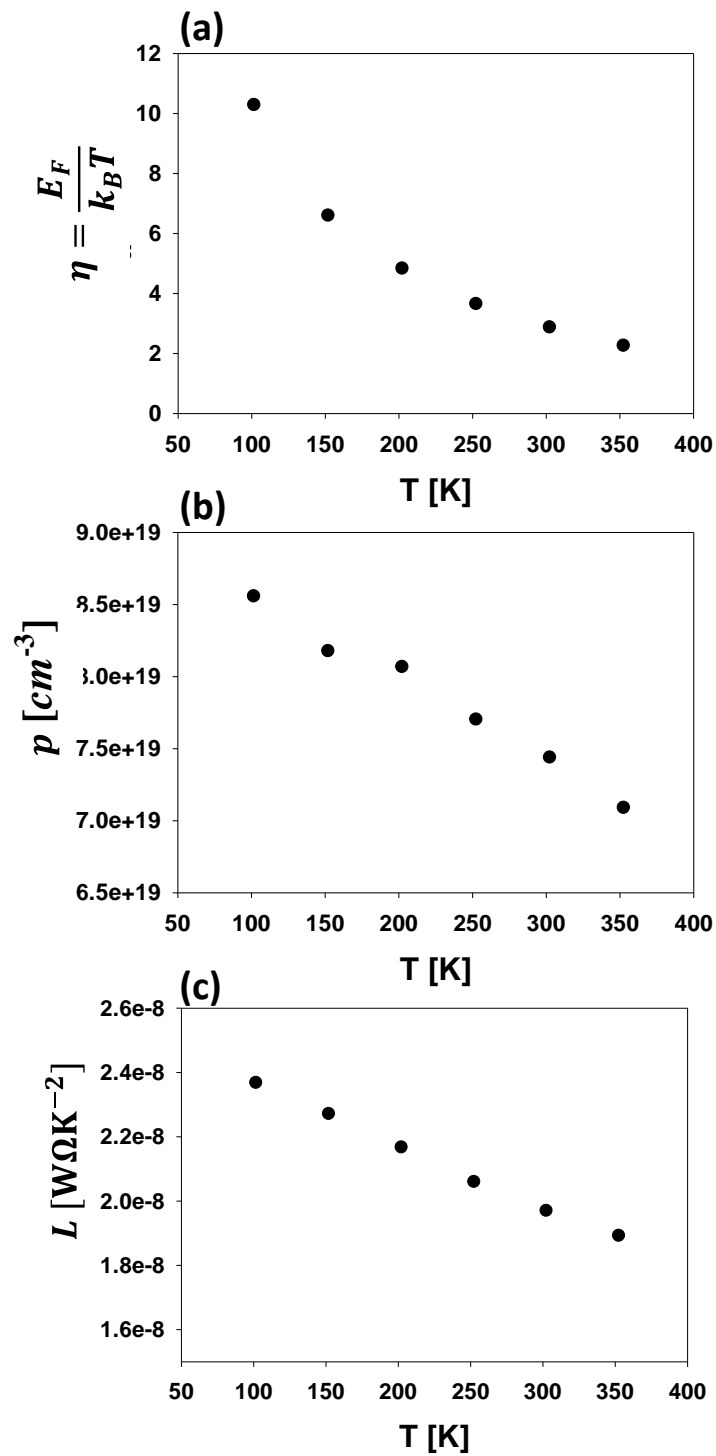


Figure 2.11: Calculated reduced Fermi level (a), hole carrier concentration (b), and Lorenz number (c) based on the measured Seebeck coefficient.

2.3.2 Nanoplates grown by vapor solid method

Figure 2.12 and figure 2.13 show the measured Seebeck coefficient (S) and thermoelectric figure of merit (zT) of five $(\text{Bi}_x\text{Sb}_{1-x})_2\text{Te}_3$ thin crystal plate samples with different Sb concentration as a function of the Sb content x and temperature, respectively. It is worth noting that the five samples have different layer thickness. The thinner samples can be affected more by surface scattering and surface electronic states. A previous work has suggested that surface band bending occurred in thin Bi_2Te_3 nanoplates exposed to air and resulted in suppressed Seebeck coefficient.²⁰ Despite the difference in the sample thickness and potentially different degrees of the surface effects, the obtained thermoelectric properties still reveal some clear dependence on Sb content in $(\text{Bi}_x\text{Sb}_{1-x})_2\text{Te}_3$ thin crystal plates. For example, the measured Seebeck coefficient changes sign from a negative value to a positive value at x between 0.07 and 0.25, suggesting a change of the majority charge carriers from electrons to holes. The magnitude of the Seebeck coefficient of these five compositions reach a peak value of about 120 $\mu\text{V}/\text{K}$ at a Sb concentration near $x = 0.5$, where the highest zT value of 0.25 has been measured among these samples.

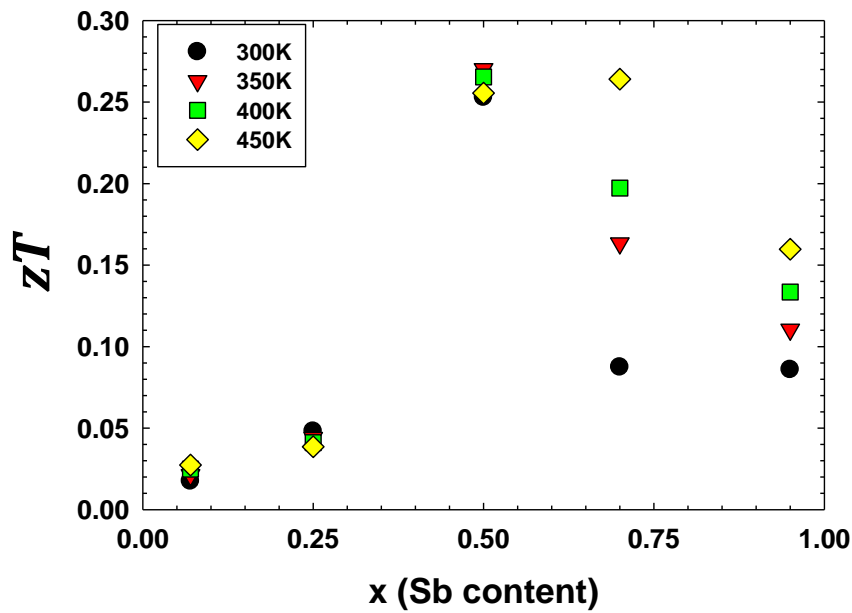
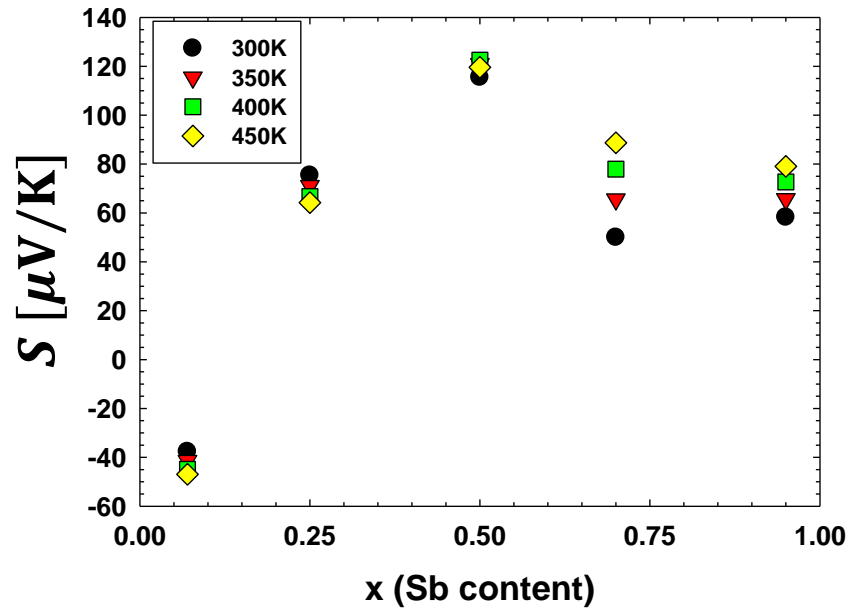


Figure 2.12: Measured Seebeck coefficient (a) and thermoelectric figure of merit zT (b) as a function of Sb content x . Some of data points are measured by Michael T. Pettes in same research group.

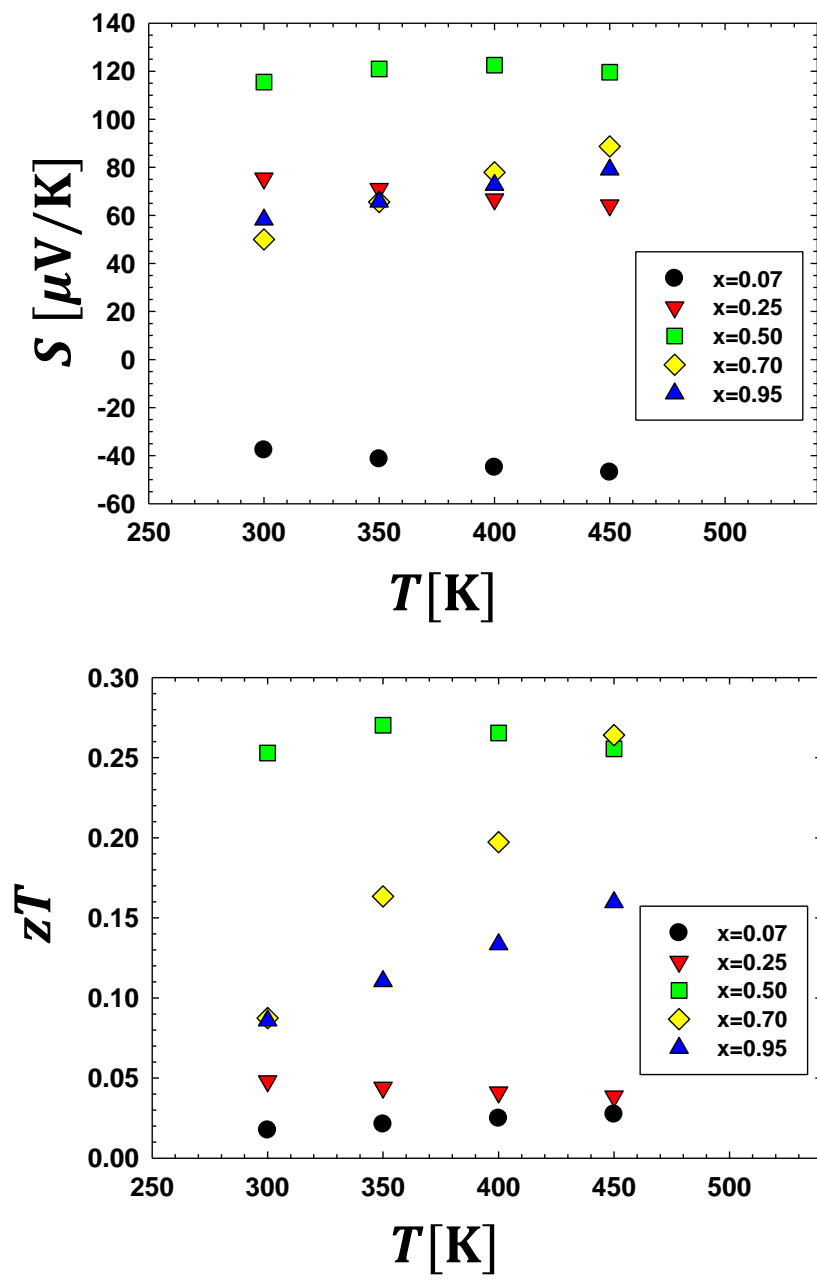


Figure 2.13: Measured Seebeck coefficient (a) and thermoelectric figure of merit zT (b) as a function of temperature. Some of data points are measured by Michael T. Pettes in same research group.

2.4 SUMMARY

The thermoelectric properties of two types of bismuth antimony telluride samples synthesized by different growth methods have been measured in this work. For $\text{Bi}_{0.1}\text{Sb}_{1.9}\text{Te}_3$ film samples grown by MOCVD method with 170 nm thickness, the sample is patterned, and suspended and transferred with a PMMA carrier layer on a suspended device for four-probe thermoelectric measurements in the temperature range between 100K and 350K. The Seebeck coefficient is positive and increases approximately linearly with increasing temperature. In addition, the electrical conductivity decreases with increasing temperature. These trends suggest that the sample is degenerately p-doped. With the use of a single parabolic band model, the measured Seebeck coefficient is used to calculate a hole concentration to be about the order of 10^{20} cm^{-3} . In addition, the thermal conductivity is about $2 \text{ Wm}^{-1}\text{K}^{-1}$ and insensitive to temperatures in the temperature range. The lattice contribution to the thermal conductivity is comparable to the electronic contribution, which is determined from the Wiedemann–Franz law, where the Lorenz number is obtained from the single parabolic band model and the measured thermoelectric properties..

For $(\text{Bi}_{1-x}\text{Sb}_x)_2\text{Te}_3$ nanoplate samples grown by vapor solid method in a tube furnace with different Sb concentration x , the nanoplates is directly picked up and transferred with a sharp tungsten probe onto the measurement device to eliminate the PMMA transfer and annealing step, which could potentially alter the chemical composition and thermoelectric properties of the MOCVD sample. The measurement results show that the sign of Seebeck coefficient changes from negative to positive at x between 0.07 and 0.25, corresponding to a change of the majority charge carrier type from electrons to holes. The maximum value of Seebeck coefficient and thermoelectric figure of merit zT appear at $x=0.5$. These results and the established experimental

methods provide a solid foundation to further investigating the size and composition dependence in the thermoelectric properties of this and other families of thermoelectric materials.

REFERENCES

1. D. M. Rowe, *CRC Handbook of Thermoelectrics*. (Taylor & Francis, 1995).
2. R. Venkatasubramanian, E. Siivola, T. Colpitts and B. O'Quinn, *Nature* 413 (6856), 597-602 (2001).
3. T. C. Harman, P. J. Taylor, M. P. Walsh and B. E. LaForge, *Science* 297 (5590), 2229-2232 (2002).
4. G. Chen and M. Neagu, *Applied Physics Letters* 71 (19), 2761-2763 (1997).
5. G. D. Mahan and J. O. Sofo, *Proceedings of the National Academy of Sciences* 93 (15), 7436-7439 (1996).
6. V. L. Kuznetsov, L. A. Kuznetsova, A. E. Kaliazin and D. M. Rowe, *Journal of Materials Science* 37 (14), 2893-2897 (2002).
7. T. M. Tritt and M. A. Subramanian, *MRS Bulletin* 31 (03), 188-198 (2006).
8. G. J. Snyder and E. S. Toberer, *Nat Mater* 7 (2), 105-114 (2008).
9. P. F. P. Poudeu, J. D'Angelo, H. Kong, A. Downey, J. L. Short, R. Pcionek, T. P. Hogan, C. Uher and M. G. Kanatzidis, *Journal of the American Chemical Society* 128 (44), 14347-14355 (2006).
10. Z. Pinwen, I. Yoshio, I. Yukihiro, S. Yoshikazi, J. Xiaopeng and Z. Guangtian, *Journal of Physics: Condensed Matter* 17 (46), 7319 (2005).
11. D. Kusano and Y. Hori, *Journal of the Japan Institute of Metals* 66 (10), 1063-1065 (2002).
12. R. Kim, S. Datta and M. S. Lundstrom, *Journal of Applied Physics* 105 (3), 034506 (2009).
13. L. D. Hicks and M. S. Dresselhaus, *Physical Review B* 47 (19), 12727-12731 (1993).
14. V. Goyal, D. Teweldebrhan and A. A. Balandin, *Applied Physics Letters* 97 (13), 133117 (2010).
15. P. Ghaemi, R. S. K. Mong and J. E. Moore, *Physical Review Letters* 105 (16), 166603 (2010).

16. *D. Kong, W. Dang, J. J. Cha, H. Li, S. Meister, H. Peng, Z. Liu and Y. Cui, Nano Letters 10 (6), 2245-2250 (2010).*
17. *H. Cao, R. Venkatasubramanian, C. Liu, J. Pierce, H. Yang, M. Zahid Hasan, Y. Wu and Y. P. Chen, Applied Physics Letters 101 (16), 162104 (2012).*
18. *A. Mavrokefalos, M. T. Pettes, F. Zhou and L. Shi, Review of Scientific Instruments 78 (3), 034901 (2007).*
19. *L. Shi, D. Li, C. Yu, W. Jang, D. Kim, Z. Yao, P. Kim and A. Majumdar, Journal of Heat Transfer 125 (5), 881-888 (2003).*
20. *M. T. Pettes, J. Maassen, I. Jo, M. S. Lundstrom and L. Shi, Nano Letters 13 (11), 5316-5322 (2013).*

Chapter 3: A novel four-probe thermal transport measurement method for nanostructures

This chapter describes a novel four-probe thermal transport measurement method for nanostructured materials such as nanowires, nanorods, and nanoribbons. A unique feature of this measurement method is its capability of separating the contact thermal resistances and intrinsic thermal resistance of the nanostructured sample. The measurement device is composed of four suspended resistant thermometer lines, and the nanostructured sample is located across all four suspended¹ thermometers. The heat flow through each thermal contact is different from the heat flow through the sample, which allows for the separation of the contact thermal resistances and intrinsic thermal resistance. Single crystalline silicon nanowire samples of two different cross section areas are measured to demonstrate the effectiveness of the measurement method. Because this new four-probe thermal transport measurement method can yield accurate experimental data for calibrating theoretical models, it can potentially play an important role in the investigation of unique size dependent thermal transport phenomena of nanostructured materials, which continue to be synthesized or discovered by the nanomaterials research society.

3.1 INTRODUCTION

There have been active developments of nanofabrication and synthesis methods for nanostructured materials, such as nanowires, nanorods, carbon nanotubes, and graphene. The characteristic lengths of these nanomaterials are comparable to the

Jaehyun Kim, Eric Ou, Daniel P. Sellan, Li Shi, *A four-probe thermal transport measurement method for nanostructures*. Review of Scientific Instruments, 2015. **86**(4): p. 044901.

LS and JK conceived the main concept behind the measurement method. JK and EO fabricated the measurement devices. JK carried out the thermal measurements. EO, JK, and LS carried out thermal conductivity modeling. DPS contributed to the development of the measurement method and assisted in early stage of the experiments.

scattering mean free path or wavelength of the charge or heat carriers. As such, they can exhibit unique size-dependent electrical and thermal transport properties compared to the bulk counterparts. For example, elimination of inter-layer interaction is expected to result in enhanced basal plane thermal conductivity of clean suspended single-layered graphene (SLG) and single-walled carbon nanotubes (SWCNTs) compared to the already high values found for graphite.¹ Scattering is especially suppressed for low-frequency phonons in clean suspended SLG and SWCNTs, so that the thermal conductivity contribution from these long-wavelength modes can be limited mainly by scattering at the lateral edges instead of phonon-phonon processes.² Exploring size dependent thermal properties can enhance understanding of thermal transport physics and is relevant to thermal management of integrated electronic devices or thermoelectric energy conversion devices.

Several experimental methods were developed to measure thermal transport properties of nanostructured materials such as nanowires, carbon nanotubes, nanoribbons, graphene, and other low dimensional materials.³⁻²¹ These methods employ various kinds of thermometry techniques, including suspended micro devices with resistive thermometry, Raman spectroscopy, thermal reflectance, and bimaterial cantilevers.²² The development of these thermal measurement techniques has remarkably enhanced the capability in understanding nanoscale thermal transport physics. However, there are several important limitations in the existing nanoscale thermal transport measurement methods.²³⁻²⁵ Among these limitations, the contact thermal resistance between the nanostructured sample and the measurement device has been a major source of error. Without separating the contact thermal resistances from the measurement results, there have been critical questions on the exact cause of the length dependent thermal

conductivities or abnormally low thermal conductivity values reported from a number of measurements on nanostructured materials.

There are several reported measurement methods for probing independently both contact thermal resistance and intrinsic thermal resistance of nanostructured sample. One method is using the measured thermovoltage drops along the contact and suspended segments of a nanostructure sample to determine the contact thermal resistance of the nanostructure suspended between two serpentine Pt resistance thermometers on two suspended membranes.¹¹ Specifically, there are two Pt electrodes in contact with the nanostructure on each of the two membranes of the measurement device. The thermovoltage drop along different segments of the nanostructure can be measured between any two of the four Pt electrodes. The difference of the thermovoltage drops measured between the outer contacts and the inner contacts of the sample is used to determine temperature drop at the contacts and contact thermal resistance. This method is effective only for electrically conducting sample with a large and uniform Seebeck coefficient compared to the Pt electrodes, and requires ohmic electrical contact between Pt electrodes and the nanostructured sample. Another method employs focused laser or electron beam heating on the suspended nanostructured sample, and measures spatial distribution of the thermal resistances along the sample by moving the heating beam along the sample.^{9, 26} However, focused laser or electron beam can also damage the nanostructured sample and change thermal properties of the sample. In addition, it remains a challenge to employ this rather complicated method to measure thermal transport properties in the low temperature range where many interesting thermal transport phenomena may exist. Because of the limitations and complications in these existing nanoscale thermal transport measurement methods, there is a need to establish

new methods for measuring both the contact thermal resistance and intrinsic thermal resistance of a nanostructured sample in a wide temperature range.

In this chapter, a novel four-probe thermal transport measurement method is presented. This method is able to probe independently both the contact thermal resistances and intrinsic thermal resistance of the nanostructured sample. The effectiveness of the method is demonstrated with two Si nanowire samples with different cross section areas, and the measurement results are compared to theoretical models.

3.2 MEASUREMENT METHOD

The device for the four-probe thermal measurement consists of four suspended Pt/SiN_x resistance thermometer lines (RT1, RT2, RT3, and RT4) with a nanostructured sample assembled across all four RTs as shown in figure 3.1. One of the four Pt/SiN_x line (i^{th} line) is electrically heated by a direct current (I), and the average temperature rise ($\bar{\theta}_{j,i}$) in the j^{th} Pt/SiN_x line is measured from the thermally induced increase of the electrical resistance of the line measured with a four probe configuration.^{27, 28} By changing both i and j from 1 to 4, a total of 16 measurement data of the $\bar{\theta}_{j,i}/(IV)_i$ ratio can be obtained, where V and $(IV)_i$ are the measured voltage drop and Joule heating rate in the i^{th} heating line, respectively. From these 16 measurement data, we can determine nine of the eleven thermal resistances in the system shown in the thermal resistance circuit of Figure 3.2, including the two contact thermal resistances ($R_{c,2}$ and $R_{c,3}$) and the intrinsic thermal resistance (R_2) of the nanostructured sample.

The temperature rise at the contact point of the j^{th} thermometer line ($\theta_{c,j,i}$) can be obtained from the measured average temperature rise $\bar{\theta}_{j,i}$ when the i^{th} line is electrically heated. The temperature distribution in the j^{th} line is linear, as shown in figure 3.1, so that

$$\theta_{c,j,i} = 2\bar{\theta}_{j,i}, \text{ for } j \neq i \quad (1)$$

From the measured contact point temperature rise, the heat flow from each thermometer line into the nanostructured sample can be expressed from the thermal resistance circuit figure 3.2 according to

$$Q_{j,i} = -\theta_{c,j,i}/R_{b,j}, \text{ for } j \neq i \quad (2a)$$

$$Q_{i,i} = -\sum_{j,j \neq i} Q_{j,i} \quad (2b)$$

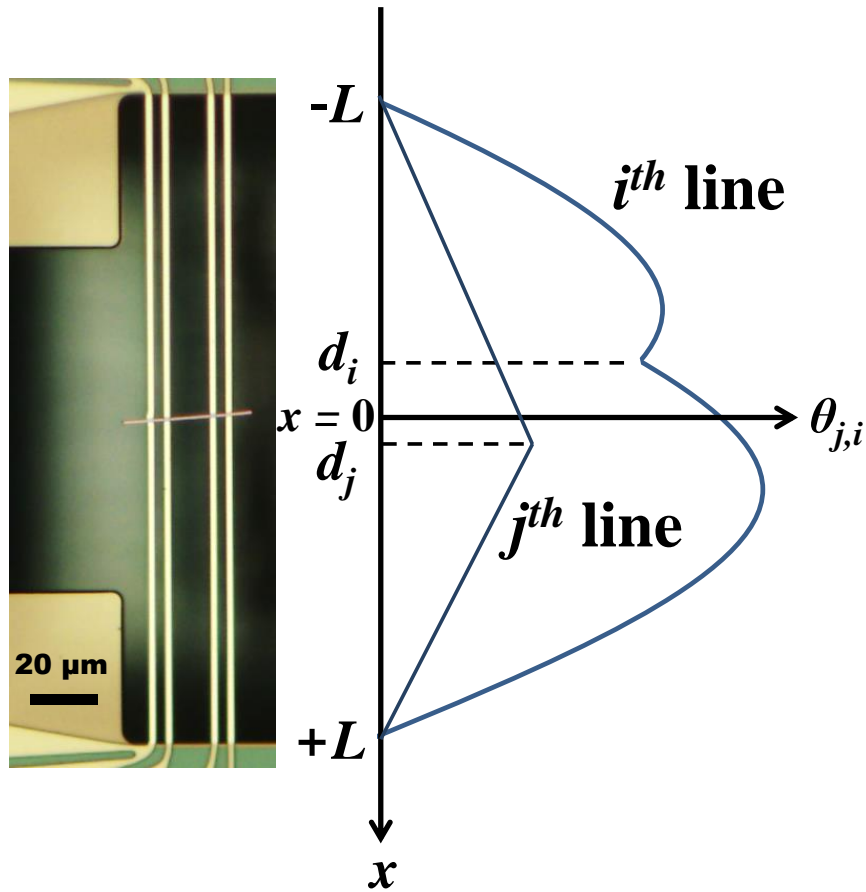


Figure 3.1: Optical micrograph of a device for four-probe thermal measurement with a Si nanowire sample assembled across all four suspended Pt/SiN_x RTs. The temperature profile of the *i*th heater line shows a parabolic shape because of uniform Joule heating, and the other three *j*th lines show linear temperature profile.

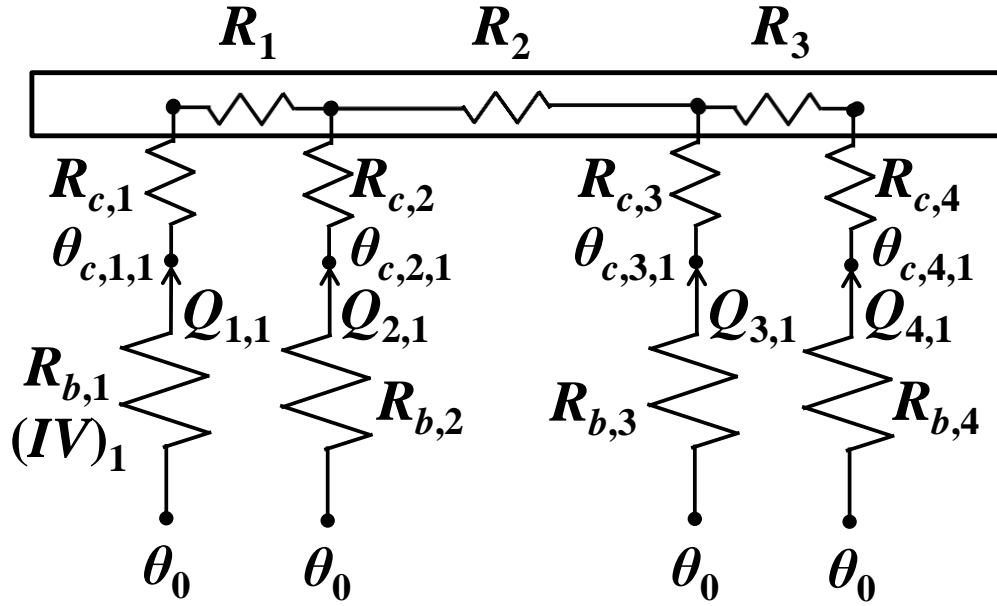


Figure 3.2: Thermal resistance circuit of the measurement device when RT1 is used as a heater at a rate of $(IV)_1$. R_1 , R_2 , and R_3 are the thermal resistances of the left, middle, and right suspended segments of the suspended Si nanowire sample. $R_{c,j}$ is the contact thermal resistance between the j^{th} Pt/SiN_x line and the sample. $R_{b,j}$ is the thermal resistance of the j^{th} Pt/SiN_x resistance thermometer line. $\theta_{c,j,i}$ is the j^{th} Pt/SiN_x line temperature at the contact to the sample when the i^{th} line is used as the heater line. The temperature rise θ_0 at the two ends of each of the suspended Pt/SiN_x lines is assumed to be negligible because the spreading thermal resistance of the Si substrate is orders of magnitude lower than $R_{b,j}$.

The thermal resistance of each suspended resistance thermometer line is given as

$$R_{b,j} = \frac{L_j}{2\kappa_j A_j} \left[1 - \left(\frac{d_j}{L_j} \right)^2 \right], \quad (3)$$

Here, κ_j , A_j , and $2L_j$ are the effective thermal conductivity, cross-sectional area, and length of the j^{th} suspended thermometer line, and d_j is the deviation of the center of the j^{th} line from its point of contact to the nanostructure sample, as shown in figure 3.1.

The temperature distribution in the i^{th} line with Joule heating shows a parabolic profile as illustrated in figure 3.1. A solution of this temperature distribution as a function of distance (x) from the center can be obtained by solving the heat diffusion equation with appropriate boundary conditions. The obtained solution is

$$\theta_{i,i}(x) = \frac{(IV)_i}{4\kappa_i A_i L_i} (L_i^2 - x^2) + \frac{[d_i + (-1)^{H(d_i-x)L_i}]}{2\kappa_i A_i L_i} [x - (-1)^{H(d_i-x)L_i}] Q_{i,i} \quad (4)$$

Here, the Heaviside step function $H(\chi)$ takes the value of 0 and 1 for $\chi < 0$ and $\chi \geq 0$, respectively. This temperature distribution can be used to calculate the average temperature rise of the i^{th} line as

$$\bar{\theta}_{i,i} = \frac{1}{2L_i} \int_{-L_i}^{L_i} \theta_{i,i}(x) dx \quad (5)$$

After carrying out the integration, the relationship between the average temperature rise $\bar{\theta}_{j,i}$ and the thermal resistances $R_{b,j}$ of suspended thermometer lines can be obtained as

$$\sum_{j=1}^4 \frac{\bar{\theta}_{j,i}/(IV)_i}{R_{b,j}} = \frac{1}{3[1-(d_i/L_i)^2]}, \text{ for } i = 1, 2, 3, \text{ and } 4 \quad (6)$$

Equation (6) yields four equations for $i=1, 2, 3, 4$ with four unknown values of the thermal resistances $R_{b,1}$, $R_{b,2}$, $R_{b,3}$, and $R_{b,4}$ of each suspended thermometer line. These four equations can be written in a matrix form, where the sixteen $\bar{\theta}_{j,i}/(IV)_i$ measurement values are the elements of a 4 x 4 matrix. This matrix can be inverted to obtain the thermal resistances $R_{b,1}$, $R_{b,2}$, $R_{b,3}$, and $R_{b,4}$. With the four obtained $R_{b,j}$ values, the contact point temperature rise of the heater line can now be calculated as

$$\theta_{c,i,i} \equiv \theta_{i,i}(x = d_i) = R_{b,i} \left[\frac{(IV)_i}{2} - 2 \left(\sum_{j=1}^4 \frac{\bar{\theta}_{j,i}}{R_{b,j}} - \frac{\bar{\theta}_{i,i}}{R_{b,i}} \right) \right] \quad (7)$$

From the Equations (1), (2), and (7), we can obtain sixteen pairs of $\theta_{c,j,i}/(IV)_i$ and $Q_{j,i}/(IV)_i$ data, with both i and j ranging from 1 to 4. These sixteen pairs of measurement values can be used to determine five thermal resistances in the thermal circuit of figure 3.2, where R_1 , R_2 , and R_3 are the intrinsic thermal resistances of the left, middle, and right suspended segments of the nanostructured sample, and $R_{c,1}$, $R_{c,2}$, $R_{c,3}$, and $R_{c,4}$ are the contact thermal resistances at the four contacts between the sample and the thermometer lines. Based on the thermal resistance circuit in figure 3.2, the temperature difference between the contacts of two middle thermometers can be expressed as

$$\theta_{c,2,i} - \theta_{c,3,i} = Q_{2,i}R_{c,2} + (Q_{1,i} + Q_{2,i})R_2 - Q_{3,i}R_{c,3}, \text{ for } i = 1,2,3,4 \quad (8)$$

The three unknown values of the thermal resistances R_2 , $R_{c,2}$, and $R_{c,3}$ can be determined from these four equations.

In addition, the temperature difference between the contact points of the two left thermometers can be expressed as

$$\theta_{c,1,i} - \theta_{c,2,i} = Q_{1,i}(R_1 + R_{c,1}) - Q_{2,i}R_{c,2} \quad , \text{ for } i = 1, 2, 3, 4, \quad (9)$$

while that between two right thermometers can be expressed

$$\theta_{c,4,i} - \theta_{c,3,i} = Q_{4,i}(R_3 + R_{c,4}) - Q_{3,i}R_{c,3} \quad , \text{ for } i = 1, 2, 3, 4 \quad (10)$$

With the already obtained values of $R_{c,2}$ and $R_{c,3}$ from the Equation (8), $(R_1 + R_{c,1})$ and $(R_3 + R_{c,4})$ can be determined by Equation (9) and (10), respectively.

Hence, the measurement of sixteen average temperature values $\bar{\theta}_{j,i}/(IV)_i$ can be used to determine the nine thermal resistances shown in the thermal circuit of figure 3.2, including $R_{b,1}$, $R_{b,2}$, $R_{b,3}$, $R_{b,4}$, $R_{c,2}$, R_2 , $R_{c,3}$, $R_1 + R_{c,1}$, and $R_3 + R_{c,4}$. The contact thermal resistances at the end contacts ($R_{c,1}$ and $R_{c,4}$) cannot be separated from the sum with the thermal resistance of the adjacent suspended sample segment ($R_1 + R_{c,1}$ and $R_3 + R_{c,4}$) because the heat flow rates through each end contact and the adjacent sample segment are always same. In comparison, the heat flow rates through the two middle contacts ($R_{c,2}$ and $R_{c,3}$) and the middle sample segment (R_2) are different, and depend on which Pt/SiN_x line is used as the heater line. This characteristic of the system can be used to separate the contact thermal resistances ($R_{c,2}$ and $R_{c,3}$) and the intrinsic thermal resistance (R_2) of the middle suspended segment of the nanostructured sample.

3.3 EXPERIMENTAL RESULTS

Two single crystalline silicon nanowire samples with different cross section areas of 240 nm x 220 nm and 740 nm x 220 nm were measured to demonstrate the effectiveness of the new four probe thermal measurement method. The cross section areas were intentionally chosen to be relatively large, so that the results obtained from the new measurement method can be compared with established theoretical models without the need to consider quantum confinement or anomalous surface scattering effects, which are not well explained yet. The measurement results were compared with two different theoretical models.

3.3.1 Device fabrication and sample preparation

Figure 3.3 shows the measurement devices assembled with two silicon nanowire samples of different cross section areas, which are 740 nm x 220 nm and 240 nm x 220 nm. The process of making the device consists of three parts, including fabrication of the suspended device, patterning of the silicon nanowires, and transferring of the nanowire onto the measurement device.

The fabrication of the suspended device is carried out with conventional semiconductor processing techniques such as photolithography, metal evaporation, reactive ion etching, and wet chemical etching. The length of each suspended thermometer line is 200 μm and the width is 2 μm for the devices shown in figure 3.3. These length and width can be adjusted depending on the measured nanostructure sample. When the thermometer line width is much smaller than the length of the middle suspended segment of the nanostructure sample and the length of the thermometer line is much longer than the width of the sample, the contact between the thermometer line and the sample can be approximated as a point contact, which is assumed in the previous analysis. For measuring a wider sample than the Si nanowire, such as a graphene flake,

the length of the four suspended thermometer lines can be designed to be much longer than the sample width, so that the contact can be approximated as a point contact.

The silicon nanowire sample is fabricated from a silicon-on-insulator (SOI) wafer with a 220 nm thick top silicon layer doped with $5 \times 10^{16} \text{ cm}^{-3}$ boron and 3 μm thick buried SiO_2 layer. The nanowire is first patterned by electron beam lithography and reactive ion etching of the top Si to obtain the width of 740 nm and 240 nm. The nanowires are suspended by wet etching the buried SiO_2 layer with diluted hydrogen fluoride acid. Figure 3.4 shows the obtained suspended silicon nanowires.

Once the suspended device and the nanowire sample are made, the nanowire can be transferred with a polymethyl methacrylate (PMMA) carrier layer on a device. Figure 3.4 shows the process of transferring and aligning a nanowire sample on a prefabricated suspended device. The patterned and suspended nanowire sample is picked up with a sharp tungsten probe, and transferred to a piece of wafer coated with polyvinyl alcohol, (PVA), which is water soluble. A PMMA layer is spin coated on this piece of wafer, and the PVA layer is dissolved in deionized water, resulting in the separation of PMMA layer. The nanowire sample is still attached to the PMMA layer, so that we can manipulate the large PMMA layer and align the attached nanowire sample on the measurement device. After aligning the silicon nanowire sample, the PMMA layer is removed by heating to a temperature of 350°C in a low-pressure tube furnace with argon and hydrogen flow.

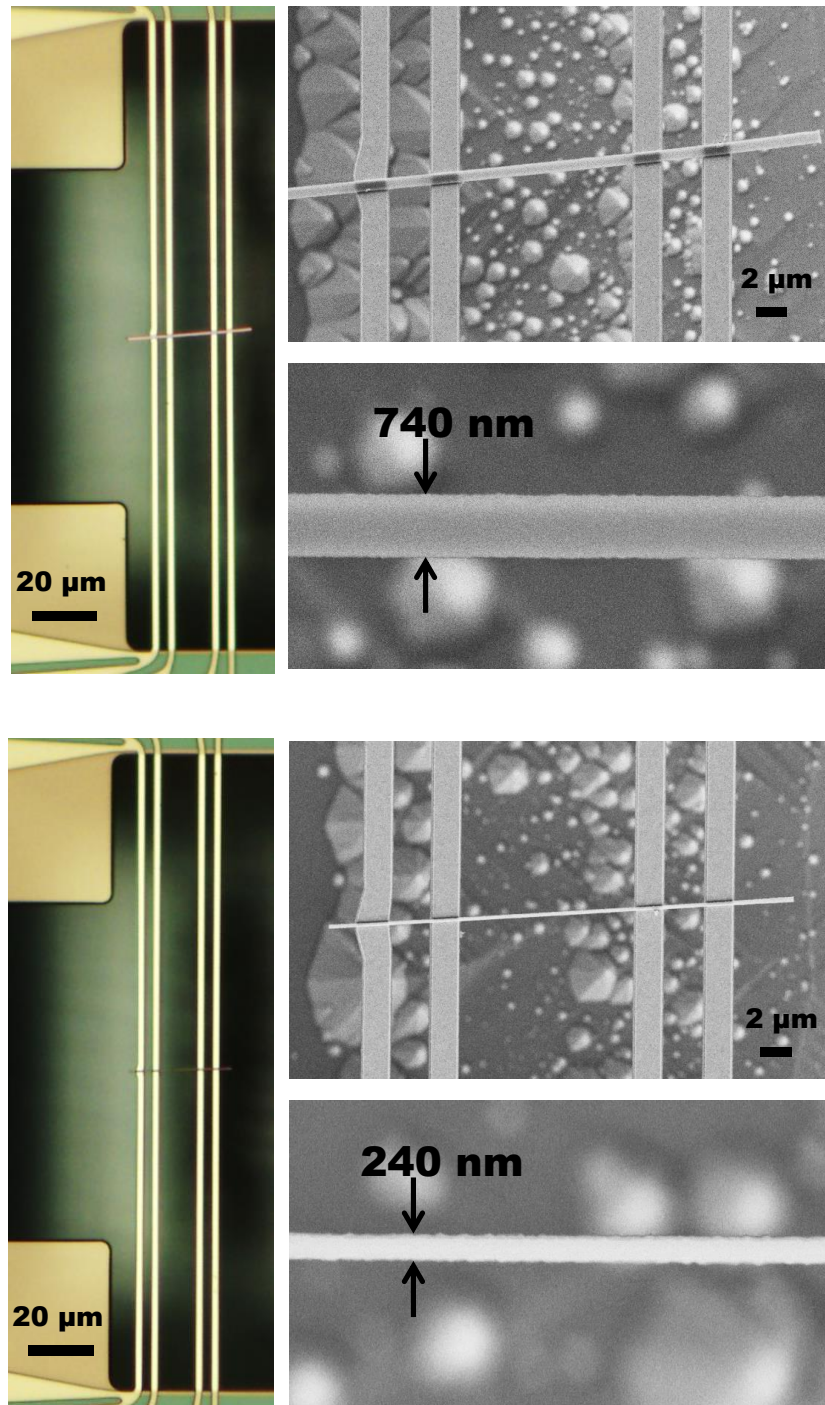


Figure 3.3: Completed devices assembled with silicon nanowire samples of two different cross section areas: $740\ \text{nm} \times 220\ \text{nm}$ and $240\ \text{nm} \times 220\ \text{nm}$.

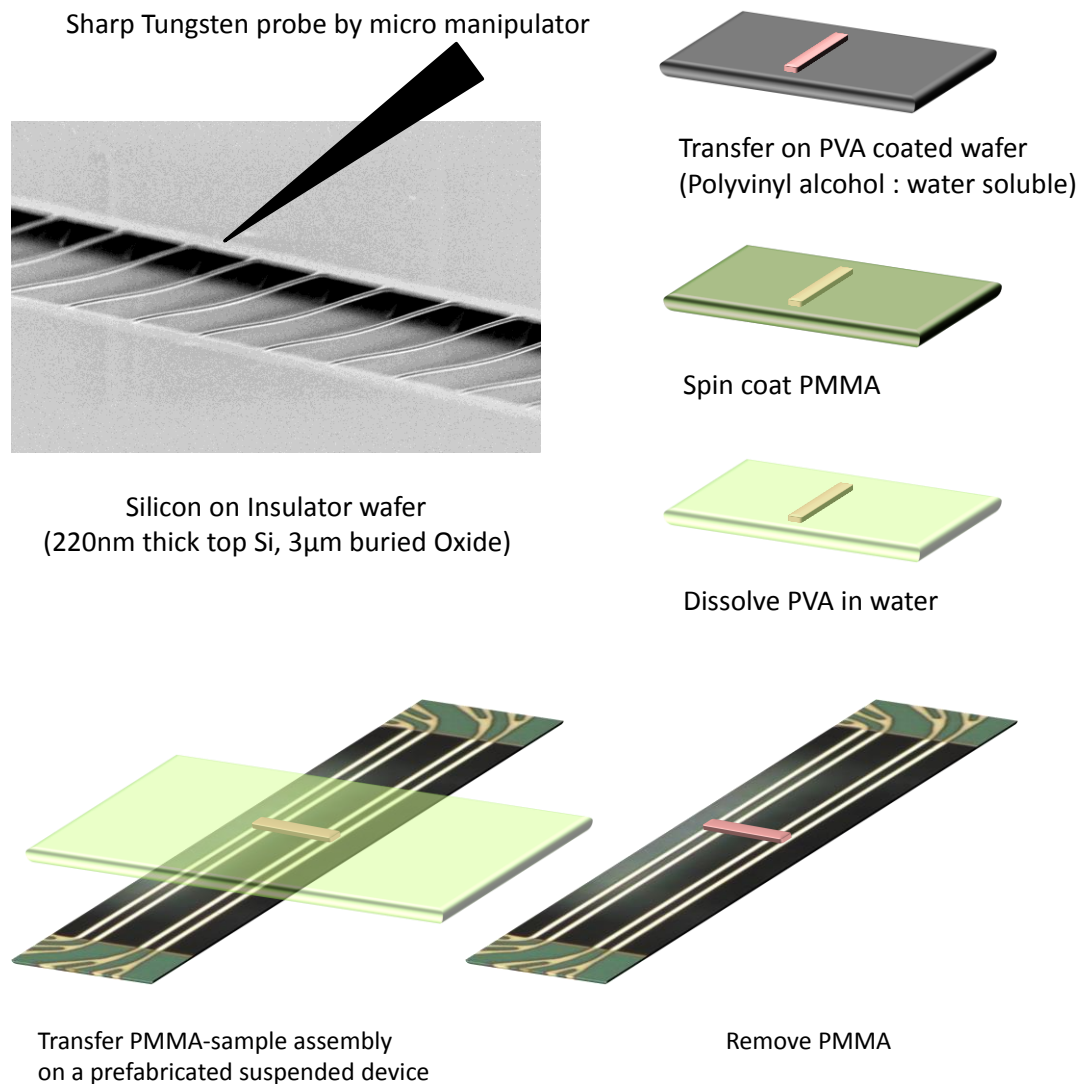


Figure 3.4: Process of transferring silicon nanowire sample on a pre-fabricated device with four suspended thermometer lines. The nanowire is first transferred on a piece of wafer with polyvinyl alcohol (PVA) coating, and polymethyl methacrylate (PMMA) is spin coated on the piece. The PVA layer is dissolved in water, and the PMMA layer with the nanowire sample is floating on water. The PMMA layer is transferred and aligned on a suspended device, and the PMMA layer is removed finally.

3.3.2 Measurement setup

After wire bonding the completed device on a chip carrier, it is measured in a high vacuum cryostat with environment temperature control. When one of the suspended thermometer line (i^{th} line) is heated by direct current I ramped between $-350 \mu\text{A}$ and $+350 \mu\text{A}$, voltage drop is measured between both ends of the line to calculate the electrical resistance ($R_{e,i}$) of the i^{th} heating line. The other three thermometer lines are connected to lock-in amplifiers, and the electrical four probe resistance ($R_{e,j}$) of each line is measured by flowing a $1 \mu\text{A}$ sinusoidal excitation current. The sinusoidal sensing current is about 350 times smaller than the maximum direct heating current applied to the heating line, so the corresponding Joule heating rate is five orders of magnitude smaller. Moreover, the sinusoidal sensing current is constant, and does not affect the measured temperature rise ($\theta_{j,i}$) of a thermometer line caused by the heating current, and only shifts the absolute temperature. Consequently, the theoretical results of $\theta_{j,i}$ distributions are not affected by the small sinusoidal sensing current.

The silicon nanowire samples measured in this work did not make electrical contact to the thermometer lines because of the amorphous native oxide on the Si nanowire, so that all the resistance of the thermometer lines can be measured simultaneously. If the sample made electrical contact to the thermometer lines, it could still be measured by connecting a floating current source to the heater line. The electrical resistance of the other three lines could be measured with a lock-in amplifier one at a time at the same heating current to prevent electrical current flowing through the sample.

3.3.3 Measurement results

Figure 3.5 (a) shows a set of measurement data of the electrical resistance rise $\Delta R_{e,j} = R_{e,j}(I) - R_{e,j}(I = 0)$ when the direct heating current is applied to the first line ($i=1$).

To convert this electrical resistance rise to the average temperature rise ($\bar{\theta}_{j,i}$), the temperature coefficient of resistance (TCR) of each thermometer line needs to be measured. The electrical resistance of each line at zero heating current, $R_{e,j}(I = 0)$, was measured with the sample stage temperature (T_0) varied from 100 K to 400 K. Figure 3.5 (b) shows the linear temperature dependence of the electrical resistance of each thermometer line as a function of stage temperature. The linear slope can be used to obtain the TCR for each line.

The obtained average temperature rise ($\bar{\theta}_{j,i}$) of each thermometer line can be plotted as a function of the electrical heating rate $(IV)_i$ in the i^{th} heater line as shown in figure 3.6 (a). The slope $\bar{\theta}_{j,i}/(IV)_i$ is used to determine the thermal resistance of each thermometer line $R_{b,1}$, $R_{b,2}$, $R_{b,3}$, and $R_{b,4}$ with equation (6). The results are shown in figure 3.7. The four suspended thermometer lines are designed to have the same dimension, so that the measured thermal resistances are almost the same. After these thermal resistances are obtained, the sixteen pairs of $\theta_{c,j,i}/(IV)_i$ and $Q_{j,i}/(IV)_i$ can be determined according to equations (1), (2), and (7). Figure 3.6 (b) shows the obtained $Q_{j,1}$ as a function of the heating current in the first line, and figure 3.8 shows the linear slope of $\theta_{c,j,1}/(IV)_1$ and $Q_{j,1}/(IV)_1$ at 350K.

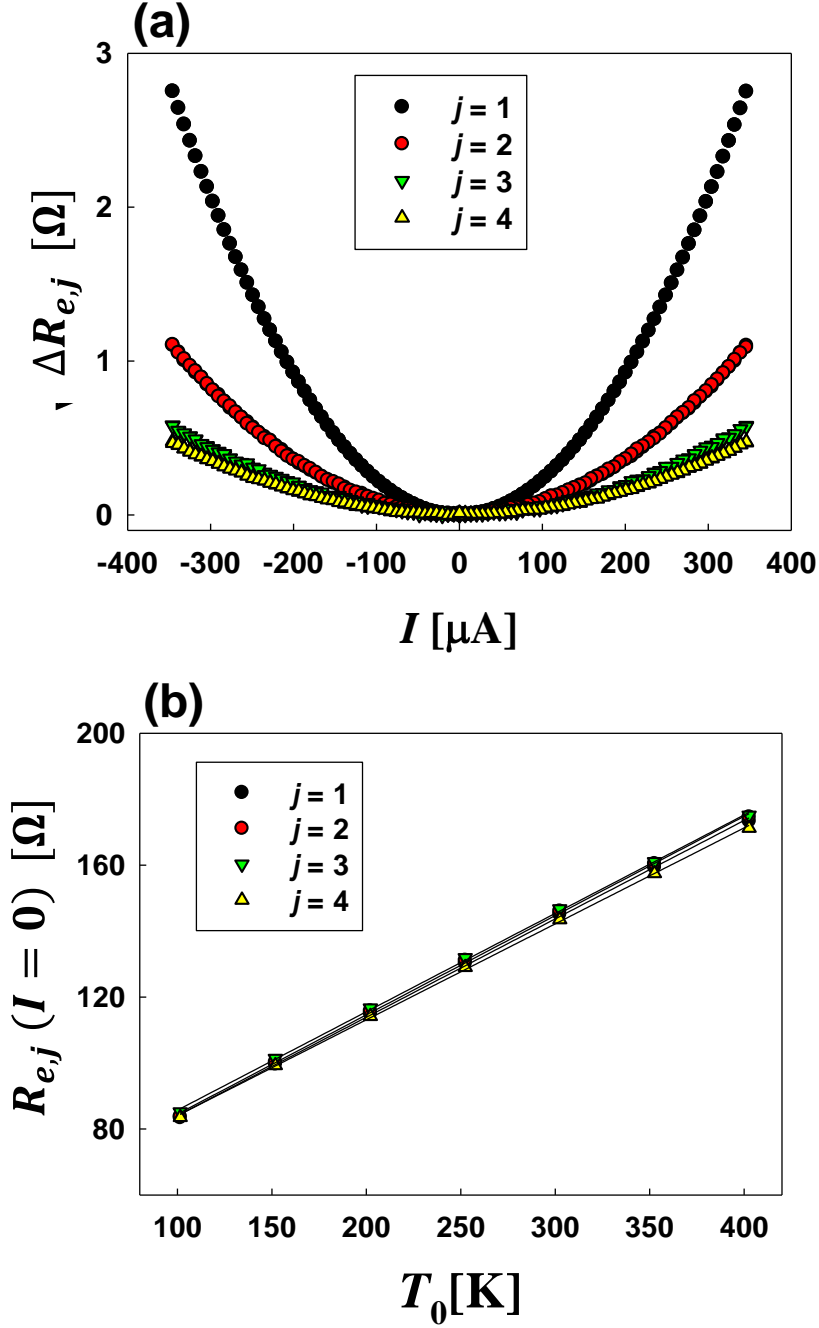


Figure 3.5: (a) Measured electrical resistance rises of RT1, RT2, RT3, and RT4 as a function of the heating current in RT1 at sample stage temperature $T_0 = 350\text{K}$. (b) Measured $R_e(I = 0)$ at different sample stage temperature (T_0). The temperature coefficient of resistance (TCR) can be obtained from the linear fit of each set of the measurement data.

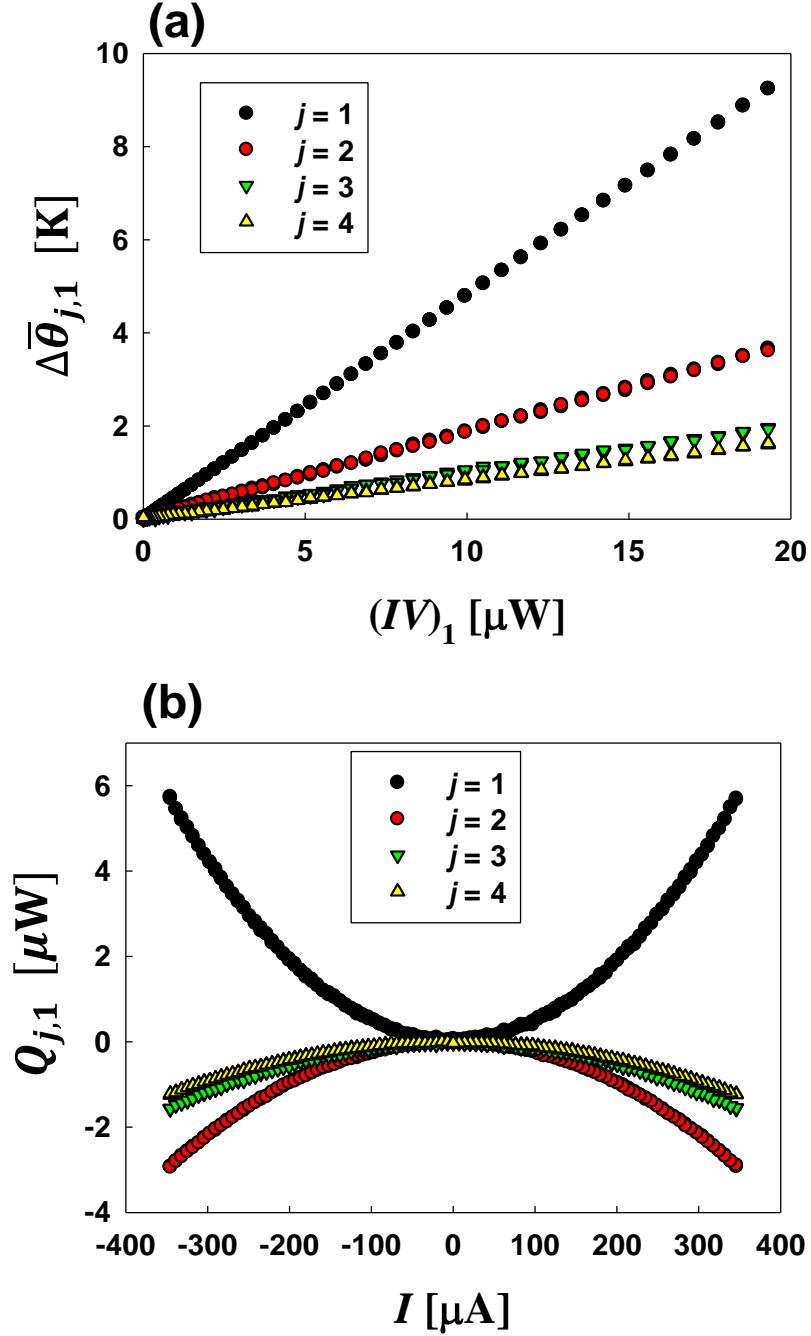


Figure 3.6: (a) Measured average temperature rise of each RT as a function of Joule heating rate in the first line when $T_0 = 350$ K. (b) Net heat flow rate across the contact point from each thermometer line into the nanowire sample as a function of the heating current (I) in the first line.

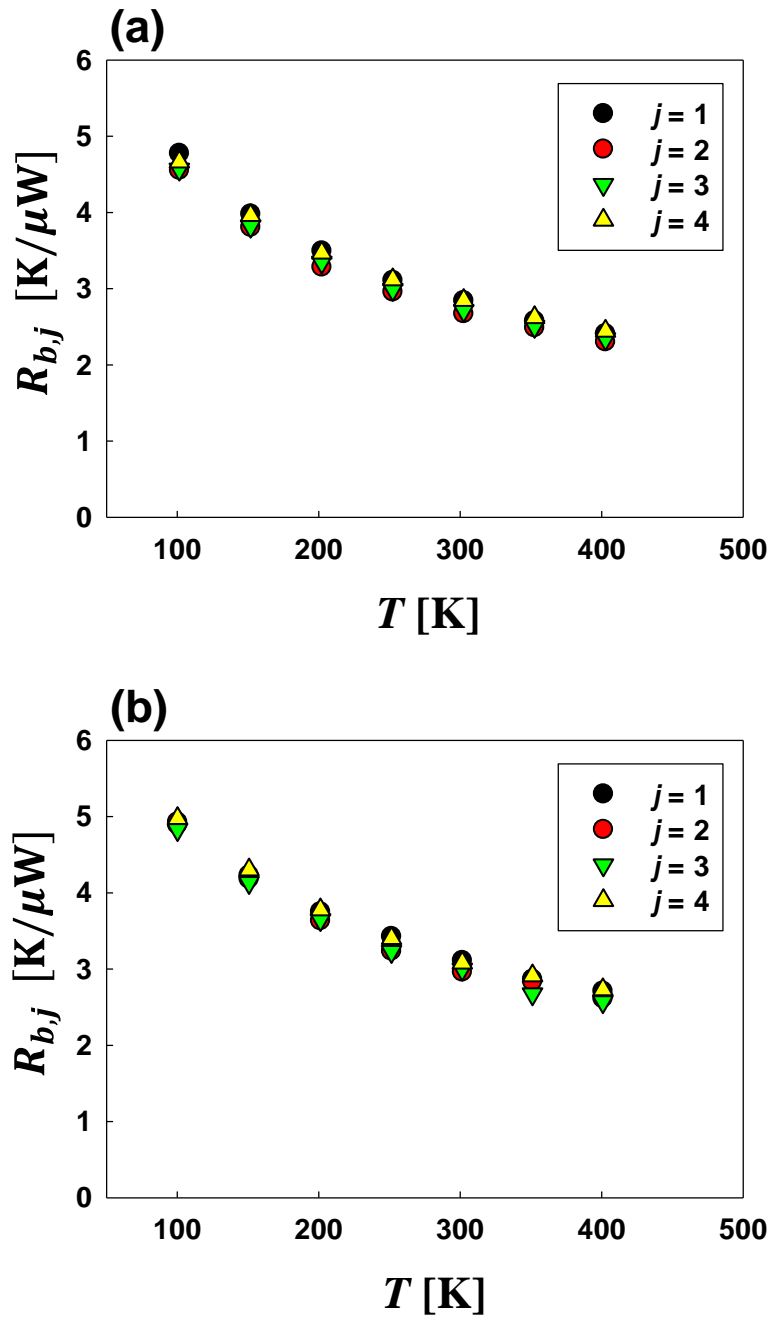


Figure 3.7: Measured thermal resistances of four suspended thermometers as a function of stage temperature T_0 for 740 nm width sample (a) and 240 nm sample (b). The designs of both devices are the same, so that the values are almost same between the two samples.

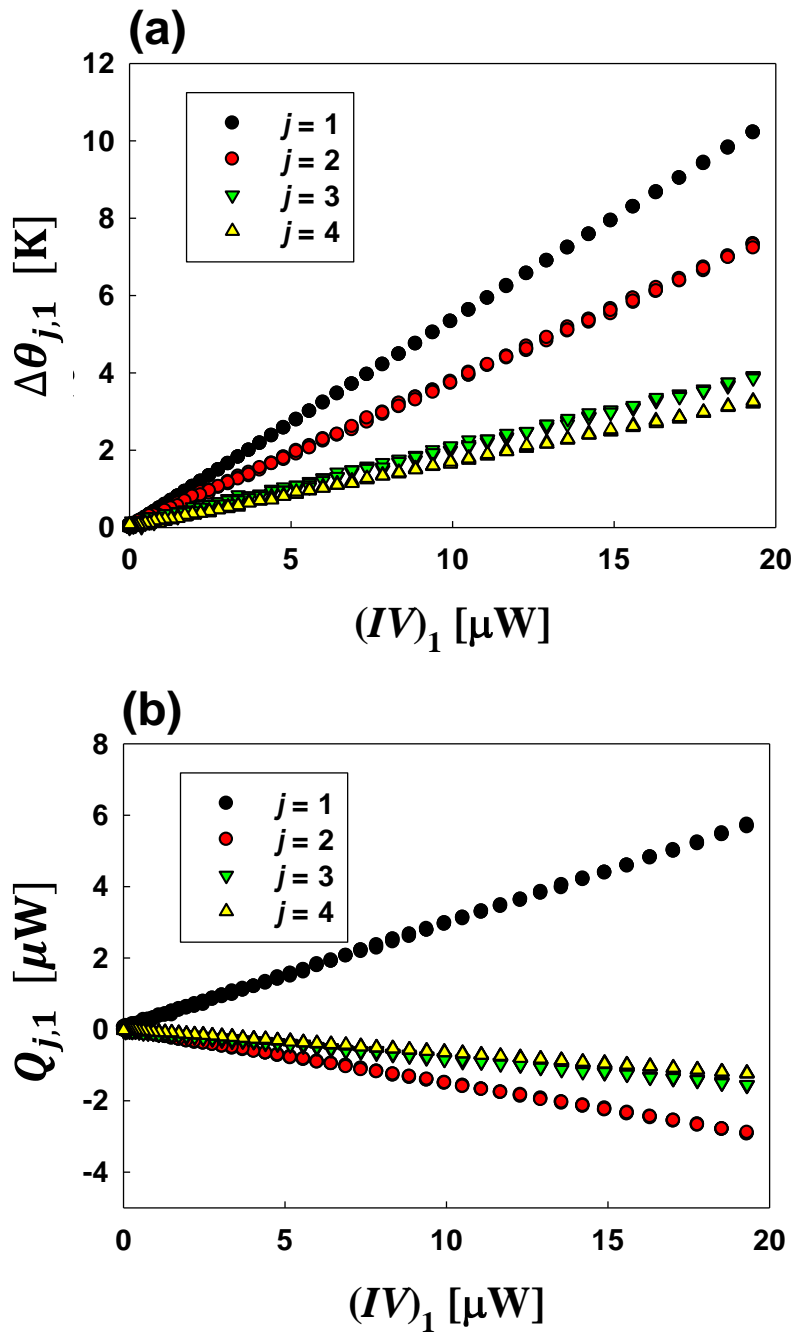


Figure 3.8: (a) Measured contact point temperature rise of each RT as a function of the Joule heating rate in the first line when $T_0 = 350\text{K}$. (b) Net heat flow rate across the contact point from each thermometer line into the nanowire sample as a function of Joule heating rate in the first line.

The sixteen pairs of $\theta_{c,j,i}/(IV)_i$ and $Q_{j,i}/(IV)_i$ data are then used to determine thermal resistances of $R_{c,2}$, R_2 , $R_{c,3}$, $R_1+R_{c,1}$, and $R_3+R_{c,4}$ according to equations 8, 9, and 10. First, $R_{c,2}$, R_2 , and $R_{c,3}$ are determined with three of four equations expressed in equation (8) for $i=1, 2, 3$, and 4. Here, there are four different combinations of three equations out of the four equations. These four combinations can yield four sets of $R_{c,2}$, R_2 , and $R_{c,3}$ values. Under perfect measurement conditions, these four values of $R_{c,2}$, R_2 , and $R_{c,3}$ will be exactly the same. However, the presence of errors in the actual measurements can produce variations in these thermal resistances. These variations can be used to show the measurement uncertainty. After the thermal resistances of $R_{c,2}$, R_2 , and $R_{c,3}$ are obtained, the other thermal resistances of $R_1+R_{c,1}$ and $R_3+R_{c,4}$ can be obtained from equations (9) and (10), respectively. They can also have four different values from the set of four equations expressed by equations (9) and (10) for $i=1, 2, 3$, and 4. We have calculated the average of the four values obtained for each of the five thermal resistances of $R_{c,2}$, R_2 , $R_{c,3}$, $R_1+R_{c,1}$, and $R_3+R_{c,4}$, and plotted them in figure 3.9. The range of variations of the four obtained thermal resistance values are used as error bars in the figure, which shows rather small variation of the four values.

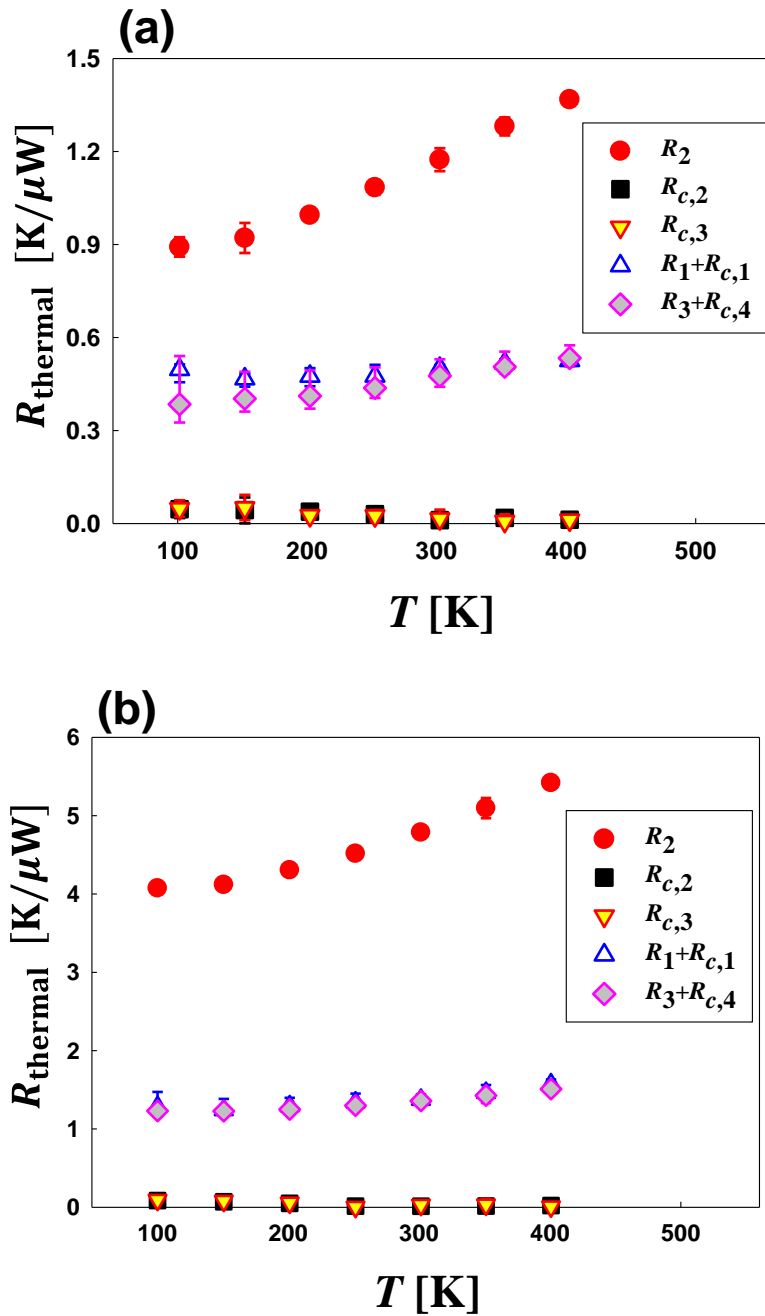


Figure 3.9: The five measured thermal resistances, including the intrinsic thermal resistance of the middle suspended segment of the sample (R_2), and contact thermal resistances of the two middle contacts ($R_{c,2}$ and $R_{c,3}$), for the two Si nanowire samples with the cross section being 740 nm x 220 nm (a) and 240 nm x 220 nm (b).

As shown in figure 3.9, the two contact thermal resistances of $R_{c,2}$ and $R_{c,3}$ are much smaller than the intrinsic thermal resistance R_2 of the middle suspended segment of the sample for the two Si nanowire samples. The contact thermal resistances measured at 300 K were normalized with the apparent contact areas to obtain the interface thermal conductance in the range between 38×10^6 and $230 \times 10^6 \text{ W m}^{-2} \text{ K}^{-1}$. These values are comparable to the measurement results by time domain thermal reflectance (TDTR) measurement method between sputtered Au and Au(Pd) alloy on SiO_2 .²⁹ During the process of transferring the silicon nanowire, the sample is annealed at the temperature of 350°C to remove the PMMA transfer layer. This high temperature annealing process could have improved the thermal contacts. In addition, the measured contact thermal resistances of $R_{c,2}$ and $R_{c,3}$ increases slightly as the temperature decreased from 400K to 100K. This tendency is consistent with the dependence of interface thermal conductance on the specific heat, which decreases with decreasing temperature.³⁰

The resolution and the noise level of the measurement method are mainly limited by the 10 - 50 mK temperature fluctuation of the cryostat sample stage as reported for serpentine Pt resistance thermometer devices.⁵ For a maximum temperature rise in the heater line of less than 5K, the maximum value of the sample and contact thermal resistances measurable with the current measurement device would be about one hundred times of the thermometer thermal resistance (R_b) or $300 \text{ K}/\mu\text{W}$. Similarly, the minimum value would be about one hundredth of R_b or $0.03 \text{ K}/\mu\text{W}$, according to the analysis similar to the earlier work.⁵ In comparison, a $3 \mu\text{m}$ wide and $5 \mu\text{m}$ long single layer graphene with a high thermal conductivity of about $2500 \text{ W m}^{-1} \text{ K}^{-1}$ would have the thermal resistance of $2 \text{ K}/\mu\text{W}$, so that such sample should be measurable with the current device. In comparison, a 10 nm diameter and $5 \mu\text{m}$ long nanowire sample with a low thermal conductivity of $1 \text{ W m}^{-1} \text{ K}^{-1}$ would have the thermal resistance of $6 \times 10^4 \text{ K}/\mu\text{W}$,

so that this sample cannot be measured with the current device design. However, the dimension of the device can be modified to increase R_b to approach the level of the sample thermal resistance. In addition, a differential method can be used to considerably reduce the impact of the cryostat stage temperature fluctuation, as reported in recent studies.^{31, 32} With these additional efforts, the maximum value of thermal resistance measurable with this method can be on the order of 1×10^4 K/ μ W, which is comparable to those achievable with the serpentine Pt resistance thermometer devices.^{31, 32} Similarly, the minimum value can approach the order of 1×10^{-3} K/ μ W by decreasing R_b .

Thermal conductivity of the silicon nanowire samples were calculated from the measured intrinsic thermal resistance R_2 and the measured dimensions of the two samples. The result is shown in figure 3.10. The experimental measurement values are compared to two theoretical calculation models, one by Morelli *et al.*,³³ and the other by Wang *et al.*,³⁴ from which we calculated the thermal conductivity of bulk silicon and nanowires. In the calculation, the equivalent boundary scattering mean free path is taken as $l_b = 2(wt/\pi)^{1/2}$, which is combined with phonon-phonon and phonon-isotope scattering to obtain the total scattering mean free path via the Matthiessen's rule.³⁵

$$\tau^{-1} = \tau_{anharmonic}^{-1} + \tau_{boundary}^{-1}$$

$$\kappa = \frac{k_B^4 T^3}{2\pi^2 v_b \hbar^3} \int_0^{\hbar\omega_c/k_B T} \tau(T, y) y^4 \frac{e^y}{(e^y - 1)^2} dy$$

This calculation has not accounted for phonon scattering by impurity dopants and other point defects because the impurity doping of the SOI wafer is very low, and it is unclear whether additional point defects could have been generated by the reactive ion etching

process during the patterning of Si nanowire sample similar to that found in an earlier study on Si etching.³⁶ As shown in figure 3.10, the thermal conductivity values obtained by the four probe measurement method lie between two calculation models for both nanowire samples, and are close to the results calculated with the model of Wang *et al.*,³⁴ where the upper phonon frequency limit was adjusted according to a previous measurement result of a Si nanowire. The thermal conductivity values measured by the four probe method are free of contact thermal resistance error, and could be used for further calibration of these theoretical calculation models.

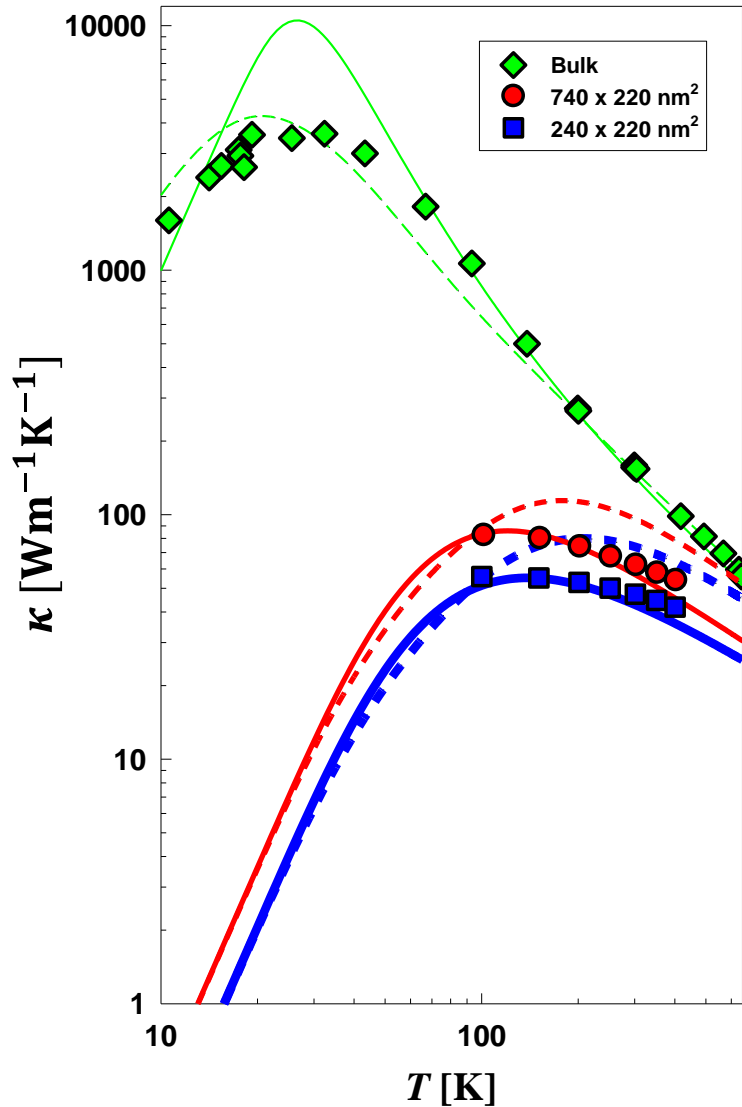


Figure 3.10: Measured thermal conductivity of the 740 nm wide (circles) and the 240 nm wide (squares) Si nanowire samples, both with 220 nm thickness. For comparison, the measured thermal conductivity data of bulk Si crystals (diamonds) reported by Glassbrenner and Slack,³⁷ and two different theoretical calculation results for bulk Si and Si nanowires with the same equivalent diameter as the two samples measured here. The theoretical calculations are based on the models reported by Morelli, Heremans, and Slack³³ (dashed lines) and Wang and Mingo³⁴ (solid lines). Thin green, red, and thick blue lines and symbols are used for the results for bulk, $740 \times 220 \text{ nm}^2$, and $240 \times 220 \text{ nm}^2$ cross section. The uncertainty of some data points is smaller than the symbol size.

3.4 SUMMARY

A novel four probe thermal transport measurement method for nanostructures has been developed in this work. This method is demonstrated by measurements of two silicon nanowire samples with different cross section areas. The results show that the method is highly effective for measuring the intrinsic thermal transport properties of nanostructures. In particular, the intrinsic thermal resistance of the nanostructure sample can be determined independently together with the contact thermal resistances of the contacts between the sample and the measurement device. Moreover, the design of the device is relatively simple, as it consists of only four suspended thermometer lines, which can be readily fabricated with the conventional photolithography and etching processes. In addition, a nanostructure sample can be transferred with a high yield with the use of a PMMA carrier layer. Hence, the four probe thermal measurement method for nanostructures can potentially become an important method to enable accurate determination of unique size dependent thermal transport phenomena, and to provide reliable experimental data for refinement of theoretical models.

REFERENCES

1. L. Lindsay, D. A. Broido and N. Mingo, *Physical Review B* 82 (16), 161402 (2010).
2. N. Mingo and D. A. Broido, *Nano Letters* 5 (7), 1221-1225 (2005).
3. K. Schwab, E. A. Henriksen, J. M. Worlock and M. L. Roukes, *Nature* 404 (6781), 974-977 (2000).
4. P. Kim, L. Shi, A. Majumdar and P. L. McEuen, *Physical Review Letters* 87 (21), 215502 (2001).
5. L. Shi, D. Li, C. Yu, W. Jang, D. Kim, Z. Yao, P. Kim and A. Majumdar, *Journal of Heat Transfer* 125 (5), 881-888 (2003).
6. D. Li, Y. Wu, P. Kim, L. Shi, P. Yang and A. Majumdar, *Applied Physics Letters* 83 (14), 2934-2936 (2003).
7. C. Yu, L. Shi, Z. Yao, D. Li and A. Majumdar, *Nano Letters* 5 (9), 1842-1846 (2005).
8. E. Pop, D. Mann, Q. Wang, K. Goodson and H. Dai, *Nano Letters* 6 (1), 96-100 (2006).
9. I.-K. Hsu, R. Kumar, A. Bushmaker, S. B. Cronin, M. T. Pettes, L. Shi, T. Brintlinger, M. S. Fuhrer and J. Cumings, *Applied Physics Letters* 92 (6), 063119 (2008).
10. A. A. Balandin, S. Ghosh, W. Bao, I. Calizo, D. Teweldebrhan, F. Miao and C. N. Lau, *Nano Letters* 8 (3), 902-907 (2008).
11. A. Mavrokefalos, M. T. Pettes, F. Zhou and L. Shi, *Review of Scientific Instruments* 78 (3), 034901 (2007).
12. A. I. Persson, Y. K. Koh, D. G. Cahill, L. Samuelson and H. Linke, *Nano Letters* 9 (12), 4484-4488 (2009).
13. J. H. Seol, I. Jo, A. L. Moore, L. Lindsay, Z. H. Aitken, M. T. Pettes, X. Li, Z. Yao, R. Huang, D. Broido, N. Mingo, R. S. Ruoff and L. Shi, *Science* 328 (5975), 213-216 (2010).
14. W. Jang, Z. Chen, W. Bao, C. N. Lau and C. Dames, *Nano Letters* 10 (10), 3909-3913 (2010).
15. C. Faugeras, B. Faugeras, M. Orlita, M. Potemski, R. R. Nair and A. K. Geim, *ACS Nano* 4 (4), 1889-1892 (2010).
16. W. Cai, A. L. Moore, Y. Zhu, X. Li, S. Chen, L. Shi and R. S. Ruoff, *Nano Letters* 10 (5), 1645-1651 (2010).

17. *S. Shen, A. Henry, J. Tong, R. Zheng and G. Chen, Nat Nano 5 (4), 251-255 (2010).*
18. *Z. Wang, R. Xie, C. T. Bui, D. Liu, X. Ni, B. Li and J. T. L. Thong, Nano Letters 11 (1), 113-118 (2011).*
19. *M. T. Pettes, I. Jo, Z. Yao and L. Shi, Nano Letters 11 (3), 1195-1200 (2011).*
20. *I. Jo, M. T. Pettes, J. Kim, K. Watanabe, T. Taniguchi, Z. Yao and L. Shi, Nano Letters 13 (2), 550-554 (2013).*
21. *C. Canetta, S. Guo and A. Narayanaswamy, Review of Scientific Instruments 85 (10), 104901 (2014).*
22. *A. Weathers and L. Shi, Annual Review of Heat Transfer 16, 101-134 (2013).*
23. *L. Shi, Applied Physics Letters 92 (20), 206103 (2008).*
24. *M. T. Pettes and L. Shi, Advanced Functional Materials 19 (24), 3918-3925 (2009).*
25. *L. Shi, Nanoscale and Microscale Thermophysical Engineering 16 (2), 79-116 (2012).*
26. *D. Liu, R. Xie, N. Yang, B. Li and J. T. L. Thong, Nano Letters 14 (2), 806-812 (2014).*
27. *M. M. Sadeghi, I. Jo and L. Shi, Proceedings of the National Academy of Sciences 110 (41), 16321-16326 (2013).*
28. *J. H. Seol, A. L. Moore, L. Shi, I. Jo and Z. Yao, Journal of Heat Transfer 133 (2), 022403-022403 (2010).*
29. *D.-W. Oh, S. Kim, J. A. Rogers, D. G. Cahill and S. Sinha, Advanced Materials 23 (43), 5028-5033 (2011).*
30. *E. T. Swartz and R. O. Pohl, Reviews of Modern Physics 61 (3), 605-668 (1989).*
31. *A. Weathers, K. Bi, M. T. Pettes and L. Shi, Review of Scientific Instruments 84 (8), 084903 (2013).*
32. *M. C. Wingert, Z. C. Y. Chen, S. Kwon, J. Xiang and R. Chen, Review of Scientific Instruments 83 (2), 024901 (2012).*
33. *D. T. Morelli, J. P. Heremans and G. A. Slack, Physical Review B 66 (19), 195304 (2002).*
34. *Z. Wang and N. Mingo, Applied Physics Letters 97 (10), 101903 (2010).*
35. *J. M. Ziman, Electrons and Phonons: The Theory of Transport Phenomena in Solids. (OUP Oxford, 1960).*
36. *G. S. Oehrlein, Materials Science and Engineering: B 4 (1-4), 441-450 (1989).*

37. *C. J. Glassbrenner and G. A. Slack, Physical Review 134 (4A), A1058-A1069 (1964).*

Chapter 4: Thermal and Thermoelectric Transport in Boron Arsenide Nanostructures

BAs is a III-V compound semiconductor with a cubic zinc blende structure and strong covalent bonding.^{1,2} This material has not been actively investigated for a long time. Recently, a theoretical calculation has suggested that BAs can possess ultrahigh thermal conductivity comparable to diamond at above room temperatures. However, there has been few experimental data on thermal transport properties of BAs. This chapter presents measurements of thermal and thermoelectric properties of boron arsenide (BAs) nanostructure samples. The four probe thermal transport measurement method³ described in chapter three of this dissertation is employed to measure the intrinsic thermal conductivity, and further developed to measure the Seebeck coefficient and electrical conductivity of individual BAs nanostructures, which are synthesized by a vapor transport method.

4.1 INTRODUCTION

As the miniaturization of electronic devices continues, the increased electrical power density per unit device area or volume makes device thermal management a critical challenge.⁴ For example, local hot spots can occur at the high and non-uniform power density. Such hot spots can decrease the device performance and reliability. Employing high thermal conductivity materials as a heat spreading layer or substrate is one possible approach to addressing the thermal management challenge. Therefore investigation of high thermal conductivity materials is an area of active research.⁵⁻¹² This field of research includes efforts on theoretical predictions of thermal conductivity of materials, and in experimental synthesis and characterization of materials with potentially high thermal conductivity. Among different materials, carbon based materials such as

diamond, graphite, graphene, and carbon nanotubes are characterized with record-high thermal conductivity. The reported room temperature thermal conductivity of bulk diamond is as high as about $2270 \text{ Wm}^{-1}\text{K}^{-1}$ and $3450 \text{ Wm}^{-1}\text{K}^{-1}$ for natural diamond and isotopically pure ^{12}C diamond, respectively.^{7, 13} Because of the high thermal conductivity of diamond crystals, there have been many efforts to synthesize diamond films on substrates of integrated electronic devices to reduce the operating temperature at a high power density. However, it remains a significant challenge to grow diamond films with a sufficiently high crystal quality and growth rate.

A recent first principles calculation has suggested that cubic boron arsenide (BAs) crystal can possess ultrahigh thermal conductivity.¹⁴ At above room temperature, the calculated thermal conductivity of BAs exceeds that of existing record value held by diamond. According to this theory, the large atomic mass contrast between B and As results in a large energy gap between the optical branches and acoustic branches in BAs, as well as the close bunching of different acoustic branches. The large frequency gap between acoustic and optical branches reduce the scattering between acoustic phonons and optical phonon, while the bunching of acoustic branches decrease scattering involving three acoustic phonons. The suppressed scattering of acoustic phonons results in the predicted ultrahigh thermal conductivity at above room temperatures. Furthermore, most of the short wave length acoustic phonons are governed by atomic motion of the heavy As atoms, which are isotopically pure, so that phonon-isotope impurity scattering is weak in BAs despite the high isotopic impurity concentration in naturally occurring B elements.

Although BAs is expected to have ultrahigh thermal conductivity, only one very recent paper has reported the experimental measurement of thermal conductivity of BAs particles with a dimension of a few hundreds of microns.¹⁵ The obtained thermal

conductivity at room temperature is only $200 \text{ W m}^{-1} \text{ K}^{-1}$, nearly one order of magnitude lower than the theoretical calculation result. This discrepancy is attributed to As deficiency in the BAs sample measured. One reason for the lack of experimental results on BAs lies in the challenge of synthesis in high-quality BAs crystals. As of now, only small crystals of BAs in the shape of micro particles, nanoplates, and nanorods, have been synthesized.^{2, 16} While measuring the thermal transport properties of these BAs nanostructures and microstructure is challenging, such measurements can provide useful data to verify the pronounced size-dependent thermal conductivity of BAs reported in the theoretical calculation. Such pronounced size dependence originates from the long bulk phonon mean free path, which can be reduced considerably by boundary scattering in BAs microstructures. Experimentally obtained size-dependent thermal conductivity can also be used to extract the phonon mean free path distribution in BAs, and provide a better understanding of the phonon transport behaviors. The following sections describe thermal and thermoelectric property measurements of BAs nanostructure samples, including sample preparation, measurement method, and results. The obtained thermal conductivity, Seebeck coefficient, and electrical resistivity of a BAs sample are discussed.

4.2 CRYSTAL GROWTH AND CHARACTERIZATION

The BAs crystals are grown by the vapor transport method by the Cowley group according to a method reported in their earlier publication.¹⁶ Figure 4.1 shows the BAs synthesis process. In this process, elemental boron pellets and arsenic powder are mixed in a 1:2.1 molar ratio in a quartz tube, which is evacuated for one hour by connecting to a Schlenk line. The tube is sealed with oxy-acetylene torch, and then the ampoules are

placed in a box furnace at 800 °C for 72 hours. The ampoules are cooled down to room temperature slowly at the rate of 0.1 °C/min, and the growth process is completed. During the growth process, the vaporized arsenic reacts on the surface of boron pellets and BAs crystals are produced. As shown in figure 4.2, the boron pellets are covered by various shapes of BAs crystals after the growth. Besides polycrystalline film coated on the boron substrate, individual single crystalline structures such as nanorods, dendrites, plates, and nanowires can be obtained from the growth.

Boron pellets before and after the BAs growth process are crushed and examined with powder X-ray diffraction (XRD). The two XRD results are compared in figure 4.3. Some additional peaks appear in the XRD result after the growth. These peaks correspond to the BAs peaks calculated with the lattice parameters of $a=4.777 \text{ \AA}$, $\alpha=90.0^\circ$, $\beta=90.0^\circ$, $\gamma=90.0^\circ$. After the XRD analysis, the BAs crystals on boron pellets are examined with Raman spectroscopy. The Raman spectroscopy gives only one sharp peak at the Raman shift of 699 cm^{-1} . In comparison to reported Raman spectra measured on BAs,^{17,18} the Raman peak observed for the BAs crystals grown in this work is close to that reported for isotopically pure ^{11}BAs as shown in figure 4.3.

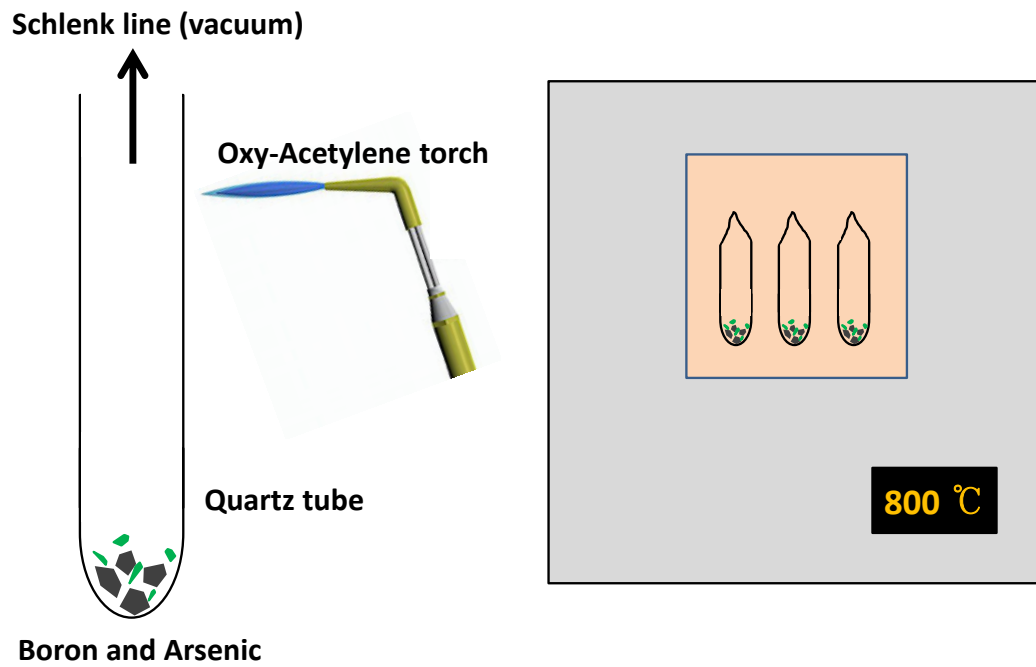


Figure 4.1: Boron arsenide synthesizing process: Boron and arsenic pellets are mixed together in a quartz tube, and evacuated for one hour. The tube is sealed with oxy-acetylene torch, and the ampoules are placed in a box furnace at 800 °C for 72 hours. The furnace is cooled down slowly at a rate of 0.1 °C/min, and the growth process is completed.

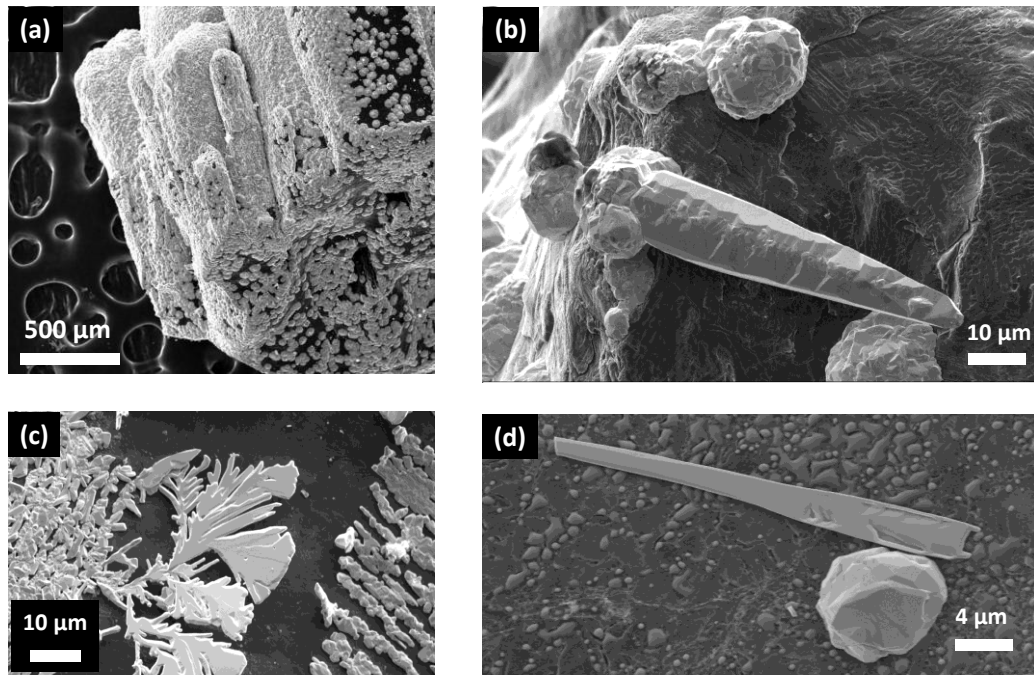


Figure 4.2: Scanning electron micrographs (SEM) taken after the growth. Boron pellets are covered by various shapes of BAs crystals, including polycrystalline coating (a), small rods (b), dendrites (c), and platelets (d).

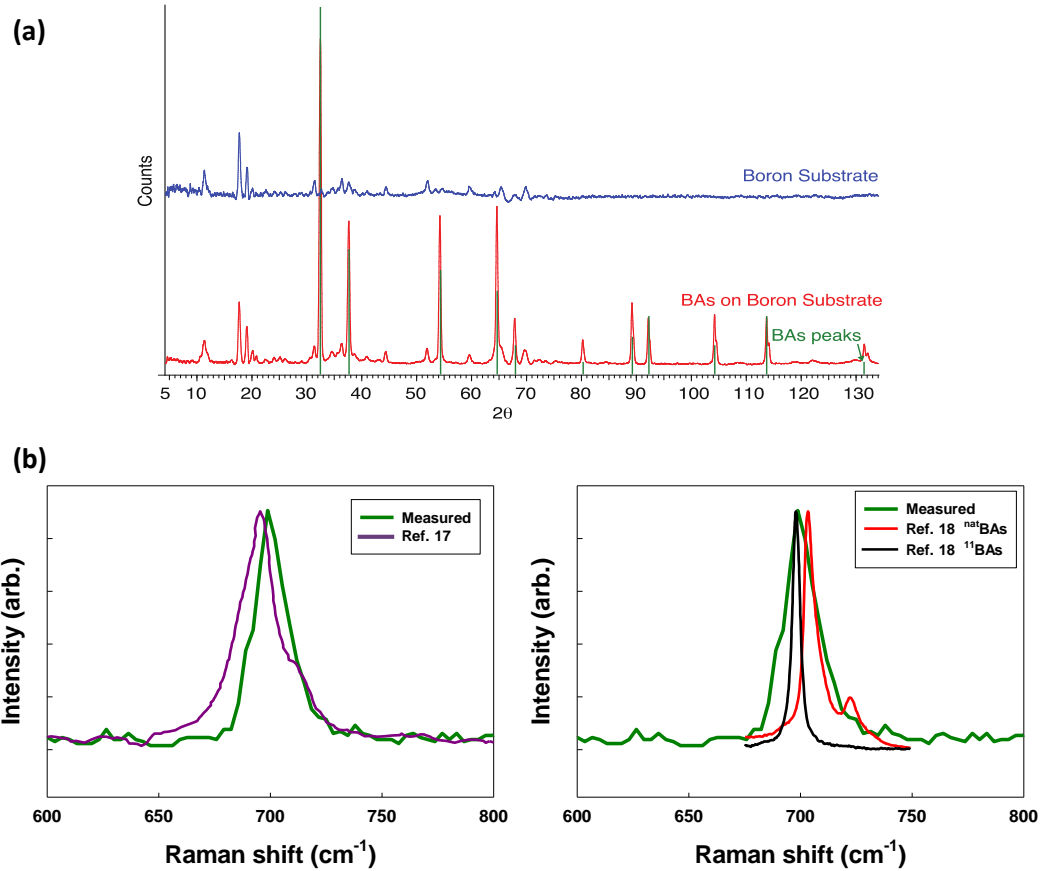


Figure 4.3: (a) XRD results of the boron pellets before and after the growth. (b) Raman spectroscopy of BAs crystals grown in this work in comparison to the results reported in Ref. 17 and 18.

4.3 EXPERIMENTAL RESULTS

4.3.1 Sample preparation

The BAs single crystalline nanostructures can be found with optical microscopy and scanning electron microscopy. Once an appropriate nanostructure sample is found, the sample is picked up with a sharp tungsten probe controlled by a XYZ micro

manipulator as shown in figure 4.4 (a). The sample is transferred on a separate piece of substrate coated with a polyvinyl alcohol (PVA) layer. Figure 4.4 (b) shows the transferred BAs nanostructure sample. At this stage, the transferred sample is verified as BAs crystal with the use of Raman spectroscopy. When the sample is probed by Raman spectroscopy, the Raman laser power should be minimized to prevent sample damage. Figure 4.5 shows the Raman shift measured on the specific sample shown in figure 4.4 (b). It has only one peak at 699 cm^{-1} , which matches exactly with literature values and previous results.^{17,18}

The BAs nanostructure sample is assembled on a prefabricated device with a transfer method based on a polymethyl methacrylate (PMMA) transfer layer. The PMMA layer is spun on the piece of wafer where the BAs sample is located. The PMMA layer is separated together with the BAs nanostructure sample from the wafer by dissolving the PVA layer in deionized water. It is easier to use a sharp probe or even a pair of tweezers to handle the larger PMMA layer than the much smaller BAs sample. The PMMA layer is transferred onto a prefabricated suspended device and aligned accurately with the device, as shown in figure 4.6. After assembling and aligning the BAs sample on the measurement device, the PMMA layer is removed in a tube furnace, which is kept at a temperature of 350°C and the pressure of 1 Torr with argon atmosphere. After the device is heated for two hours under these conditions, the PMMA layer is completely removed. Figure 4.7 shows the completed device with a BAs sample ready for thermal and thermoelectric measurements. The width and thickness are measured at five different points with scanning electron micrographs as shown in figure 4.7. The width is 1760 ± 210 nm, and the thickness is 591 ± 50 nm with 95% confidence level from student's t-distribution.

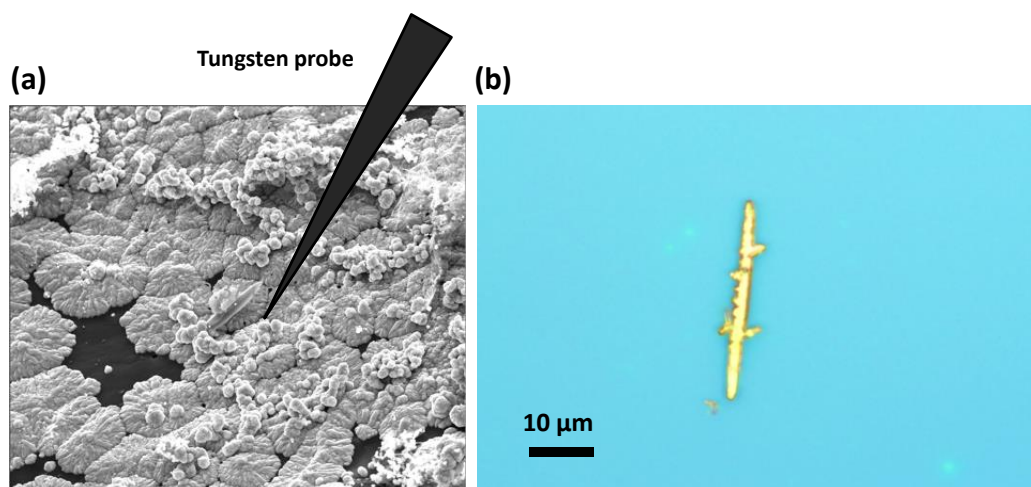


Figure 4.4: A BAs nanostructure crystal grown on the surface of boron pellet can be picked up with sharp tungsten probe (a), and transferred on a separate substrate coated with PVA for assembling on a suspended device (b).

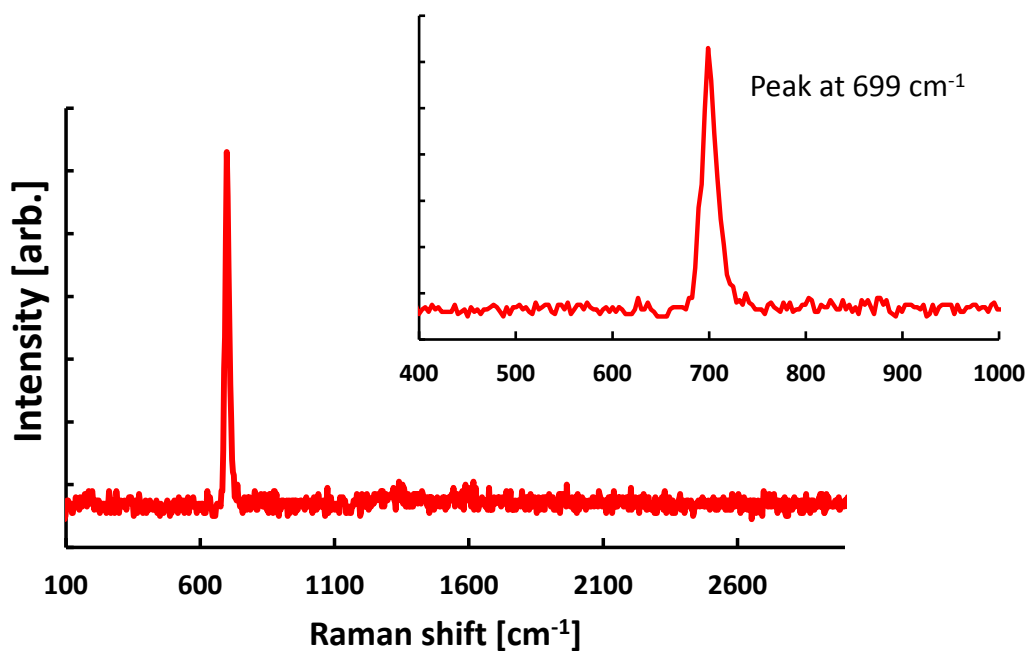


Figure 4.5: The BAs nanostructure sample shown in figure 4.4 (b) is characterized with Raman spectroscopy. It shows only one peak at 699 cm⁻¹, which matches with the reported values.

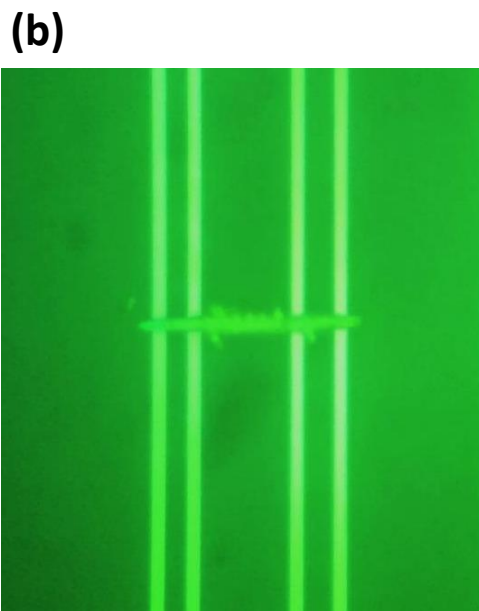
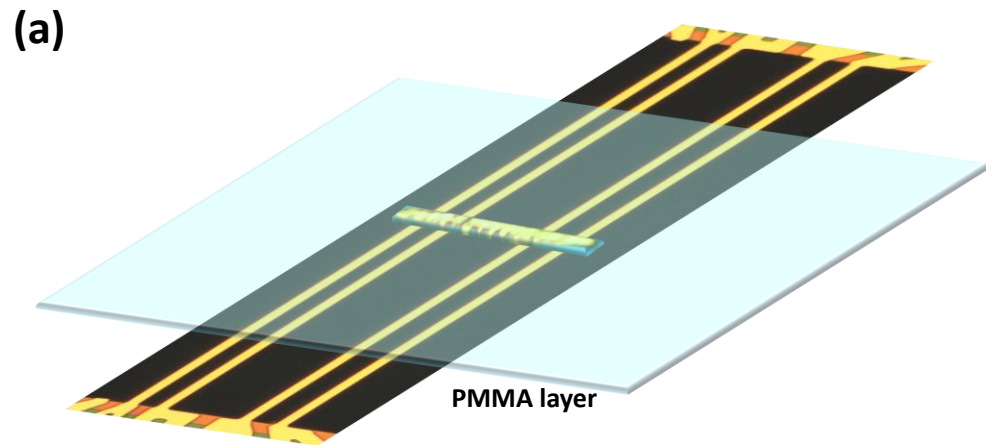


Figure 4.6: The BAs nanostructure sample is transferred and aligned on a prefabricated suspended device together with the PMMA carrier layer as shown in (a), and (b) is the optical micrograph of the assembled PMMA, BAs, and suspended device.

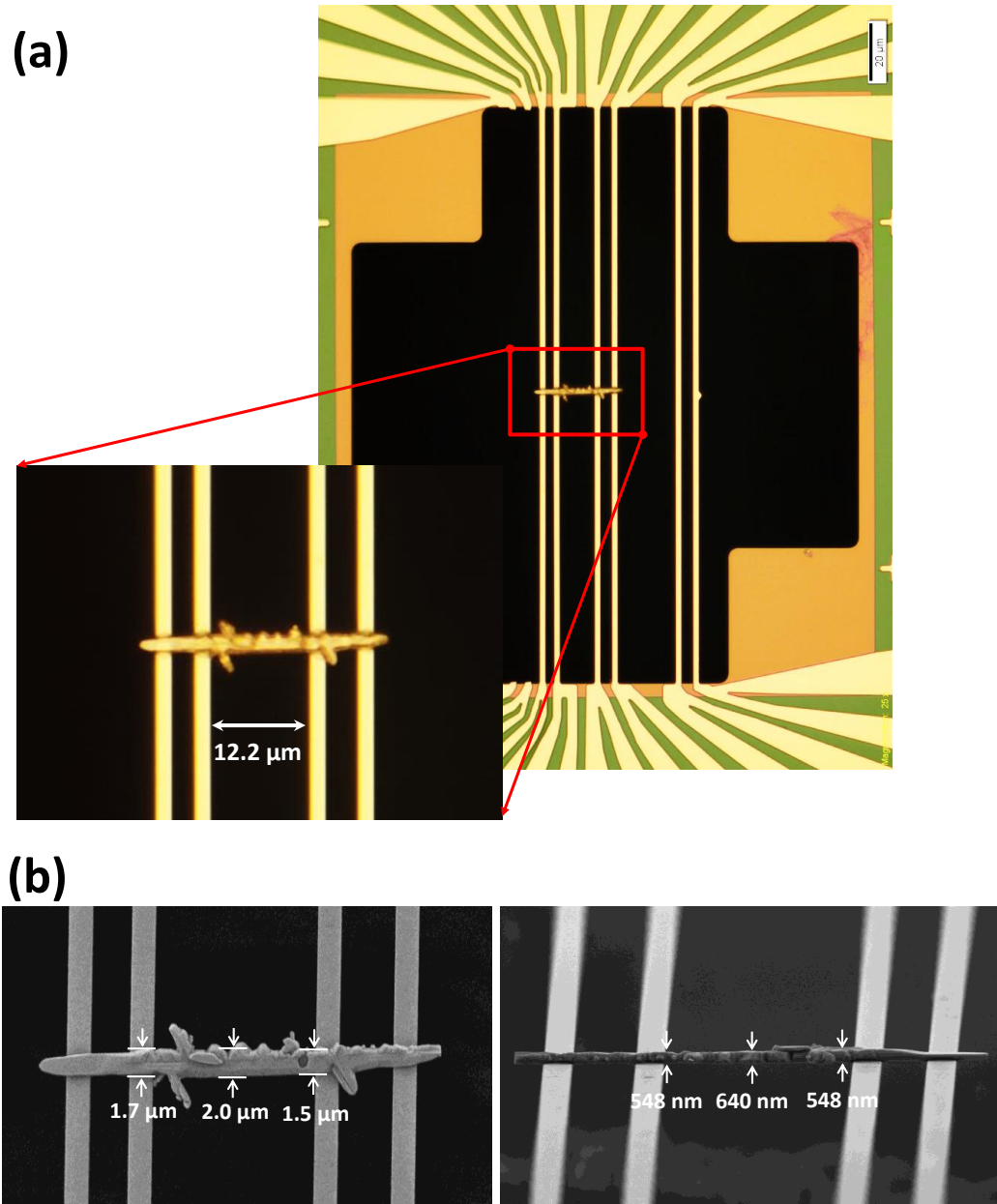


Figure 4.7: The PMMA carrier layer is removed by heating at 350°C. Optical micrographs show the completed device for thermoelectric measurement (a). The gap between two inner suspended thermometer lines is 12.2 μm . SEM micrographs are taken for measuring the width and thickness of the sample (b).

4.3.2 Measurement results

The measurement is performed with the new four probe thermal property measurement method described in chapter three of this dissertation and reported in a recent journal article.³ This method is particularly useful for high-thermal conductivity samples such as BAs. For such a sample, the intrinsic thermal resistance of the suspended segment could be very low, and comparable to the contact thermal resistances between the sample and the suspended thermometer line. The new four probe thermal measurement method is able to eliminate the influence of the contact thermal resistances from the measurement. The detailed measurement procedure of this measurement method is described in chapter three of this dissertation. One difference from the Si nanowire measurement described in chapter three is that this BAs nanostructure sample makes electrical contact to all four thermometer lines, so that a floating voltage source needs to be used for the heater line and the resistance and temperature rises in the other three thermometer lines need to be measured with a lock-in amplifier one at a time to prevent electrical current flowing through the BAs sample during the thermal measurements. The electrical contact made between the BAs sample and the thermometer line also allows for the measurement of the Seebeck coefficient and four-probe electrical conductivity of the BAs sample. Figure 4.8 shows the measurement results of thermal resistances in the device at three temperatures of 250K, 300K, and 350K. As shown in figure 4.8(a), the thermal resistances of the four suspended thermometer lines (R_b) are almost the same because they are designed to have the same dimension. Figure 4.8 (b) shows the intrinsic thermal resistance of the middle suspended segment of the BAs sample (R_2) increases slightly with decreasing temperature, corresponding to increasing thermal conductivity with decreasing temperature in the temperature range of the measurement. The opposite temperature dependences of R_b and R_2 decreases the R_2/R_b ratio with decreasing

temperature, which results in a decreased temperature difference between the thermometer lines. Figure 4.9 shows an example of the measured contact point temperature of the second and third thermometer lines when the sample stage temperature is at 300K when the second suspended thermometer line is the heater line. Although the temperature difference between the two contact points is very small, a difference is still discernable in the slopes of the contact point temperature rise versus the heating rate IV of the heater line. These slopes are used to determine R_2 , $R_{c,2}$, and $R_{c,3}$, as explained in chapter three. When the sample stage temperature decreases to temperature 250K, the difference between the two contact point temperatures decreases and approaches the measurement uncertainty, so that there is a large uncertainty in the obtained R_2 value at 250 K and below. In addition, Figure 4.8 (b) shows that the obtained contact thermal resistances ($R_{c,2}$ and $R_{c,3}$) are not much smaller than the intrinsic thermal resistance of the BAs sample (R_2), so that it is essential to measure and eliminate the influence of the large contact thermal resistance, as shown here with the four probe method.

Figure 4.10 shows the obtained thermal conductivity of the BAs nanostructure sample. The thickness of the BAs sample is measured with tilted SEM as shown in figure 4.7, and it is an about 600 nm thick sample. The values of thermal conductivity are $133 \text{ Wm}^{-1}\text{K}^{-1}$ ($98.4 - 173 \text{ Wm}^{-1}\text{K}^{-1}$), $184 \text{ Wm}^{-1}\text{K}^{-1}$ ($140 - 232 \text{ Wm}^{-1}\text{K}^{-1}$), and $205 \text{ Wm}^{-1}\text{K}^{-1}$ ($130 - 327 \text{ Wm}^{-1}\text{K}^{-1}$) at the temperature of 350K, 300K, and 250K, respectively. The decreasing thermal conductivity with increasing temperature reveals the effects of umklapp phonon-phonon scattering, which increases with increasing temperature. However, the temperature dependence is rather weak, suggesting that umklapp phonon scattering is not dominant compared to other scattering processes such as diffuse phonon-boundary scattering and phonon-defect scattering. The diffuse phonon-boundary scattering mean free path is calculated to be $(4wt/\pi)^{1/2} = 1150 \text{ nm}$, where $w = 1700 \text{ nm}$

and $t = 600$ nm are the width and thickness of the middle suspended segment of the BAs sample. At this phonon-boundary scattering mean free path, the room temperature thermal conductivity has been calculated by the authors of reference 5 to be $917 \text{ Wm}^{-1}\text{K}^{-1}$ for isotopically pure ^{11}BAs and $774 \text{ Wm}^{-1}\text{K}^{-1}$ for natural BAs. The measured value of $184 \text{ Wm}^{-1}\text{K}^{-1}$ is still considerably lower than the calculation result. One possible cause of the discrepancy is the presence of As vacancies in the measured BAs sample. Such vacancies can considerably reduce the thermal conductivity of bulk BAs, as reported in a recent work.¹⁵

Because the BAs sample makes electrical contacts to all four suspended thermometer lines, the thermoelectric and electrical properties of the sample can be measured. When the first thermometer line is used as the heater line, the temperature drop along the middle suspended segment can be obtained as $\theta_{2,1} - \theta_{3,1} = R_2(Q_{1,1} + Q_{2,1})$ based on the thermal circuit in figure 3.2 of chapter three, where the intrinsic thermal resistance of the middle suspended segment (R_2) has been determined from the four-probe thermal transport measurement method. In addition, the thermovoltage ($V_{\text{TE},23}$) between the two middle contacts to the BAs sample can be measured when the first thermometer line is the heater line. Because the Seebeck coefficient of the metal thermometer line is negligible compared to that of the semiconducting BAs, the Seebeck coefficient of the BAs sample can be obtained by $S = -V_{\text{TE},23}/(\theta_{2,1} - \theta_{3,1}) = -V_{\text{TE},23}/R_2(Q_{1,1} + Q_{2,1})$. In addition, the electrical resistance of the middle suspended segment of the BAs sample can be measured in a four-probe configuration. During the four-probe electrical measurement with an electrical current (I) flowing between the two outer contacts to the BAs sample, the measured voltage drop (ΔV) along the middle suspended segment can consist of a small thermovoltage component, which is caused by Peltier heating and cooling at the two outer electrical contacts. For the BAs sample with

high thermal conductivity and low thermoelectric figure of merit (ZT), it can be shown that the thermovoltage drop is negligible compared to the IR voltage drop, so that the electrical resistance of the middle segment can be obtained as $R = \Delta V/I$.

Figure 4.11 shows the measured Seebeck coefficient and electrical resistivity of the BAs sample. The measured Seebeck coefficient is positive, suggesting that the sample is a p type semiconductor. The electrical resistivity increases linearly with temperature between 250 K and 350 K. The linear trend suggests that the sample is degenerately doped with a high hole concentration, consistent with the case of a high concentration of As vacancies. The value at room temperature is about 180 $\mu\text{V/K}$ at 300K, which is comparable to that of well-known thermoelectric materials such as bismuth telluride (Bi_2Te_3).¹⁹ In addition, the measured electrical resistivity of the BAs sample is also comparable to that of Bi_2Te_3 , so that a rather high room-temperature power factor (S^2/ρ) is obtained for BAs. However, the thermal conductivity of the BAs sample is two orders of magnitude higher than that of Bi_2Te_3 , so that the ZT value is very small.

The thermoelectric property measurements can provide valuable information on the chemical potential and charge carrier concentration and mobility of the BAs samples.²⁰⁻²³ According to a single parabolic band, the measured Seebeck coefficient can be used to obtain the Fermi level, hole carrier concentration, and Lorenz number ($L = k_e/\sigma T$) according to,

$$S = \frac{k_B}{e} \left\{ \frac{(r_p + \frac{5}{2})F_{r_p+3/2}(\eta)}{(r_p + \frac{3}{2})F_{r_p+1/2}(\eta)} - \eta \right\} \quad (1), \quad F_r(\eta) = \int_0^\infty \frac{\zeta^r}{\exp(\zeta - \eta) + 1} d\zeta \quad (2)$$

$$p = \frac{(2m_p^*k_B T)^{\frac{3}{2}}}{2\pi^2\hbar^3} F_{\frac{1}{2}}(\eta) \quad (3), \quad L = \left(\frac{k_B}{e}\right)^2 \left\{ \frac{3F_2(\eta)}{F_0(\eta)} - \frac{4F_1(\eta)^2}{F_0(\eta)^2} \right\} \quad (4)$$

where the reduced Fermi level $\eta = E_F / k_B T$, and $r_p = -1/2$ for acoustic phonon and boundary scattering dominant condition. Figure 4.12 shows the calculation results. The calculated hole concentration is at the order of 10^{19} cm^{-3} , which is rather high. This high hole concentration is in agreement with high As vacancies in the sample. Based on the Lorenz number calculated from this model and the measured Seebeck coefficient, the electronic contribution to total thermal conductivity is about two orders of magnitude smaller than the lattice contribution.

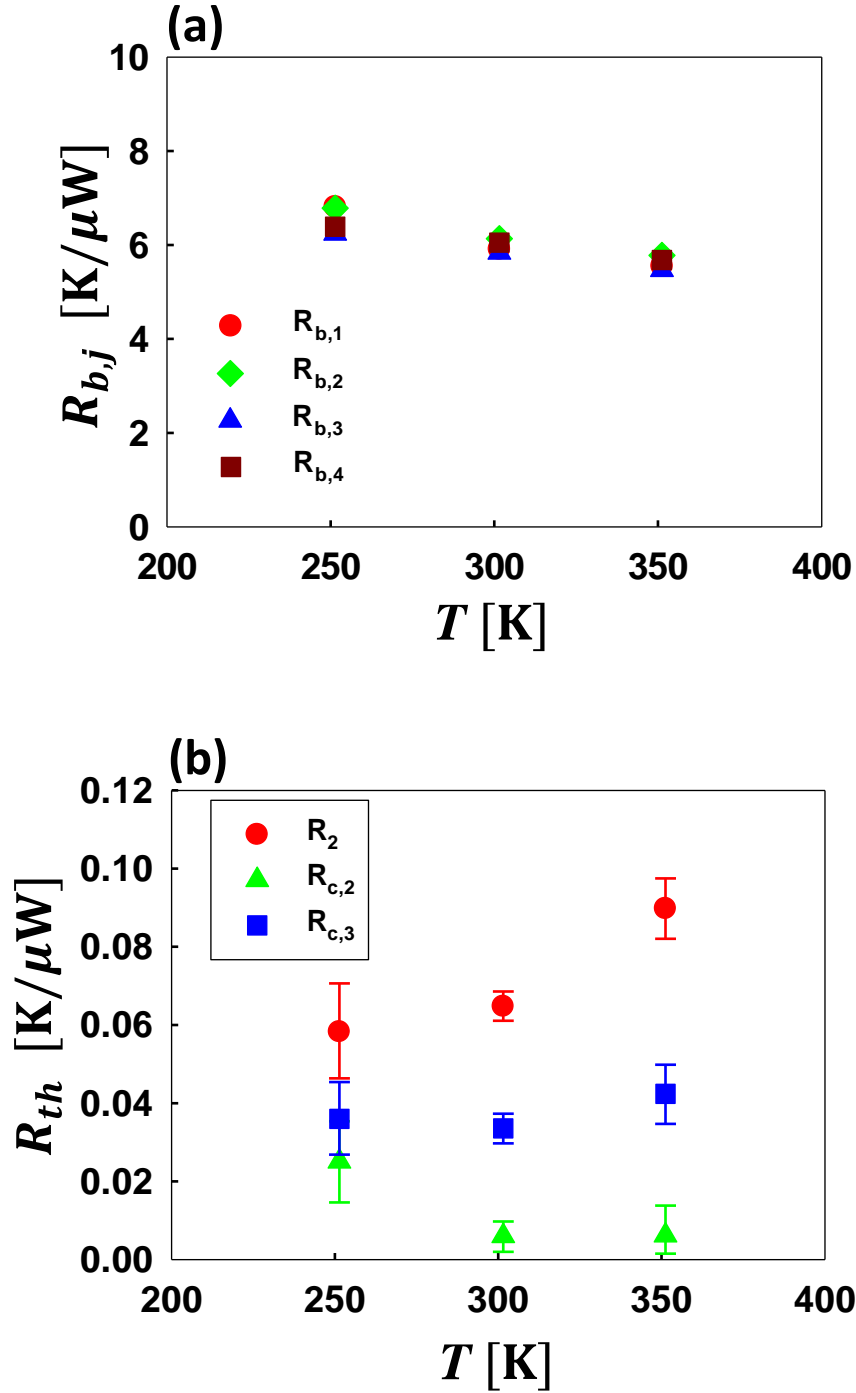


Figure 4.8: Thermal resistances of suspended thermometer lines (a), and intrinsic thermal resistance of BAs (R_2) and contact thermal resistances between the sample and two middle thermometer lines ($R_{c,2}$, $R_{c,3}$) (b).

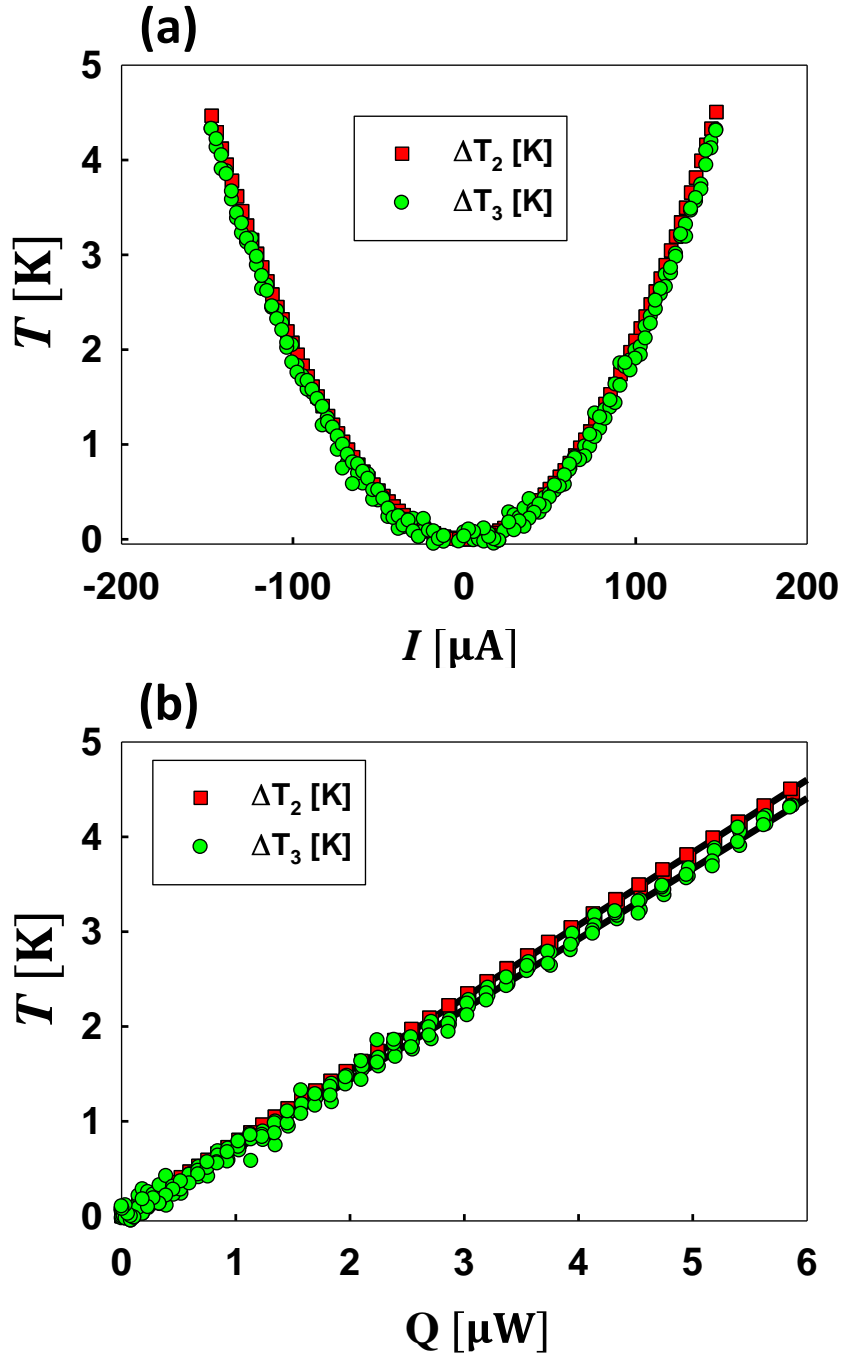


Figure 4.9: Measured point temperature rise at the contacts between the BA sample and two inner thermometer lines at 300K, which is plotted by heating current (a) and heating rate (b). They are very close, but still detectable the different slope in (b).

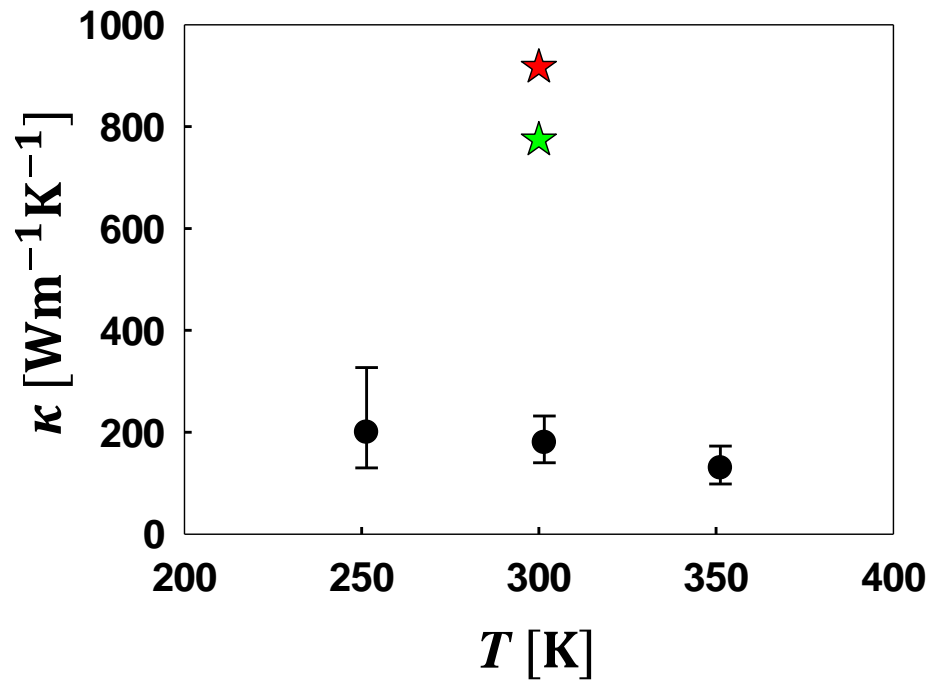


Figure 4.10: Measured thermal conductivity of BAs nanostructure sample (black circles). Red and green star indicates the calculation value of 1140 nm diameter ^{11}BAs and natural BAs rods with an infinite length, respectively.

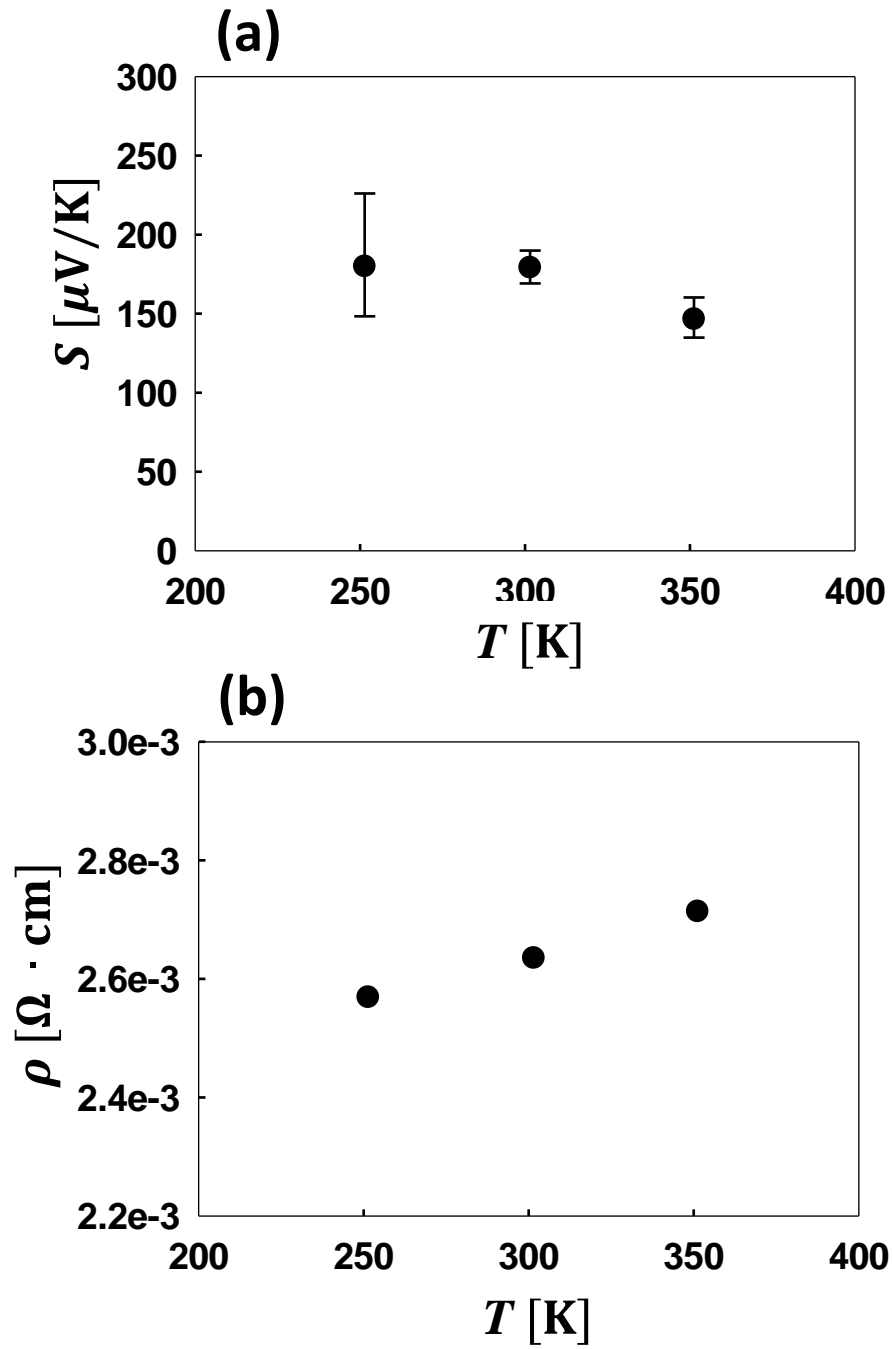


Figure 4.11: Measured Seebeck coefficient (a), and electrical resistivity (b) of the BA nanostructure sample.

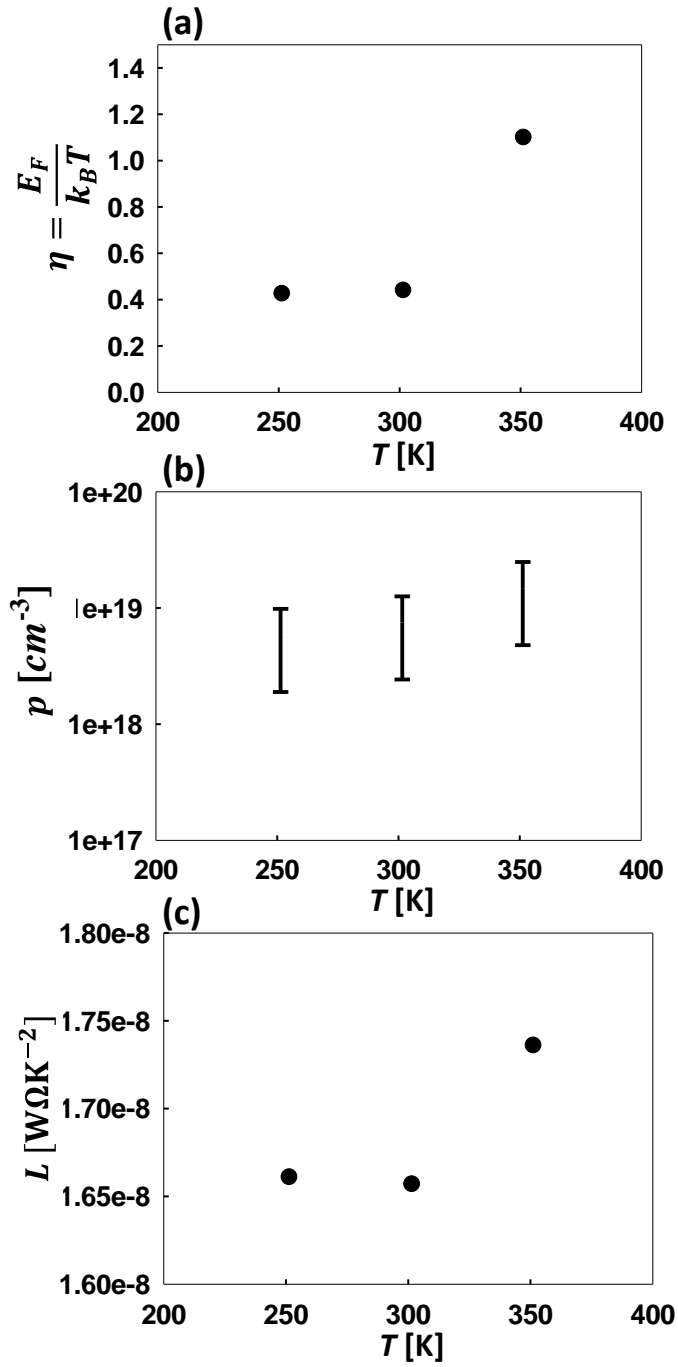


Figure 4.12: Calculated reduced Fermi level (a), hole carrier concentration (b), and Lorenz number (c) from the measured Seebeck coefficient according to the single parabolic band model.

4.4 SUMMARY

Single crystalline boron arsenide (BAs) nanostructure materials such as nanorods, nanowires, and nanoplates are synthesized by vapor transport method. The grown BAs nanostructures are characterized as high quality BAs materials with powder X-ray diffraction, Raman spectroscopy, and scanning electron microscopy. One of the BAs nanostructure sample is transferred successfully on a prefabricated suspended device for four-probe thermal and thermoelectric transport measurements. The four-probe measurement method can determine the contact thermal resistances and the intrinsic thermal resistance of the middle suspended segment. The measured intrinsic thermal conductivity of the BAs nanostructure increases slightly with decreasing temperature. The weak temperature dependence reveals that umklapp phonon-phonon scattering is not dominant compared to phonon-boundary and phonon defect scattering. The room-temperature value of about $184 \text{ Wm}^{-1}\text{K}^{-1}$ at 300K is higher than that of bulk silicon, but still lower than the theoretical prediction for BAs rods with a comparable phonon-boundary scattering cross section of about 1150 nm.

Moreover, the Seebeck coefficient and the electrical resistivity of the BAs sample have also been measured by the four-probe device. The positive Seebeck coefficient and linearly increased electrical resistivity with increasing temperature suggests that the sample is degenerately p-doped, potentially because of high As vacancy concentration. The thermoelectric measurement can be used to evaluate the As vacancy concentration, which is difficult to be measured with other methods. The measured room-temperature Seebeck coefficient, electrical conductivity, and power factor are comparable to well-known thermoelectric material Bi_2Te_3 . However, the high thermal conductivity of BAs results in a small thermoelectric figure of merit. The carrier concentration is calculated from the measured Seebeck coefficient according to a single parabolic band model. The

obtained hole concentration is on the level of 10^{19} cm^{-3} . The high hole concentration is in agreement with high As vacancies concentration in the BAs sample. The electronic contribution to the total thermal conductivity is found to be negligible for the BAs sample.

The measurement of this BAs sample shows that the thermal resistance of the suspended thermometer lines of the four-probe device should be modified to match the thermal resistance of the BAs sample in order to improve the measurement sensitivity, especially at low temperatures. With such efforts, the obtained size-dependent thermal and thermoelectric properties of BAs can help to develop a better understanding of phonon transport in this material with potentially record high thermal conductivity.

REFERENCES

1. A. Boudjemline, M. M. Islam, L. Louail and B. Diawara, *Physica B: Condensed Matter* 406 (22), 4272-4277 (2011).
2. J. A. Perri, S. La Placa and B. Post, *Acta Crystallographica* 11 (4), 310 (1958).
3. J. Kim, E. Ou, D. P. Sellan and L. Shi, *Review of Scientific Instruments* 86 (4), 044901 (2015).
4. S. V. Garimella, A. S. Fleischer, J. Y. Murthy, A. Keshavarzi, R. Prasher, C. Patel, S. H. Bhavnani, R. Venkatasubramanian, R. Mahajan, Y. Joshi, B. Sammakia, B. A. Myers, L. Chorosinski, M. Baelmans, P. Sathyamurthy and P. E. Raad, *Components and Packaging Technologies, IEEE Transactions on* 31 (4), 801-815 (2008).
5. S. Berber, Y.-K. Kwon and D. Tománek, *Physical Review Letters* 84 (20), 4613-4616 (2000).
6. J. E. Graebner, S. Jin, G. W. Kammlott, J. A. Herb and C. F. Gardinier, *Nature* 359 (6394), 401-403 (1992).
7. L. Wei, P. K. Kuo, R. L. Thomas, T. R. Anthony and W. F. Banholzer, *Physical Review Letters* 70 (24), 3764-3767 (1993).
8. A. A. Balandin, S. Ghosh, W. Bao, I. Calizo, D. Teweldebrhan, F. Miao and C. N. Lau, *Nano Letters* 8 (3), 902-907 (2008).
9. J. Hone, M. Whitney, C. Piskoti and A. Zettl, *Physical Review B* 59 (4), R2514-R2516 (1999).
10. J. Che, T. Çağın, W. Deng and W. A. Goddard, *The Journal of Chemical Physics* 113 (16), 6888-6900 (2000).
11. S. Ghosh, I. Calizo, D. Teweldebrhan, E. P. Pokatilov, D. L. Nika, A. A. Balandin, W. Bao, F. Miao and C. N. Lau, *Applied Physics Letters* 92 (15), 151911 (2008).
12. J. H. Seol, I. Jo, A. L. Moore, L. Lindsay, Z. H. Aitken, M. T. Pettes, X. Li, Z. Yao, R. Huang, D. Broido, N. Mingo, R. S. Ruoff and L. Shi, *Science* 328 (5975), 213-216 (2010).
13. G. A. Slack, *Journal of Physics and Chemistry of Solids* 34 (2), 321-335 (1973).
14. L. Lindsay, D. A. Broido and T. L. Reinecke, *Physical Review Letters* 111 (2), 025901 (2013).
15. B. Lv, Y. Lan, X. Wang, Q. Zhang, Y. Hu, A. J. Jacobson, D. Broido, G. Chen, Z. Ren and C.-W. Chu, *Applied Physics Letters* 106 (7), 074105 (2015).
16. S. Wang, S. F. Swingle, H. Ye, F.-R. F. Fan, A. H. Cowley and A. J. Bard, *Journal of the American Chemical Society* 134 (27), 11056-11059 (2012).

17. R. G. Greene, H. Luo, A. L. Ruoff, S. S. Trail and F. J. DiSalvo, *Physical Review Letters* 73 (18), 2476-2479 (1994).
18. V. G. Hadjiev, M. N. Iliev, B. Lv, Z. F. Ren and C. W. Chu, *Physical Review B* 89 (2), 024308 (2014).
19. J. Zhou, C. Jin, J. H. Seol, X. Li and L. Shi, *Applied Physics Letters* 87 (13), 133109 (2005).
20. S. M. Ku, *Journal of The Electrochemical Society* 113 (8), 813-816 (1966).
21. J. H. Seol, A. L. Moore, S. K. Saha, F. Zhou, L. Shi, Q. L. Ye, R. Scheffler, N. Mingo and T. Yamada, *Journal of Applied Physics* 101 (2), 023706 (2007).
22. F. Zhou, J. Szczech, M. T. Pettes, A. L. Moore, S. Jin and L. Shi, *Nano Letters* 7 (6), 1649-1654 (2007).
23. X. Chen, A. Weathers, D. Salta, L. Zhang, J. Zhou, J. B. Goodenough and L. Shi, *Journal of Applied Physics* 114 (17), 173705 (2013).

Chapter 5: Conclusion

Nanostructured materials exhibit unique size dependent thermal and thermoelectric properties because their characteristic dimensions are comparable to the mean free path or even wavelength of heat carriers including electrons and phonons. This dissertation presents the development of nanoscale thermal and thermoelectric measurement methods to obtain a better understanding of the size-dependent thermal and thermoelectric properties of several material systems, including bismuth antimony telluride nanoplates, silicon nanowires, and boron arsenide nanorods. These materials are either already in use in current electronic or thermoelectric devices, or being investigated for future-generation device structures.

The thermoelectric properties of bismuth antimony telluride $(\text{Bi}_{1-x}\text{Sb}_x)_2\text{Te}_3$ nanostructures synthesized by two different methods are characterized with the use of a four-probe thermoelectric measurement method based on a suspended measurement device. Five $(\text{Bi}_{1-x}\text{Sb}_x)_2\text{Te}_3$ samples grown by a vapor solid method in a tube furnace are measured with different nominal Sb concentration of $x=0.07, 0.25, 0.5, 0.7, 0.95$. The measurement results of Seebeck coefficient and thermoelectric figure of merit (zT) peaks at x close to 0.5. The sign of the Seebeck coefficient shows the change of the majority charge carriers from electrons to holes when x is increased from 0.07 to 0.25. Another $(\text{Bi}_{1-x}\text{Sb}_x)_2\text{Te}_3$ film sample with $x=0.95$ grown on GaAs substrate by metal organic chemical vapor deposition (MOCVD) is measured, and shows a degenerate p-type behavior. These measurement results represent an initial but important step toward developing a better understanding of the effects of chemical composition and size confinement in the $(\text{Bi}_{1-x}\text{Sb}_x)_2\text{Te}_3$ system.

One major innovation of this dissertation is the establishment of a new four probe thermal transport measurement method for obtaining both the intrinsic thermal resistance and contact thermal resistance of a nanostructure sample. Compared to the rather complicated device design used for four-probe thermoelectric measurements of $(\text{Bi}_{1-x}\text{Sb}_x)_2\text{Te}_3$ nanostructures, the device for the new four-probe thermal transport measurement consists of only four suspended thermometer lines, can be readily fabricated with established semiconductor processing technique, and does not require electrical contact between the sample and the measurement device. The effectiveness of the measurement method is demonstrated with its application for measuring two silicon (Si) nanowires with different cross section areas. The measurement results are compared to two theoretical calculation results. This new measurement method is expected to enable accurate measurements of unique size dependent thermal transport properties in nanostructure materials, which can help to refine theoretical models.

The new four-probe thermal transport measurement method is employed to obtain the intrinsic thermal conductivity of a boron arsenide (BAs) nanorod sample. In addition, the method is further developed to obtain the intrinsic Seebeck coefficient together with the electrical conductivity of the sample. The thermal transport measurement results suggest that the thermal conductivity of the BAs nanostructure is suppressed by both phonon-boundary scattering and phonon scattering by point defects caused by As vacancies. However, the suppressed thermal conductivity in the BAs sample with an equivalent diameter close to 1150 nm is still as high as $184 \text{ Wm}^{-1}\text{K}^{-1}$, and higher than that of bulk silicon. In addition, the thermoelectric measurement reveals rather high power factor in BAs. Nevertheless, the thermoelectric figure of merit of the BAs is very low because of the high thermal conductivity. Moreover, the thermoelectric measurement data support the presence of high As vacancies in the sample.

The experimental methods presented in this dissertation have enhanced the capability in probing intriguing size-dependent thermal and thermoelectric properties of nanostructures. Further efforts in employing and refining these experimental methods are expected to lead to a better understanding of nanoscale thermal and thermoelectric transport phenomena in BAs, $(\text{Bi}_{1-x}\text{Sb}_x)_2\text{Te}_3$, and other materials systems with potential applications in thermal management and thermoelectric energy conversion.

Bibliography

1. Balandin, A.A., et al., *Superior Thermal Conductivity of Single-Layer Graphene*. Nano Letters, 2008. **8**(3): p. 902-907.
2. Berber, S., Y.-K. Kwon, and D. Tománek, *Unusually High Thermal Conductivity of Carbon Nanotubes*. Physical Review Letters, 2000. **84**(20): p. 4613-4616.
3. Boudjemline, A., et al., *Electronic and optical properties of BAs under pressure*. Physica B: Condensed Matter, 2011. **406**(22): p. 4272-4277.
4. Cai, W., et al., *Thermal Transport in Suspended and Supported Monolayer Graphene Grown by Chemical Vapor Deposition*. Nano Letters, 2010. **10**(5): p. 1645-1651.
5. Canetta, C., S. Guo, and A. Narayanaswamy, *Measuring thermal conductivity of polystyrene nanowires using the dual-cantilever technique*. Review of Scientific Instruments, 2014. **85**(10): p. 104901.
6. Cao, H., et al., *Topological insulator Bi₂Te₃ films synthesized by metal organic chemical vapor deposition*. Applied Physics Letters, 2012. **101**(16): p. 162104.
7. Che, J., et al., *Thermal conductivity of diamond and related materials from molecular dynamics simulations*. The Journal of Chemical Physics, 2000. **113**(16): p. 6888-6900.
8. Chen, G. and M. Neagu, *Thermal conductivity and heat transfer in superlattices*. Applied Physics Letters, 1997. **71**(19): p. 2761-2763.
9. Chen, R., et al., *Thermal Conductance of Thin Silicon Nanowires*. Physical Review Letters, 2008. **101**(10): p. 105501.
10. Chen, X., et al., *Effects of (Al,Ge) double doping on the thermoelectric properties of higher manganese silicides*. Journal of Applied Physics, 2013. **114**(17): p. 173705.
11. Chowdhury, I., et al., *On-chip cooling by superlattice-based thin-film thermoelectrics*. Nat Nano, 2009. **4**(4): p. 235-238.
12. Faugeras, C., et al., *Thermal Conductivity of Graphene in Corbino Membrane Geometry*. ACS Nano, 2010. **4**(4): p. 1889-1892.
13. Garimella, S.V., et al., *Thermal Challenges in Next-Generation Electronic Systems*. Components and Packaging Technologies, IEEE Transactions on, 2008. **31**(4): p. 801-815.

14. Ghaemi, P., R.S.K. Mong, and J.E. Moore, *In-Plane Transport and Enhanced Thermoelectric Performance in Thin Films of the Topological Insulators B_2Te_3 and Bi_2Se_3* . Physical Review Letters, 2010. **105**(16): p. 166603.
15. Ghosh, S., et al., *Extremely high thermal conductivity of graphene: Prospects for thermal management applications in nanoelectronic circuits*. Applied Physics Letters, 2008. **92**(15): p. 151911.
16. Glassbrenner, C.J. and G.A. Slack, *Thermal Conductivity of Silicon and Germanium from 3°K to the Melting Point*. Physical Review, 1964. **134**(4A): p. A1058-A1069.
17. Goyal, V., D. Teweldebrhan, and A.A. Balandin, *Mechanically-exfoliated stacks of thin films of Bi_2Te_3 topological insulators with enhanced thermoelectric performance*. Applied Physics Letters, 2010. **97**(13): p. 133117.
18. Graebner, J.E., et al., *Large anisotropic thermal conductivity in synthetic diamond films*. Nature, 1992. **359**(6394): p. 401-403.
19. Greene, R.G., et al., *Pressure Induced Metastable Amorphization of BAs: Evidence for a Kinetically Frustrated Phase Transformation*. Physical Review Letters, 1994. **73**(18): p. 2476-2479.
20. Hadjiev, V.G., et al., *Anomalous vibrational properties of cubic boron arsenide*. Physical Review B, 2014. **89**(2): p. 024308.
21. Harman, T.C., et al., *Quantum Dot Superlattice Thermoelectric Materials and Devices*. Science, 2002. **297**(5590): p. 2229-2232.
22. Hicks, L.D. and M.S. Dresselhaus, *Effect of quantum-well structures on the thermoelectric figure of merit*. Physical Review B, 1993. **47**(19): p. 12727-12731.
23. Hicks, L.D., et al., *Experimental study of the effect of quantum-well structures on the thermoelectric figure of merit*. Physical Review B, 1996. **53**(16): p. R10493-R10496.
24. Hone, J., et al., *Thermal conductivity of single-walled carbon nanotubes*. Physical Review B, 1999. **59**(4): p. R2514-R2516.
25. Hsu, I.-K., et al., *Optical measurement of thermal transport in suspended carbon nanotubes*. Applied Physics Letters, 2008. **92**(6): p. 063119.
26. <http://www.itrs.net>. <http://www.itrs.net>.
27. Jang, W., et al., *Thickness-Dependent Thermal Conductivity of Encased Graphene and Ultrathin Graphite*. Nano Letters, 2010. **10**(10): p. 3909-3913.
28. Jo, I., et al., *Thermal Conductivity and Phonon Transport in Suspended Few-Layer Hexagonal Boron Nitride*. Nano Letters, 2013. **13**(2): p. 550-554.
29. Kim, J., et al., *A four-probe thermal transport measurement method for nanostructures*. Review of Scientific Instruments, 2015. **86**(4): p. 044901.

30. Kim, P., et al., *Thermal Transport Measurements of Individual Multiwalled Nanotubes*. Physical Review Letters, 2001. **87**(21): p. 215502.
31. Kim, R., S. Datta, and M.S. Lundstrom, *Influence of dimensionality on thermoelectric device performance*. Journal of Applied Physics, 2009. **105**(3): p. 034506.
32. Kong, D., et al., *Few-Layer Nanoplates of Bi_2Se_3 and Bi_2Te_3 with Highly Tunable Chemical Potential*. Nano Letters, 2010. **10**(6): p. 2245-2250.
33. Ku, S.M., *Preparation and Properties of Boron Arsenides and Boron Arsenide-Gallium Arsenide Mixed Crystals*. Journal of The Electrochemical Society, 1966. **113**(8): p. 813-816.
34. Kusano, D. and Y. Hori, *Thermoelectric Properties of p-type $(\text{Bi}_2\text{Te}_3)_{0.2}(\text{Sb}_2\text{Te}_3)_{0.8}$ Thermoelectric Material Doped with PbTe*. Journal of the Japan Institute of Metals, 2002. **66**(10): p. 1063-1065.
35. Kuznetsov, V.L., et al., *High performance functionally graded and segmented Bi_2Te_3 -based materials for thermoelectric power generation*. Journal of Materials Science, 2002. **37**(14): p. 2893-2897.
36. Li, D., et al., *Thermal conductivity of individual silicon nanowires*. Applied Physics Letters, 2003. **83**(14): p. 2934-2936.
37. Lindsay, L., D.A. Broido, and N. Mingo, *Diameter dependence of carbon nanotube thermal conductivity and extension to the graphene limit*. Physical Review B, 2010. **82**(16): p. 161402.
38. Lindsay, L., D.A. Broido, and T.L. Reinecke, *First-Principles Determination of Ultrahigh Thermal Conductivity of Boron Arsenide: A Competitor for Diamond?* Physical Review Letters, 2013. **111**(2): p. 025901.
39. Liu, D., et al., *Profiling Nanowire Thermal Resistance with a Spatial Resolution of Nanometers*. Nano Letters, 2014. **14**(2): p. 806-812.
40. Lv, B., et al., *Experimental study of the proposed super-thermal-conductor: BAs*. Applied Physics Letters, 2015. **106**(7): p. 074105.
41. Mahan, G.D. and J.O. Sofo, *The best thermoelectric*. Proceedings of the National Academy of Sciences, 1996. **93**(15): p. 7436-7439.
42. Mavrokefalos, A., et al., *Four-probe measurements of the in-plane thermoelectric properties of nanofilms*. Review of Scientific Instruments, 2007. **78**(3): p. 034901.
43. Mingo, N. and D.A. Broido, *Length Dependence of Carbon Nanotube Thermal Conductivity and the "Problem of Long Waves"*. Nano Letters, 2005. **5**(7): p. 1221-1225.

44. Morelli, D.T., J.P. Heremans, and G.A. Slack, *Estimation of the isotope effect on the lattice thermal conductivity of group IV and group III-V semiconductors*. Physical Review B, 2002. **66**(19): p. 195304.
45. Oehrlein, G.S., *Dry etching damage of silicon: A review*. Materials Science and Engineering: B, 1989. **4**(1-4): p. 441-450.
46. Oh, D.-W., et al., *Interfacial Thermal Conductance of Transfer-Printed Metal Films*. Advanced Materials, 2011. **23**(43): p. 5028-5033.
47. Perri, J.A., S. La Placa, and B. Post, *New group III-group V compounds: BP and BAs*. Acta Crystallographica, 1958. **11**(4): p. 310.
48. Persson, A.I., et al., *Thermal Conductance of InAs Nanowire Composites*. Nano Letters, 2009. **9**(12): p. 4484-4488.
49. Pettes, M.T., et al., *Influence of Polymeric Residue on the Thermal Conductivity of Suspended Bilayer Graphene*. Nano Letters, 2011. **11**(3): p. 1195-1200.
50. Pettes, M.T., et al., *Effects of Surface Band Bending and Scattering on Thermoelectric Transport in Suspended Bismuth Telluride Nanoplates*. Nano Letters, 2013. **13**(11): p. 5316-5322.
51. Pettes, M.T. and L. Shi, *Thermal and Structural Characterizations of Individual Single-, Double-, and Multi-Walled Carbon Nanotubes*. Advanced Functional Materials, 2009. **19**(24): p. 3918-3925.
52. Pinwen, Z., et al., *Enhanced thermoelectric properties of PbTe alloyed with Sb₂Te₃*. Journal of Physics: Condensed Matter, 2005. **17**(46): p. 7319.
53. Pop, E., et al., *Thermal Conductance of an Individual Single-Wall Carbon Nanotube above Room Temperature*. Nano Letters, 2006. **6**(1): p. 96-100.
54. Poudel, B., et al., *High-Thermoelectric Performance of Nanostructured Bismuth Antimony Telluride Bulk Alloys*. Science, 2008. **320**(5876): p. 634-638.
55. Poudeu, P.F.P., et al., *Nanostructures versus Solid Solutions: Low Lattice Thermal Conductivity and Enhanced Thermoelectric Figure of Merit in Pb_{9.6}Sb_{0.2}Te_{10-x}Sex Bulk Materials*. Journal of the American Chemical Society, 2006. **128**(44): p. 14347-14355.
56. Rowe, D.M., *CRC Handbook of Thermoelectrics*. 1995: Taylor & Francis.
57. Sadeghi, M.M., I. Jo, and L. Shi, *Phonon-interface scattering in multilayer graphene on an amorphous support*. Proceedings of the National Academy of Sciences, 2013. **110**(41): p. 16321-16326.
58. Schwab, K., et al., *Measurement of the quantum of thermal conductance*. Nature, 2000. **404**(6781): p. 974-977.
59. Seol, J.H., et al., *Two-Dimensional Phonon Transport in Supported Graphene*. Science, 2010. **328**(5975): p. 213-216.

60. Seol, J.H., et al., *Measurement and analysis of thermopower and electrical conductivity of an indium antimonide nanowire from a vapor-liquid-solid method*. Journal of Applied Physics, 2007. **101**(2): p. 023706.
61. Seol, J.H., et al., *Thermal Conductivity Measurement of Graphene Exfoliated on Silicon Dioxide*. Journal of Heat Transfer, 2010. **133**(2): p. 022403-022403.
62. Shen, S., et al., *Polyethylene nanofibres with very high thermal conductivities*. Nat Nano, 2010. **5**(4): p. 251-255.
63. Shi, L., *Comment on "Length-dependant thermal conductivity of an individual single-wall carbon nanotube" [Appl. Phys. Lett.91, 123119 (2007)]*. Applied Physics Letters, 2008. **92**(20): p. 206103.
64. Shi, L., *Thermal and Thermoelectric Transport in Nanostructures and Low-Dimensional Systems*. Nanoscale and Microscale Thermophysical Engineering, 2012. **16**(2): p. 79-116.
65. Shi, L., et al., *Measuring Thermal and Thermoelectric Properties of One-Dimensional Nanostructures Using a Microfabricated Device*. Journal of Heat Transfer, 2003. **125**(5): p. 881-888.
66. Slack, G.A., *Nonmetallic crystals with high thermal conductivity*. Journal of Physics and Chemistry of Solids, 1973. **34**(2): p. 321-335.
67. Snyder, G.J. and E.S. Toberer, *Complex thermoelectric materials*. Nat Mater, 2008. **7**(2): p. 105-114.
68. Swartz, E.T. and R.O. Pohl, *Thermal boundary resistance*. Reviews of Modern Physics, 1989. **61**(3): p. 605-668.
69. Tritt, T.M. and M.A. Subramanian, *Thermoelectric Materials, Phenomena, and Applications: A Bird's Eye View*. MRS Bulletin, 2006. **31**(03): p. 188-198.
70. Venkatasubramanian, R., et al., *Thin-film thermoelectric devices with high room-temperature figures of merit*. Nature, 2001. **413**(6856): p. 597-602.
71. Wang, S., et al., *Synthesis and Characterization of a p-Type Boron Arsenide Photoelectrode*. Journal of the American Chemical Society, 2012. **134**(27): p. 11056-11059.
72. Wang, Z. and N. Mingo, *Diameter dependence of SiGe nanowire thermal conductivity*. Applied Physics Letters, 2010. **97**(10): p. 101903.
73. Wang, Z., et al., *Thermal Transport in Suspended and Supported Few-Layer Graphene*. Nano Letters, 2011. **11**(1): p. 113-118.
74. Weathers, A., et al., *Reexamination of thermal transport measurements of a low-thermal conductance nanowire with a suspended micro-device*. Review of Scientific Instruments, 2013. **84**(8): p. 084903.

75. Weathers, A. and L. Shi, *Thermal Transport Measurement Techniques for Nanowires and Nanotubes*. Annual Review of Heat Transfer, 2013. **16**: p. 101-134.
76. Wei, L., et al., *Thermal conductivity of isotopically modified single crystal diamond*. Physical Review Letters, 1993. **70**(24): p. 3764-3767.
77. Wingert, M.C., et al., *Ultra-sensitive thermal conductance measurement of one-dimensional nanostructures enhanced by differential bridge*. Review of Scientific Instruments, 2012. **83**(2): p. 024901.
78. Yu, C., et al., *Thermal Conductance and Thermopower of an Individual Single-Wall Carbon Nanotube*. Nano Letters, 2005. **5**(9): p. 1842-1846.
79. Zhou, F., et al., *Determination of Transport Properties in Chromium Disilicide Nanowires via Combined Thermoelectric and Structural Characterizations*. Nano Letters, 2007. **7**(6): p. 1649-1654.
80. Zhou, J., et al., *Thermoelectric properties of individual electrodeposited bismuth telluride nanowires*. Applied Physics Letters, 2005. **87**(13): p. 133109.
81. Ziman, J.M., *Electrons and Phonons: The Theory of Transport Phenomena in Solids*. 1960: OUP Oxford.

Vita

Jae Hyun Kim attended Seoul National University in Seoul, South Korea majoring in Mechanical and Aerospace Engineering, and received a Bachelor of Science in February 2003 and a Master of Science in February 2005, respectively. During the undergraduate, he joined the Republic of Korea Army in 1999 and was discharged in 2001 as a sergeant. He worked for Samsung Electronics from 2005-2007 as a photolithography process engineer. He joined the research group of Prof. Li Shi in August 2008 as a doctoral student of Mechanical Engineering, the University of Texas at Austin.

Permanent address (or email): jh77.kim@gmail.com

This dissertation was typed by the author.